THERMALLY DRIVEN HYDROMAGNETIC DYNAMOS

by

GRAEME A. MORRISON

A thesis submitted to the Faculty of
Science, University of Glasgow, for the
degree of Doctor of Philosophy.

Department of Mathematics,

University of Glasgow,

October 1999

i

ProQuest Number: 13834252

ProQuest 13834252

Summary

There are still many challenges to be overcome before we can claim to have a full understanding of the generation of the Earth's magnetic field. From a mathematical point of view, the governing equations are nonlinear and must be solved in fully three dimensions, meaning that a numerical method must be employed, although this would probably also be the case for a two-dimensional problem. However, it is only relatively recently that the computer technology has become available to make this possible. Obtaining these solutions remains a highly computationally intensive task, making it difficult to find solutions for a range of parameter values. This is extremely important as a great deal of uncertainty still surrounds the present (and past) geophysical values of the main parameters in the governing equations. Our aim is to try and further understanding of the effect of varying some of these key parameters in simplified, but fully self-consistent hydromagnetic dynamo models. These models will allow us to examine the effect of including the full inertial term to the equations, which has in the past been neglected due to the small geophysical value of the parameter which controls its effect. Further physical insight into the magnetic field generation mechanism will be provided, and we will examine some key issues in numerical dynamo modelling.

A broad introduction to the Earth's magnetic field, the properties of the core, the possible energy sources and the current state of successful numerical dynamo models, is given in Chapter 1. In Chapter 2 we will describe in detail the governing equations and associated theory of magnetohydrodynamic (MHD) flows in a rapidly rotating spherical shell, as is appropriate for the Earth. Chapter 3 presents the results of varying the

Rayleigh number, Ra, and the azimuthal wavenumber, m, for a $2\frac{1}{2}D$ dynamo model, and also examines the effect (if any) of different forms of thermal driving. We show that the dynamo can exhibit very different types of behaviour for small changes in Ra, and in one particular case the magnetic field can be shut off, leaving only a convective solution. This type of behaviour is not observed for a different value of m. Our model is therefore too severely truncated in azimuth, but also suggests that care should be exercised when interpreting the results from a single run of a numerical dynamo model with a fixed value of Ra. The different forms of thermal driving produce qualitatively very similar dynamos, with the case of internal heating seeming to give the most efficient dynamo at any given value of Ra. However our definition of Ra is most suitable for internal heating, and this probably accounts for the difference in efficiency.

In Chapter 4, the same $2\frac{1}{2}D$ model is used to examine the effect of varying the inner core radius. This is the first detailed study to be performed in a fully self-consistent dynamo model, and will aid understanding of the long term behaviour of the geodynamo, because the inner core is slowly growing as it freezes out of the outer core fluid. We find that the critical Rayleigh number for the onset of convection is dependent on the inner core radius. This plays a crucial role in determining the behaviour of the solution, along with the geometry and the diffusion time of the inner core. We show that not only does a large inner core stabilise the magnetic field, due to the diffusion time of the inner core, but that a small inner core also stabilises the magnetic field, due to the simpler geometry.

The inertial term has not been included in a $2\frac{1}{2}D$ model before, although it is included in some form in most $3D$ models. In Chapter 5, we use a different $2\frac{1}{2}D$ model to examine the effect of including the inertial term, and choosing different values of the Rossby number, Ro, while keeping the Ekman number, E, fixed. In addition the imposed equatorial symmetry constraint has been removed in this new model. We find a rather complicated pattern of behaviour, with the inertia of the fluid strongly

iii

affecting the time dependence of the solution obtained, but having less effect on the structure on the flow. There are two possible solutions, one which is chaotic and one which is periodic. As the value of Ro is increased we find that it becomes increasingly difficult to maintain a magnetic field, and above a certain value of Ro no solutions could be obtained. A solution obtained with $m = 4$ intermittently changes between chaotic and periodic states.

For my parents and family, who have supported all my academic endeavours, and my wife, Lee, whose patience and help have enabled me to finish on time.

Contents

List of Figures

xi

List of Tables

Preface

This thesis is submitted to the University of Glasgow in accordance with the requirements for the degree of Doctor of Philosophy.

Many people have aided me in the production of this thesis. I would like to take this opportunity to thank my supervisor, Prof. David Fearn, for his advice, encouragement and support, throughout the period of my research. This work has leaned heavily on the codes developed by Dr. Rainer Hollerbach, who also provided excellent advice on the development of the new $2\frac{1}{2}D$ code. I am indebted to Dr. Graeme Sarson for helping me get started with the original $2\frac{1}{2}D$ code and for providing me with details of his results. Lastly, I would like to thank my fellow research student Paul Fotheringham for many helpful discussions on the finer points of computing, and in particular the AVS graphics package.

Chapter 1

Introduction

1.1 The geomagnetic field

The Earth has possessed an internally generated magnetic field, the geomagnetic field, for at least the past 3.5×10^9 years (McElhinny and Senanayake 1980). The geomagnetic field was known about by at least the first century AD, when the magnetic compass was invented by the Chinese, although the origin of the magnetic field remained unknown. Over the subsequent centuries a better understanding of the magnetic field and the mechanism by which it is generated has been developed, but our knowledge is still far from complete. The first major jump in understanding came in 1600 when William Gilbert realised that the origin of the geomagnetic field lay inside the Earth. Many subsequent observations of the geomagnetic field at the Earth's surface were made, with the first geomagnetic chart produced by Halley at the end of the 17th century. Rocks, exposed at the surface of the Earth and on the ocean floor, and sediments, containing even small traces of iron, provide a record of how the geomagnetic field has changed over time. This has been recognised for about 150 years, but it is only in the latter half of the 20th century, that paleomagnetic studies have extracted enough knowledge of the polarity and local direction of the magnetic field to allow the construction of a polarity time scale, covering the past few hundred million years. These studies were also to prove invaluable in confirming the theory of continental drift and plate tectonics. Records

of the intensity of the paleomagnetic field are more difficult to obtain. It is crucial that the rock samples are unaltered from formation or not chemically altered in the laboratory. Even when a suitable sample exists, two different intensity measurements from the same sample may not give consistent results. To contribute to the construction of a continuous record of polarity or intensity, the sample must also be reliably dated. The best continuous record currently available, covers about the past 8×10^5 years (Guyodo and Valet 1999). There are also studies covering a longer range of time, but these are not continuous records (Juarez et al. 1998). Analysis of the paleomagnetic record, reveals that the geomagnetic field is continuously changing, and has experienced excursions and reversals of polarity many hundreds of times. The average time between reversals is about $2 - 3 \times 10^6$ years, but the reversal frequency is rather irregular. This frequency may be controlled by conditions at the core mantle boundary, with the inner core also playing a significant role. Indeed it was once believed that the geomagnetic field was relatively stable between reversals, but recent analyses of paleomagnetic data, up to the time of the last reversal, suggest that the geomagnetic field may be in an excursional state up to 20% of the time between reversals. It is very difficult to define precisely what an excursion is in a complex time varying magnetic field, but usually at a given site, there will be a large departure from the usual geomagnetic field direction. The geomagnetic field may be observed to change polarity, but if it does so then it returns to its original state. A reversal exhibits similar behaviour, but the magnetic field remains stable in the new polarity. Both these features seem to be associated with a large drop in geomagnetic field intensity, but this is not considered to be a defining feature. We also know from current observations, and historical and paleomagnetic records that the direction of the geomagnetic field at any fixed point on the Earth varies with time. This so-called secular variation of the geomagnetic field occurs on time scales of years to thousands of years. One of the greatest challenges facing paleomagnetists, is to establish whether excursions, reversals and secular variation of the geomagnetic

field are really distinct phenomena. If an excursion is observed contemporaneously at more than one site, then it is a global feature, if not, then all that may be recorded is large secular variation at that site. Gubbins (1999) uses the recent data to suggest that excursions are part of the (paleo)secular variation. He suggests that during an excursion, the magnetic field reverses in the outer core, but not in the inner core, resulting in the original parity being restored. The duration of an excursion (about 5-10 $\times 10^3$ years) is consistent with the diffusion time associated with the inner core. A full reversal only occurs if the reversed outer core field persists for this diffusion time. It is fair to say that his is not a consensus view, and much more data and longer records are required.

The current geomagnetic field, can be approximated by that due to an axial dipole fixed at the centre of the Earth, with the dipole axis inclined at about 11° to the rotation axis. The dominating influence of the Coriolis force on the convective motions in the Earth's core, would be expected to on average produce an axially symmetric magnetic field. Due to secular variation the time-averaged paleomagnetic field differs substantially from this instantaneous field, but has been, to a first order approximation, a geocentric axial dipole over the past few million years. This assumption is fundamental to the measurement and interpretation of paleomagnetic data. By contrast the intensity of the geomagnetic field, outwith excursions and reversals, has remained relatively constant over almost the full length of its existence. There is also a significant component which can be considered as non-dipole, making up about 20% of the observed surface magnetic field, although it is much more localised than the dipole component. This is also found to vary with time, with one of the best known features the westward drift which has averaged about 0.18^o/year over the past 150 years, although it is unclear whether this is a permanent feature.

Measurements of the geomagnetic field have been made for at least 500 years now in land-based observatories and in the logs of ships, which used the geomagnetic field

3

as a navigational aid. More recently magnetic surveys of the ocean floor have been performed from ships and the whole Earth has been surveyed from space. We now have a reasonable, but by no means complete, picture of the intensity and structure of the geomagnetic field, and its variation with time. However we are less certain about the underlying generation process. This must take place in the deep interior of the Earth, and must be able to explain the observed features of the geomagnetic field described above. The only realistic region of the Earth for magnetic field generation to take place is the core. Since we know that hundreds of reversals have taken place, it seems highly unlikely that the presence of a magnetic field is due to some form of permanent magnetisation. All electrically conducting materials, lose their magnetic properties above some critical temperature called the Curie temperature. For iron at low pressure, this temperature is about $1000K$. The high temperatures present in the Earth's core (see Table 1.1) then also make permanent magnetisation an unlikely scenario, but cannot rule it out since it is not clear how the Curie temperature will change with increasing pressure. Unless they contain sources of electric current, conducting bodies of spatial dimension, L, can only retain their magnetic fields for times of the order of the electromagnetic diffusion time,

$$\tau_\eta = L^2/\eta, \tag{1.1}$$

where η is the magnetic diffusivity of the constituent material. Using values of these quantities appropriate for the core (see Table 1.1), and substituting into (1.1), we obtain a value of τ_η of $O(10^5)$ years. Clearly some process must be maintaining the geomagnetic field against diffusion.

Larmor (1919a,b) first proposed that the magnetic fields of astronomical bodies were produced by motions in internal conducting regions, which induce from the magnetic field an emf that creates currents which generate the inducing magnetic field itself. This is known as self-excited dynamo action, and is currently the only plausible generation

4

mechanism for the geomagnetic field. In the context of the Earth, the dynamo process is often referred to as the geodynamo and would be expected to generate the bulk of the geomagnetic field. However, there may be other processes, which contribute, although this contribution is most likely very small (see Merrill et al. 1996 for a brief review). Exploration of the solar system by unmanned spacecraft, as well as Earthbound observations have also revealed that many other planetary bodies in the solar system possess, or have in the past possessed, intrinsic magnetic fields. These magnetic fields are probably produced by similar internal processes (Stevenson et al. 1983). The latest such exploration has revealed that two of the Galilean satellites of Jupiter, Io and Ganymede, have intrinsic magnetic fields (Schubert et al. 1996). The dynamo process may be fundamentally different in these particular planetary bodies as both sit inside the strong Jovian magnetic field.

1.2 Composition and properties of the core

Our knowledge of the structure of the Earth is obtained from seismic observations. From these observations, we know that the Earth consists of three separate regions. At the centre is the core, which takes up about half the radius of the Earth. Above this is the mantle, with a very thin layer on top, known as the crust. The principal region of interest is the Earths's core, which itself has two distinct regions, the fluid outer core, where dynamo action takes place, and the solid inner core. The overall composition of the core can be obtained from geochemical and mineral physics studies. These use testing in the laboratory by diamond anvil cell, ultrasonic, X-ray diffraction and shock wave experiments to simulate core conditions, and so to establish which elements or compounds can be present in the core (Mao and Hemley 1998). There is general agreement that the main constituent of the core is Iron, while studies of the composition of meteorites suggest that about 4% Nickel should also be present. However, the density of the core is about 10% below that of pure Iron, and so there

must be some other lighter elements present. It is uncertain as to how these elements are partitioned between the inner and outer cores, but the density contrast across the ICB ($0.5 kg/m^3$), inferred from seismic results (Shearer and Masters 1990), implies that the inner core contains more Iron than the outer core. The exact identity of these lighter elements is uncertain at present with Sulphur, Oxygen, Silicon, Carbon, Magnesium and Hydrogen all being possible candidates (Poirier 1994). If some of the common radiogenic heat producing elements present in the Earth are also present in the core, then an even greater concentration of light elements is required. The most likely radiogenic element partitioned into the core is Potassium, as it is believed that the upper regions of the Earth are depleted in this element.

The inner core was discovered by Lehmann (1936) from seismic observations, which indicated that it was a solid body. It was only last year that the first direct evidence for a solid inner core was obtained, when a shear wave was detected passing through the inner core (Okal and Cansi 1998). This suggests that the inner core boundary (ICB) is a phase boundary, and Jacobs (1953) was the first to suggest that the ICB is a freezing interface, with iron crystallising from the outer core fluid as the Earth cools, providing two different energy sources, latent heat due to freezing and compositional buoyancy due to the excess of light elements (see 1.3.2). The freezing process has been well studied in the metallurgical literature (e.g. Chalmers 1964, Copley et al. 1970), and more recently from aqueous experiments (Huppert 1990, Tait and Jaupart 1992, Worster 1997). It seems certain that the freezing interface is not sharp, freezing taking place in a mushy zone, which is a mixture of fluid and solid, with the mass fraction of solid increasing with depth. The fluid fills the gaps between the solid which is probably in the form of dendrites. However due to the sharp density contrast inferred from seismic results, the effective depth of this layer can only be of the order of a kilometre (Loper 1983).

There are three phases of Iron which are definitively known, but it is still uncer-

6

tain as to which is stable at inner core temperatures and pressures. Which phase is present in the inner core may have an effect on the bulk properties, the amount of latent heat released, the ability of the inner core to incorporate light elements and also the magnitude and symmetry of the anisotropy. From first principles calculations and observations, some form of hexagonal close packed (hcp) structure seems to fit best (Stixrude and Brown 1998). Seismological observations of free oscillations and PKIKP travel times have shown that the inner core is acoustically anisotropic, with longitudinal waves propagating parallel to the rotation axis travelling faster than those propagating parallel to the equatorial plane (Morelli et al 1986, Woodhouse et al. 1986). Individual iron crystals have an intrinsic acoustic anisotropy, which if suitably aligned, may explain the seismic observations. Magnetic or dynamic effects may be responsible for this crystal alignment, but the exact source of the anisotropy remains unclear. The anisotropy is not uniform in the core. Recent observations suggest that the axis of anisotropy is not aligned with the rotation axis, but is inclined at an angle of about 10° (Su and Dziewonski 1995). The upper 200km of the inner core are also believed to be isotropic (Song and Helmberger 1998). Examination of the travel time records for seismic waves following a specific path through the Earth, suggest that the fast axis has shifted eastwards over time. This can be explained by the inner core rotating faster than the mantle (Song and Richards 1996, Su et al. 1996, Creager 1997). The motivation for these seismic studies was a prediction from numerical dynamo models that the inner core should super-rotate due to the strong electromagnetic torque acting upon it. The magnitude of the rotation rate obtained in the numerical models is consistent with the rotation rate inferred from observation. This varies between the different studies, but a value of about 1° per year seem reasonable. The existence of inner core rotation remains a subject of vigorous debate. Some doubt surrounds whether the tilt of the anisotropy axis has been reliably detected (Souriau et al. 1997, Souriau 1998a), and whether the seismic data has been accurately timed (Rohm et. al. 1999). The

7

observation of inner core rotation clearly depends crucially on these two factors. In addition a study based on a different seismic ray path seems to place an upper limit on the magnitude of the rotation rate (Souriau 1998b), which is nonetheless compatible with other results.

Table 1.1: Typical estimates of the values obtained by some important parameters and quantities in the Earth's core.

Property	Symbol	Value
Rotation rate	Ω	$7.27 \times 10^{-5}\ s^{-1}$
Density (ICB)	ρ_i	$1.28 \times 10^4\ kgm^{-3}$
Density (CMB)	ρ_o	$9.90 \times 10^4\ kgm^{-3}$
Inner core radius	r_i	$1215\ km$
Outer core radius	r_o	$3485\ km$
Kinematic viscosity	ν	$1 \times 10^{-6}\ m^2s^{-1}$
Electrical conductivity	σ	$5 \times 10^5\ Sm^{-1}$
Magnetic diffusivity	η	$1\ m^2s^{-1}$
Magnetic permeability	$\mu \approx \mu_0$	$4\pi \times 10^{-7} Hm-1$
Thermal expansion	α	$5 \times 10^{-6}\ K^{-1}$
Thermal diffusivity	κ	$1 \times 10^{-5}\ m^2s^{-1}$
Magnetic field (CMB)	B	$2 \times 10^{-3}\ T$
Temperature (CMB)	T	$4 \times 10^3\ K$
Pressure (ICB)	P	$3 \times 10^{11}\ Pa$

Some of the values for the physical properties associated with the Earth's core are given in Table 1.1, with locations given where appropriate. Any quantity without an associated location is assumed to be constant throughout the core. The viscosity of the outer core fluid is one of the most poorly known quantities in geophysics, with estimates ranging over 12 orders of magnitude! The most recent estimates place this value at about $O(10^{-6})\ m^2s^{-1}$ (de Wijs et al. 1998), a very low value. This has serious implications for attempting to model the dynamo process, as is discussed in Chapter 3.

The core-mantle boundary also plays an important role in the dynamics of the core and also perhaps reversals of the magnetic field. At this point the silicate materials of

the mantle come into contact with the Iron alloys of the core. Seismic evidence suggests that there is a distinct region of variable thickness and composition at the base of the mantle, called D'', which exhibits relatively slow shear wave velocities. This layer may also have a conducting region near the CMB (Knittle and Jeanloz 1989), which would increase electromagnetic coupling between the core and the mantle. Some of the variations of the magnetic field in the core would be partially screened, meaning that estimates of core flow velocities, and magnetic field strengths would have to be revised. Lateral variations in heat flux at the CMB, caused by mantle convection, occur on a time scale of about 2×10^7 years, and there is also some seismic evidence of small scale topography on the CMB. Both of these features can have a locking effect on the convection in the outer core (see for example Sarson et al. 1997a).

1.3   Energy sources

Any potential energy source for the geodynamo, must possess enough power to be able to generate a magnetic field of the observed magnitude, and be able to efficiently convert the kinetic energy of the fluid motions to magnetic energy. An estimate of the power required to drive the geodynamo can be obtained from the relation,

$$Po = \frac{d}{dt} \int_V \frac{\mathbf{B}^2}{2\mu_0} \, dV = -\int_V \frac{\mathbf{J}^2}{\sigma} \, dV, \tag{1.2}$$

where V is the volume of the core. This relation is itself obtained by first setting $\mathbf{U} = \mathbf{0}$ in the induction equation (2.2), then taking the scalar product with $\mathbf{B}/\mu_0$, and using the vector identity $\nabla \cdot (\mathbf{e} \times \mathbf{f}) = \mathbf{f} \cdot (\nabla \times \mathbf{e}) - \mathbf{e} \cdot (\nabla \times \mathbf{f})$, where $\mathbf{e}$ and $\mathbf{f}$ are arbitrary vectors. The first integral represents the rate of change of magnetic energy, while the second represents the ohmic power dissipation. With an insulating mantle, the current $\mathbf{J}$ vanishes for $r > r_o$, and since $\mu_0 \mathbf{J} = \nabla \times \mathbf{B}$ then,

$$Po \approx \frac{4}{3} \pi r_o^3 \frac{B^2}{\sigma \mu_0^2 L^2}, \tag{1.3}$$

9

where B is a typical field strength and L an appropriate length scale. Merrill et al. (1996) suggest that a lower bound for the power required is $O(10^{10})\ W$. The Ohmic energy loss is made good by conversion (through $\nabla \times (\mathbf{U} \times \mathbf{B})$ in (2.2)) from the kinetic energy of the flow, which must be continually replenished. There are three main energy sources available to drive the geodynamo, thermal convection, compositional convection and precessional or tidal forcing. These are all discussed more fully below, and it may be that all three contribute in varying degrees to the energy budget, certainly none can be discounted, but the bulk of the energy is expected to come from compositional convection. However, most numerical dynamo models have retained thermal convection as their driving mechanism because it has been much more widely studied, and is much less complicated to implement. Glatzmaier and Roberts have come closest to incorporating a compositional buoyancy source in their model. The inner core grows releasing latent heat and light constituents at the ICB, with the buoyancy proportional to the growth rate of the inner core. However it is still unclear if the values of the diffusivities are correct, and no allowance has been made for a mushy layer at the top of the inner core.

1.3.1 Thermal convection

The classic text of Chandrasekhar (1961) develops the foundations of the theory of linear thermal convection, which was extended to spherical geometry, with radial temperature gradient and gravity, by Roberts (1968) and Busse (1970). Since then thermal convection has been a subject of wide experimental and theoretical interest (Knobloch 1998). In the context of the core we have to consider the effects of rapid rotation, a magnetic field and spherical boundaries on the convective flow, and this is done in Chapter 2. Of course, if thermal convection is to provide the power source for the geodynamo, then there must be a source of heating in the core, and this heat source must produce a temperature gradient in excess of the adiabatic temperature gradient.

This represents the heat which can be conducted from the core without any convection taking place. The heat sources may be concentrated at the ICB or spread throughout the core. At the ICB, the main source of thermal buoyancy is the release of latent heat due to freezing of the inner core, which has an associated compositional buoyancy source (see 1.3.2). Heat is also released as the Earth cools naturally over time, and by any radioactive isotopes which may be present in the core. Even if there is significant radiogenic heat released in the outer core, much of it may be conducted away without any effect on the fluid. Heat released at the ICB on the other hand is more efficient at stirring the core, since the amount of heat that can be conducted down the adiabatic temperature gradient is proportional to surface area i.e. r^2.

1.3.2 Compositional convection

Compositional convection is associated with the freezing of the inner core. As noted earlier, the core is composed predominately of Iron with some lighter impurities. The temperature below which freezing takes place is a function of the amount of impurity as well as pressure. As the Earth cools, this temperature is reached first at the centre of the fluid, due to the effect of pressure. When the concentration of impurity is small, the solid that freezes is almost pure Iron, with most of the impurity left in the remaining fluid. This leaves an excess of buoyant light elements close to the ICB, giving rise to a source of compositional buoyancy (Loper and Roberts 1981). The light fluid released in the mushy zone rises to stir the flow in the outer core. Very little is known about the effects of magnetic fields and rotation on this process, both of which may be important for the core. Originally experimental work suggested that compositional convection was in the form of narrow chimneys emanating from a mushy zone at the ICB, but more recent work suggests that this may not be possible due to the effect of the magnetic field (Bergman and Fearn 1994, Bergman et al. 1997). Conductive losses are much smaller for compositional buoyancy, meaning that it may

be the most efficient method of driving the geodynamo. A recent estimate suggests that compositional convection satisfies about 80% of the energy requirement of the geodynamo, with the remainder coming from thermal convection (Lister and Buffett 1995). This ratio may have changed over time as the inner core has grown through freezing.

1.3.3 Precessional and tidal forcing

The Earth is to a good approximation an oblate spheroid and since the equatorial bulge is inclined (at 23.5°) to the orbital plane, the gravitational attraction of the Sun and Moon produce a resultant torque on the Earth. This strong gravitational attraction also produces a tidal bulge at the equator. Both of these can produce motion in the core, but it is unclear how this energy is converted into a flow which can generate the geomagnetic field. This energy source for the geodynamo has been strongly supported by Malkus, who comprehensively reviews the subject in Malkus (1994). Progress is being made in both numerical and experimental studies, but a precessionally driven dynamo model is still some way off (Kerswell 1996). To complement the experimental and numerical work, paleomagnetists have looked for evidence of the well known cycles of the Earth's orbital parameters (Milankovitch 1941) in paleointensity measurements, with varying degrees of success (Channell et al. 1998, Guyodo and Valet 1999).

1.4 Numerical dynamo models

Since the prospects for directly sampling core material or viewing the fluid motions in the outer core are very bleak, indirect methods have to be used to further understanding of the geodynamo process. We have already seen that the behaviour of the geomagnetic field can be obtained from observatory measurements, navigational logs, historical sites, and ancient rocks, and that knowledge of the properties of the Earth's interior, and in particular the composition and structure of the core is shaped

by seismology and high pressure mineral physics. Experimental dynamo models are an (expensive) possibility, however they can never reproduce the correct (planetary) scale of the problem, for quite obvious reasons. Numerical dynamo modelling still remains the most likely method of producing a model which is at least representative of the geodynamo. Any numerical model should retain as many physical features of the Earth's core as possible, producing a surface magnetic field which is at least of similar magnitude to the Earth's, with a dominant dipole component. This magnetic field should also exhibit the time-varying features of the geomagnetic field, e.g. secular variation, reversals, excursions, and possibly westward drift. The appropriate geometry is a spherical shell, with an inner core which is solid, and an outer core which is fluid. The equations, and associated boundary conditions, governing the geodynamo are well known (see Chapter 2), however, as we shall see, the parameter values relevant to the Earth's core are less well known. There are also some constraints on the self-excited dynamo process itself, which make numerical geodynamo modelling more difficult. One of the most important is due to Cowling (1934), who showed that a magnetic field, which is symmetric about an axis (as the Earth's approximately is), cannot be maintained by any fluid motion. In other words the geodynamo process is necessarily three-dimensional in character. Given the three-dimensional nature of the problem, the nonlinear governing equations must be solved numerically. It is only recently that the computational power has become available to solve the full $3D$ problem, and previously one had to study magnetoconvection or introduce some simplifying assumptions to the equations (see Chapter 2).

Using different approaches, Glatzmaier and Roberts (Glatzmaier and Roberts 1995a,b, 1996a,b,c) and Kuang and Bloxham (Kuang and Bloxham 1997, 1999) have both produced $3D$, fully self-consistent, hydromagnetic numerical dynamo models, exhibiting many of the qualitative features of the observed geomagnetic field. Both these models use hyperdiffusivities to try and better model the parameter regime of the Earth's core,

a point which is discussed more fully in Chapter 2. The Glatzmaier-Roberts dynamo was the first to be produced, with thermal convection as an energy source. The radial magnetic field produced had a similar pattern, amplitude and secular variation at the CMB as the Earth's. This model predicted that the inner core would super-rotate, and also produced a reversal of the magnetic field, which was similar to real reversals of the geomagnetic field (Glatzmaier and Roberts 1995a,b). After this initial success, the model has been improved by using an anelastic approximation for the compressibility of the fluid; by including the azimuthal part of the axisymmetric inertial term, and by incorporating a simulated compositional buoyancy source with a growing inner core. A concise summary of the current state of the model is given in (Glatzmaier and Roberts 1998). Recently, the model has been used to examine the effect of lateral heterogeneity in the heat flux at the CMB on reversals of the magnetic field (Glatzmaier et al. 1999). The Kuang-Bloxham model has also produced an external magnetic field, which is dominated by an axial dipole component, and has an intensity close to the present-day geomagnetic dipole moment. The non-dipole magnetic field also displays westward drift, like the historical geomagnetic field. In the interior of the core however, the generated magnetic fields look very different. Kuang and Bloxham attribute these differences to their choice of boundary conditions for the flow, while Glatzmaier and Roberts attribute the differences to their treatment of inertial effects. This is a fundamental point which will be discussed more fully in Chapter 5. Recent work with the Kuang-Bloxham model has concentrated on two main areas, the force balance in the momentum equation, and comparison with historical and paleomagnetic field observations. Clearly close collaboration between paleomagnetists and the dynamo modelling community, will be mutually beneficial. There are also now fully $3D$, well resolved numerical dynamo models, which do not require the use of hyperdiffusivity or artificial parameterisations, but are run at less realistic parameter values (Kageyama and Sato 1997, Busse et al. 1998, Christensen et al. 1998 and Sakuraba and Kono 1999).

14

While the results of the 3D models have been encouraging, all of the models still make some unrealistic assumptions, due in part to computational limitations and in part to gaps in our knowledge. Even with today's supercomputers it is still very difficult to perform detailed surveys of even the attainable parameters. The previously mentioned constraints on 3D models, suggest that a slightly simpler approach is required, while still self-consistently solving for the flow and magnetic field. This can be achieved by using the so-called $2\frac{1}{2}D$ approximation, in which the full solution structure in the radial and latitudinal directions is included, but the azimuthal structure is constrained to be of fixed periodicity. It should be noted that the 3D models also have less structure in the azimuthal direction, and the difference between the two is merely one of degree. The benefit of adopting this approximation is that the computational limitations are greatly reduced. A successful model using such an approach was produced by Jones et al. (1995), and since the initial results have been produced, this model has proved invaluable in probing both the geodynamo and possible magnetic field generation processes for the Jovian moons. Preliminary work looked at the effect of topography on the core-mantle boundary and a stably stratified layer at the top of the outer core (Sarson et al. 1997a). The next modification to the model was to introduce an ambient magnetic field, which simulates the main Jovian magnetic field in which Io and Ganymede reside, to gain further understanding of the effect that this has on the dynamo process (Sarson et al. 1997b, 1999). More recently the $2\frac{1}{2}D$ model has been studied in two very different parameter regimes, Busse-Zhang (BZ) type dynamos and Glatzmaier-Roberts (GR) type dynamos (Sarson et al. 1998b). The GR type dynamos adopt more realistic parameter values, requiring the use of hyperdiffusivities, but seem to better model the geodynamo. Subsequently, the GR type dynamos have been used to study a model reversal of the magnetic field (Sarson and Jones 1999), and to incorporate more azimuthal modes, with so far $m = 2, 4, 6, 8$ all being included (Sarson et al. 1998a). This is clearly an intermediate model between the $2\frac{1}{2}D$ and fully

$3D$ models.

As we shall see, in any hydromagnetic dynamo model, several non-dimensional parameter values have to be prescribed. If the model includes an inner core, as this one does, then a value also has to be assigned to the ratio of the inner core radius to outer core radius, χ. Since none of the parameter values for the Earth are well known, and the value of χ has changed over time, it is clear that the influence of different prescribed parameters on dynamo solutions needs to be established. This is generally impractical with $3D$ models, given the computational effort required to produce one solution at a given set of parameters, though a limited parameter survey using a $3D$ model has been reported by Christensen et al. (1999). The $2\frac{1}{2}D$ model is, on the other hand, not only capable of qualitatively reproducing the main features observed in the Boussinesq Glatzmaier and Roberts $3D$ model (Sarson et al. 1998b), but is also free from the associated computational restrictions, allowing solutions to be obtained for a much larger parameter range, longer run times, or higher truncations. It is also sensible to consider the effects of different energy sources and different boundary conditions for the temperature, flow and the magnetic field. Clearly, incorporating more than one energy source into a single model is a non-trivial task. With thermal convection as the energy source it is possible to consider the effect of different distributions of heat sources, and we will do so in Chapter 3. Although the boundary conditions for each of the quantities can be altered, we choose to keep these fixed.

The equations governing the geodynamo process and the details of the models which are used to investigate the effects of the different parameters will be briefly discussed in Chapter 2. The full mathematical and computational details can be found in the Appendices. We will also present the theory of magnetohydrodynamic (MHD) flows in rapidly rotating systems, and the force balance in the outer core fluid. The first model we will use is that used by Jones and co-workers. It adopts dipolar symmetry (as defined in Chapter 2) and uses thermal convection as an energy source. The second

model has been obtained by removing all but one azimuthal mode from the $3D$ model of Hollerbach (1999), and incorporating a finitely conducting inner core. This model has no imposed symmetry constraint, includes the full inertial term and again uses thermal convection as an energy source. Chapter 3 examines the influence of varying the temperature gradient, through the Rayleigh number, Ra, for two different values of the azimuthal wavenumber, m. Since the value of Ra is not well known for the Earth, it is important to examine what effect prescribing a slightly different value can have. Additionally, some comment will be made on the effect of a different source of heating. With our system as defined, we find that care must be taken in the interpretation of the value of Ra. In Chapter 4 we examine the changes in dynamo behaviour when the inner core radius is varied. The discussion will be facilitated by presenting the results using different definitions for the non-dimensional parameters, E, Ra and τ. The usual parameter values can be restored by using a simple scaling factor. We will focus on one of the solutions at small inner core radius, which allows us to perform a sensible survey of other parameter values. The final piece of work, presented in Chapter 5, centres on the inertial term in the momentum equation. We will study the effect that restoring this term has on a dynamo solution obtained with no inertia, and which value of Ro is more appropriate for our given, fixed value of E.

Chapter 2

Theoretical framework

2.1 Physical model

We assume that the Earth's core is spherical with two distinct regions, the solid inner core and the fluid outer core. The inner and outer boundaries are assumed to be perfectly spherical, and so any precessional and topographical effects on the solutions are ignored. Both of these regions are assumed to be composed solely of electrically conducting material, with physical properties which, where possible, reflect the predominance of Iron in the core (see Table 1.1). Effectively our model core can be thought of as consisting of Iron, with some radiogenic elements present in the outer core fluid to provide a source of internal heating. We adopt the Boussinesq approximation where all the parameters arising in the equations are assumed constant throughout the core, with the exception of the density of the outer core fluid in the buoyancy term. In other words we are dealing with strictly incompressible fluids, but allow density variation in the buoyancy term to enable us to drive convection. By adopting this approximation all values of magnetic field, flow and temperature must be interpreted as being relative to the adiabatic values. In reality the fluid is compressible and the parameter values will change as the density changes, but this simplifying assumption has been adopted in most models to date.

The inner core is assumed to have the same conductivity as the outer core, while

the mantle is taken to be electrically insulating. As we shall see in (2.2.2), this means that we have to solve for the magnetic field in the inner core and then match the three components of this magnetic field and its radial derivative to those of the outer core magnetic field at the inner core boundary. Otherwise, if the inner core was either electrically insulating or perfectly conducting then changes to the magnetic field in the inner core could be obtained from the boundary conditions. At the CMB, the outer core magnetic field is matched to a potential field.

Our energy source is restricted to purely thermal convection, but we are free to choose the source of the heating. The outer core can be assumed to be uniformly internally heated, or we can assume differential heating of the ICB and CMB, or a combination of the two. Whichever source is chosen, there is a spherically symmetric distribution of temperature in the absence of convection. Most of our studies have been performed using internal heating to facilitate comparison with previous work, but we do also consider different temperature profiles. The rotation of the Earth is simulated by uniform angular velocity about the z-axis, where z is the axial cylindrical polar coordinate. In line with the discussion in Chapter 1, the inner core is also free to rotate about this same axis.

2.2 Equations

The equations governing hydromagnetic convection in a physical system as described above are shown below:

$$\rho_0 \left(\partial \mathbf{U}/\partial t + (\mathbf{U} \cdot \nabla)\mathbf{U} + 2\mathbf{\Omega} \times \mathbf{U} + \mathbf{\Omega} \times (\mathbf{\Omega} \times \mathbf{r}) \right) = \qquad (2.1)$$

$$-\nabla P + \rho_0 \nu \nabla^2 \mathbf{U} + \mu^{-1}(\nabla \times \mathbf{B}) \times \mathbf{B} + \rho \mathbf{g}$$

$$\frac{\partial \mathbf{B}}{\partial t} = \nabla \times (\mathbf{U} \times \mathbf{B}) + \eta \nabla^2 \mathbf{B} \qquad (2.2)$$

$$\frac{\partial T}{\partial t} + \mathbf{U} \cdot \nabla T = \kappa \nabla^2 T + \epsilon \qquad (2.3)$$

19

$$\nabla \cdot \mathbf{U} = \nabla \cdot \mathbf{B} = 0 \qquad (2.4)$$

where $\mathbf{U}$ is the fluid velocity, $\mathbf{B}$ is strictly speaking the magnetic induction, but will be referred to throughout as the magnetic field, T is the temperature, P is the pressure, Ω is the angular velocity, $\mathbf{r}$ is the position vector, ρ is the density including correction due to buoyancy and $\mathbf{g}$ is the acceleration due to gravity. The other constant parameter, not defined in Table 1.1, is ϵ, the heating due to internal sources. Before embarking on the non-dimensionalisation some of the terms can be replaced using assumptions of the model. We take $\mathbf{1}_\xi$ to represent the unit vector in the ξ direction. The core rotates with uniform angular velocity about the z-axis, therefore $\Omega = \Omega \mathbf{1}_z$, gravity acts radially inwards giving $\mathbf{g} = -g\mathbf{r}$ ($\mathbf{r} = r\mathbf{1}_r$), and the density in the buoyancy term can be expressed as $\rho = \rho_0(1 - \alpha(T - T_r))$, where T_r is some reference temperature at which $\rho = \rho_0$. Note that the unit vector $\mathbf{1}_z$ has spherical polar coordinates $(\cos\theta, -\sin\theta, 0)$. Using a suitable vector identity the centrifugal force, $\Omega \times (\Omega \times \mathbf{r})$ can be replaced by the term $-\nabla(\frac{1}{2}(\Omega \times \mathbf{r})^2)$, which can then be incorporated into the pressure gradient term $(-\nabla P)$, on the left hand side of (2.1). The resulting pressure term, $P_R = P/\rho_0 - \frac{1}{2}(\Omega \times \mathbf{r})^2$, is often referred to as the reduced pressure.

The outer core gap width, $L = r_o - r_i$, where r_i and r_o are the inner and outer core radii respectively, is chosen as the length scale for non-dimensialistion, while the magnetic diffusion timescale, $\tau = \tau_\eta$, is chosen as the timescale. In addition, the pressure is scaled by $2\Omega\eta$, the magnetic field by $(2\Omega\eta\mu_0\rho_0)^{1/2}$, the temperature by βL, where β is the average temperature gradient across the outer core (see Appendix C), and the velocity by η/L. Substituting for the non-dimensionalisation, the momentum equation becomes:

$$Ro\,(\partial\mathbf{U}/\partial t + (\mathbf{U} \cdot \nabla)\mathbf{U}) + \mathbf{1}_z \times \mathbf{U} = \qquad (2.5)$$

$$-\nabla P_R + E\nabla^2\mathbf{U} + (\nabla \times \mathbf{B}) \times \mathbf{B} + qRaT\mathbf{r}.$$

At this stage we would like to define some of the important forces which appear in

this equation. We have the Coriolis force $\mathbf{1}_z \times \mathbf{U}$, the Lorentz force $(\nabla \times \mathbf{B}) \times \mathbf{B}$, the viscous force $E\nabla^2\mathbf{U}$, and finally the buoyancy force $qRaT\mathbf{r}$. The definition of q will be given after discussion of the Heat equation. The other non-dimensional parameters which appear in (2.5) are,

$$Ro = \frac{\eta}{2\Omega L^2}, \quad E = \frac{\nu}{2\Omega L^2}, \quad Ra = \frac{\alpha\beta gL^2}{2\Omega\kappa}, \qquad (2.6)$$

the Rossby number, Ekman number and modified Rayleigh number respectively. The Ekman number can be thought of as the ratio of the viscous to the Coriolis force, and so in a rapidly rotating system, where we would expect the Coriolis force to be dominant, this parameter should take a small value. Substitution of the values given in Table 1.1 confirms that both Ro and E do indeed take small values in the Earth's core ($O(10^{-9})$ and $O(10^{-15})$ respectively), see also Poirier (1994).

At this point we would like to define one other parameter, which does not arise in our equations but is of use in the discussion which will follow. The Elsasser number,

$$\Lambda = \frac{B^2}{2\Omega\mu_0\rho_0\eta} \qquad (2.7)$$

can be thought of as a measure of the Lorentz force relative to the Coriolis force, where B in this case is some typical field strength. This parameter can be especially useful since it gives a measure of B relative to the scale $(2\Omega\eta\mu_0\rho_0)^{1/2}$.

Substituting the non-dimensionalisation into the remaining equations gives:

$$\frac{\partial\mathbf{B}}{\partial t} = \nabla \times (\mathbf{U} \times \mathbf{B}) + \nabla^2\mathbf{B} \qquad (2.8)$$

$$\frac{\partial T}{\partial t} + \mathbf{U} \cdot \nabla T = q\nabla^2 T + \hat{\epsilon} \qquad (2.9)$$

$$\nabla \cdot \mathbf{U} = \nabla \cdot \mathbf{B} = 0 \qquad (2.10)$$

where $\hat{\epsilon}$ can be thought of as the non-dimensional heating. A new parameter has appeared in the heat equation, the Roberts number,

$$q = \frac{\kappa}{\eta}, \qquad (2.11)$$

21

Again by substituting the values given in Table 1.1 into (2.11) we also find that q takes a very small value in the Earth's core, of $O(10^{-5})$.

2.2.1 Parity

It can sometimes be convenient to impose a particular parity on the solutions. Since the geomagnetic field is dominated by the dipole part, then usually dipolar symmetry is imposed, with **B** anti-symmetric about the equator. The components of the magnetic field then have the following symmetry,

$$(B_r, B_\theta, B_\phi)(r, \theta, \phi) = (-B_r, B_\theta, -B_\phi)(r, \pi - \theta, \phi). \tag{2.12}$$

Mathematically speaking, we could equally well impose the opposite, quadrupolar symmetry, but if either fixed parity for the magnetic field is imposed, then the flow **U** must be symmetric about the equator to be able to satisfy the induction equation (2.8). Additionally, convection in rapidly rotating systems is known to be dominantly symmetric in the presence of a dipolar magnetic field. The temperature T is also usually chosen to be symmetric about the equator. The assumption of fixed parity increases the calculation speed, allowing either solutions to be run for longer, or at higher truncation. This is the approach adopted in Model 1 (see Appendix A), using dipolar symmetry. There may be good reason, however, not to impose either fixed symmetry, because the interaction between dipole and quadrupole modes has been observed to play an important role in satisfying Taylor's constraint (Jault 1996), and in triggering reversals of the magnetic field (Glatzmaier and Roberts 1995a,b). This is the approach adopted in Model 2 (see Appendix B).

2.2.2 Boundary conditions

Even though E is very small, viscous effects must become important in narrow boundary (Ekman) layers at the CMB and the ICB if no-slip boundary conditions are applied to the flow, **U** (see for example Greenspan 1968), with the flow reduced to zero over a

very short distance. The viscous term in (2.5) becomes important when $\nabla^2 = O(E^{-1})$, and so these Ekman layers have thickness $O(E^{1/2})$. At the CMB, the usual $\mathbf{U} = \mathbf{0}$ condition can be applied, but since the inner core is free to rotate, then at the rigid ICB the axisymmetric velocity of the fluid is,

$$\Omega_i r \sin \theta \, \mathbf{1}_\phi, \tag{2.13}$$

where Ω_i is the inner core rotation rate. Note that stress-free boundary conditions could also be applied using the following condition,

$$U_r = \frac{\partial}{\partial r} \left(\frac{U_\theta}{r} \right) = \frac{\partial}{\partial r} \left(\frac{U_\phi}{r} \right) = 0. \tag{2.14}$$

This means that viscous effects will not be so important near the boundaries, and Kuang and Bloxham (1997) have argued that it better models the force balance in the core (see Chapter 5). Although both of these choices are possible in both of the models which we use, no-slip boundary conditions are exclusively employed throughout.

We have explicitly chosen the boundary conditions for the magnetic field $\mathbf{B}$ in our physical set up of the model. A finitely conducting inner core has its own diffusive time scale of order a few thousand years, and so the magnetic field in the inner core does not adjust instantaneously to the magnetic field in the outer core. This means that the magnetic field in the inner core is not solely determined by changes at the boundary but by its own past history as well, and so it must also be included in the calculation. An appropriately modified induction equation now has to be solved for the magnetic field in the inner core and a value has to be assigned to Σ, the ratio of inner core to outer core electrical conductivity (usually taken to be unity). For a perfectly conducting ($\Sigma = \infty$) or perfectly insulating ($\Sigma = 0$) inner core this is not the case, it is sufficient just to impose the appropriate boundary conditions. For a perfectly conducting inner core, there is no magnetic field in the inner core at all, while for a perfectly insulating inner core the magnetic field in the inner core adjusts instantaneously to changes on

the boundary. For finite $\Sigma \neq 0$ then

$$[\mathbf{B}] = [\mathbf{1}_n \times \mathbf{E}] = \mathbf{0}, \quad [\mathbf{1}_n \cdot \mathbf{J}] = 0 \tag{2.15}$$

at the ICB, where $[\cdot] =$ represents the difference in the quantities across the ICB, $\mathbf{1}_n$ is the unit vector normal to the boundary, and $\mathbf{E}$ is the non-dimensional electric field (Kuang and Bloxham 1999). Since the mantle is assumed to be perfectly electrically insulating, there are no sources of magnetic field, and so at the CMB,

$$[\mathbf{B}] = \mathbf{0}, \quad \mathbf{1}_n \cdot \mathbf{J} = 0. \tag{2.16}$$

Lastly for the temperature, either isothermal ($T = T_0$) or fixed heat flux ($dT/dr = 0$) boundary conditions can be adopted at either boundary, but we will deal exclusively with isothermal boundary conditions.

2.2.3 Inner core rotation

With a finitely conducting inner core, the inner and outer cores are electromagnetically coupled, giving rise to a magnetic torque on the inner core. This torque gives rise to a solid body rotation of the inner core, which must be determined as part of the solution. The method of solution depends on the assumptions in the model. For a perfectly conducting or insulating inner core there can be no electromagnetic torque on the inner core. With the inner core constrained to rotate about the same axis as the mantle, the following relation holds at $r = r_i$,

$$U_r = U_\theta = 0, \quad U_\phi = \Omega_i r \sin\theta \tag{2.17}$$

The angular momentum equation of the inner core is

$$C \frac{d\Omega_i}{dt} = \Gamma \tag{2.18}$$

where C is the polar moment of inertia and Γ is the total axial torque on the inner core,

$$\Gamma = E \int r \frac{\partial}{\partial r} \left(\frac{U_\phi}{r} \right)_{r=r_i} r_i \sin\theta \, dS + \int (B_\phi B_r)_{r=r_i} r_i \sin\theta \, dS, \tag{2.19}$$

24

(Glatzmaier and Roberts 1996c). There are two approaches depending on whether or not inertia is included in the problem. If the moment of inertia of the inner core is included, then this equation has to be time stepped forward in a similar fashion to the other equations. If inertia is not included then the total torque on the inner core must be zero. The inner core rotation can then be obtained at each time step by using (2.19). These approaches are discussed in more detail in Appendices A and B. In the most general case the inner core would be free to tilt about the vertical axis, meaning that U_θ and U_ϕ are not identically zero at $r = r_i$. However this tilt-over motion is unlikely to be significant, and so it makes sense to consider rotation only about the vertical axis.

2.3 MHD flow in a rapidly rotating system

2.3.1 Non-magnetic flows

Since the system is rapidly rotating, the Coriolis force is a dominant term in the momentum equation. In the absence of buoyancy and Lorentz forces (2.5) reduces to the geostrophic balance,

$$\mathbf{1}_z \times \mathbf{U} = -\nabla P \qquad (2.20)$$

Taking the curl of this equation and using (2.10) gives the *Taylor-Proudman theorem*:

$$\frac{\partial \mathbf{U}}{\partial z} = 0 \qquad (2.21)$$

In other words the dominance of the Coriolis force means that the motions are independent of the co-ordinate in the direction of the rotation axis. The fluid moves in (Taylor) columns of constant height. In our spherical geometry the only motions satisfying (2.21) take the form,

$$U_\phi(s)\, \mathbf{1}_\phi \qquad (2.22)$$

25

where (s, ϕ, z) are cylindrical polar co-ordinates, and are called geostrophic flows. Since this flow is solely azimuthal, it cannot transport heat outwards and so cannot be directly driven by buoyancy. Therefore convective motions cannot satisfy the Taylor-Proudman theorem exactly in a spherical container. They do however satisfy it to leading order in an asymptotic expansion in powers of E resulting in the scaling,

$$\frac{\partial}{\partial z} \ll \frac{\partial}{\partial \phi}, \frac{\partial}{\partial s}. \tag{2.23}$$

In the linear system, Roberts (1968) and Busse (1970) predict convection in the form of rolls with axes parallel to the rotation axis. The geometry constrains $\partial/\partial z$ to be $O(1)$, and gives

$$\frac{\partial}{\partial \phi} = O(E^{-1/3}), \quad \frac{\partial}{\partial s} = O(E^{-2/9}). \tag{2.24}$$

These short length scales result in increased dissipation, with an increase in the minimum temperature gradient required for convection with rotation rate according to

$$Ra_c \propto E^{-1/3} \tag{2.25}$$

It is clear from (2.25) that rotation has a strong inhibiting effect on convection, despite the fact that no work has to be done against the Coriolis force since $\mathbf{U} \cdot (\mathbf{\Omega} \times \mathbf{U}) \equiv 0$. Although in the weakly nonlinear regime Soward (1977) has shown that some problems exist with the scalings in this linear analysis, experimental and numerical work (Carrigan and Busse 1983, Cardin and Olson 1994) has shown that the basic result in (2.23) holds. More recently, Zhang has performed numerical and analytical studies in a spherical geometry, finding different forms of convection depending on the Prandtl number, $Pr = \nu/\kappa$.

For a spherical shell, the cylindrical surface co-axial with the rotation axis, which touches the inner core, is often referred to as the tangent cylinder. Hollerbach and Proctor (1993) show that the flow inside the tangent cylinder does not match smoothly

26

to the flow outside when $E = Ro = 0$. This discontinuity becomes a viscous shear layer when $E > 0$, and is generally present even with no inner core rotation. The shear layer has very similar features to a Stewartson (1966) layer with innermost thickness $O(E^{1/3})$ (see Hollerbach 1994a). The introduction of a magnetic field smooths out the shear layer, and with a sufficiently strong magnetic field there is no noticeable feature associated with the tangent cylinder (Hollerbach 1994a,b).

2.3.2 MHD flows

To aid our visualisation of the effect of the Lorentz force, we can use a vector identity to write it in the form,

$$(\nabla \times \mathbf{B}) \times \mathbf{B} = (\mathbf{B} \cdot \nabla)\mathbf{B} - \nabla(\frac{1}{2}\mathbf{B}^2). \tag{2.26}$$

The first term can be interpreted as a magnetic tension, while the second as the gradient of a magnetic pressure. The magnetic pressure can be absorbed into a total pressure $(P + \frac{1}{2}\mathbf{B}^2)$, the magnetic tension force means that the magnetic field lines act like stretched wires (see for example Glatzmaier and Roberts 1997). In a perfectly conducting fluid ($\eta = 0$), then (2.2) reduces to

$$\frac{\partial \mathbf{B}}{\partial t} = \nabla \times (\mathbf{U} \times \mathbf{B}). \tag{2.27}$$

Alfvén's *frozen-flux theorem*, that in a perfectly conducting fluid the magnetic field evolves as if the field lines move with the fluid, can be derived from this equation. For ($\eta \neq 0$), the effects of diffusion allow the magnetic field to slip through the fluid. The extent to which this occurs is measured by the ratio of the advective to diffusive terms on the right-hand side of (2.2), which is more commonly known as the magnetic Reynolds number R_m. If this parameter is large, as it usually has to be for dynamo action to occur, then the frozen flux theorem is still a useful aid to interpretation.

These two results imply that a magnetic field (in the absence of rotation) will act to inhibit convection in the following way. In a highly conducting fluid, the convecting

fluid will drag the magnetic field lines along with it, these field lines will be stretched and so will act to oppose the motion. In other words extra work has to be done against the Lorentz force. In the limit of high field strength ($Q \gg 1$), where Q is the Chandrasekhar number (see Chandrasekhar 1961), then a linear analysis gives

$$\frac{Ra_c}{E} \propto Q. \tag{2.28}$$

Note that Ra_c/E and $Q = \Lambda/E$ are both independent of Ω. Acting individually rotation and a magnetic field inhibit the onset of convection. Let us now assume that we have a system that is already rapidly rotating, and to which we wish to add a magnetic field. If a weak field is added then surprisingly it has a destabilising effect, with $Ra_c \propto 1/\Lambda$. For a magnetic field which is stable, Ra_c reaches a minimum at $\Lambda = O(1)$, and then as Λ is increased further the magnetic field reverts to its expected stabilising role, with $Ra_c \propto \Lambda$ (Chandrasekhar 1961). The leading order balance is now *magnetostrophic*

$$\mathbf{1}_z \times \mathbf{U} = -\nabla P + (\nabla \times \mathbf{B}) \times \mathbf{B}. \tag{2.29}$$

When $|\mathbf{B}|$ is small, (2.20) and hence (2.21), will remain approximately true. As the magnetic field strength increases, the geostrophic constraint is relaxed, and so the inhibiting effect of rotation on the convection is reduced. At low magnetic field strengths this dominates the inhibiting effect of the magnetic field itself. For a long time the minimum of Ra_c at $O(1)$ was seen as the favoured location in parameter space for the dynamo to operate. At lower field strengths the dynamo may be unstable, as a small increase in Λ leads to a small decrease in Ra_c and consequently an increase in convective vigour and hence magnetic field generation, amplifying the small initial increase. This adds to the difficulties inherent in the hydrodynamic dynamo problem, as it is not possible to find a strong-field (Earth-like) solution by following a series of bifurcations from a non-magnetic, non-convecting system to a convecting, non-magnetic system, to a convecting system with self-generated magnetic field (Hollerbach 1996). For $\Lambda > O(1)$, the increase in Ra_c with Λ leads to a stable dynamo, since a small

28

increase in Λ leads to a small increase in Ra_c, giving weaker field generation. All of the preceding analysis relies on the magnetic field being stable. Magnetic fields characteristic of the Earth's core are unstable when $\Lambda > O(10)$ (Zhang and Fearn 1994), and at least when $q = O(1)$, there is a smooth transition from thermally driven convection at low Λ to magnetically driven convection at higher Λ, with no minimum of Ra_c at $\Lambda = O(1)$. Magnetic instabilities are an important component of the dynamo problem, as they may be able to explain reversals and other features of the geomagnetic field. They will not be discussed any further here, for a more detailed review see Fearn (1998).

2.4 Force balance in the momentum equation

Intuition suggests that the very low geophysical values of E and Ro should allow viscous and inertial effects to be neglected. Setting $E = Ro = 0$ in (2.5) gives the magnetostrophic approximation

$$\mathbf{1}_z \times \mathbf{U} = -\nabla P + (\nabla \times \mathbf{B}) \times \mathbf{B} + qRaT\mathbf{r}. \tag{2.30}$$

Taylor (1963) first realised that this approximation leads to the following constraint on the magnetic field, for an incompressible fluid,

$$\int_{C(s)} ((\nabla \times \mathbf{B}) \times \mathbf{B})_\phi \, dS = 0. \tag{2.31}$$

Here $C(s)$ is the surface of a cylinder of radius s, co-axial with the rotation axis. The system has the freedom to satisfy this constraint through a component of the azimuthal flow, the 'arbitrary' geostrophic flow, that is otherwise undetermined. A solution satisfying (2.31) is known as a Taylor state, which is characterised by being independent of viscosity. The quantity on the left hand side of (2.31) can be interpreted as the net magnetic torque acting on the the cylinder of radius s in the ϕ direction. When the torque is weak this can be balanced by the viscous drag on the ends of the

cylinder, the viscosity only being effective in the Ekman boundary layers. When the viscosity remains important in the Ekman boundary layers, the preceding discussion has to be modified. Equation (2.30) is only satisfied in the interior of the fluid, and there is the possibility of flow along the Ekman layer and into the top and bottom of $C(s)$. Taylor's constraint is then modified and now gives an expression for the geostrophic flow

$$U_G = (2E)^{-1/2}(1 - s^2)^{1/4} \int_{z_B}^{z_T} \langle (\nabla \times \mathbf{B}) \times \mathbf{B} \rangle_\phi \, dz \qquad (2.32)$$

(see for example Fearn 1994), where $\langle \cdot \rangle$ represents the azimuthal average. Various modifications to this expression have been investigated. Of most relevance here is the work of Jault (1995) who included inertia to obtain the alternative relation

$$2Ro \frac{\partial U_G}{\partial t} + \frac{E^{1/2}U_G}{(1 - s^2)^{3/4}} = \frac{1}{2^{1/2}(1 - s^2)^{1/2}} \int_{z_B}^{z_T} \langle (\nabla \times \mathbf{B}) \times \mathbf{B} \rangle_\phi \, dz \qquad (2.33)$$

Restoring inertia was found to reduce the stiffness associated with (2.32), allowing evolution to a steady state satisfying Taylor's constraint. Returning to (2.32), for $Ra > Ra_c$ an infinitesimal solution will grow, initially exponentially. The presence of the factor $E^{-1/2}$ means that when $|\mathbf{B}| = O(E^{1/4}), U_G = O(1)$ while all other nonlinear interaction terms are $O(E^{1/2})$, and so the effect of the geostrophic flow is the first nonlinear effect to become important. When the shear has increased sufficiently such that $Ra_c = Ra$, the solution stops growing and we have an equilibrated finite amplitude solution with $|\mathbf{B}| = O(E^{1/4})$, called an Ekman state, which clearly depends on the viscosity.

As Ra is increased it is possible for the nonlinear effect of U_G to modify this Ekman state to a Taylor state. In this way the amplitude of $\mathbf{B}$ can increase, while U_G remains $O(1)$. This transition is often referred to as the Malkus-Proctor scenario (Malkus and Proctor 1975). Nonlinear $\alpha^2\omega$-dynamo (see below) and magnetoconvection studies have found both Ekman states and transitions to Taylor states. However, the Ekman states found with the $\alpha^2\omega$-dynamos have a characteristic axisymmetric magnetic

field amplitude of $O(E^{1/4})$, while those found in the magnetoconvection studies have an $O(1)$ axisymmetric magnetic field. This difference in characteristic magnetic field amplitudes, makes obtaining an Ekman state in a fully self-consistent hydromagnetic dynamo impossible. Nonlinear dynamos can either be in the weak-field regime, for which the magnetic field amplitude is too small to have any effect on the convection, or in the strong-field regime, for which the magnetic field is $O(1)$, strong enough to distort the flow. A fully self-consistent dynamo can be viewed as consisting of the interaction between an $\alpha^2\omega$ dynamo and magnetoconvection. The axisymmetric magnetic field (and flow) used in the magnetoconvection part of the calculation is that being generated in the $\alpha^2\omega$-dynamo, with the resulting non-axisymmetric flow (and magnetic field) used in turn to drive the $\alpha^2\omega$-dynamo. It is the fact that α and ω no longer need to be prescribed which makes the dynamo self-consistent. As stated above, a magnetoconvective Ekman state is characterised by an $O(1)$ magnetic field, while the $\alpha^2\omega$-dynamo Ekman state is characterised by an $O(E^{1/4})$ magnetic field. The prescription of α and ω required to give an $O(1)$ magnetic field must be completely different to that which will give an $O(E^{1/4})$ magnetic field. Thus an Ekman state is not possible in the fully self-consistent dynamo. This means that an alternative route to a Taylor state must be found, and as yet none of the models have been successful in obtaining one. An alternative to the Taylor state is the viscosity-dependent model-Z dynamo, see Braginsky (1994).

2.5 Numerical models

2.5.1 $2\frac{1}{2}D$ approximation

As we have already stated the equations governing the geodynamo are nonlinear. Our objective is to produce a model, with some simplifying assumptions, which incorporates the influence of the magnetic field on the convection. The ϕ dependence of $\mathbf{B}, \mathbf{U}$ and T are obtained using an $e^{im\phi}$ term in the non-axisymmetric components (see Appendix

A), where the parameter, m, is the azimuthal wavenumber. There is also an axisymmetric component, for which $m = 0$. The $2\frac{1}{2}D$ approximation requires that only one non-zero value of m is included in addition to the axisymmetric part of the solution. In this case, a nonlinear term ($U \times B$) say, will involve the interaction of two axisymmetric components, to produce an axisymmetric component, two non-axisymmetric components, and two separate interactions between an axisymmetric component and a non-axisymmetric component. The term produced consists of an axisymmetric part, an $e^{im\phi}$ part and an $e^{2im\phi}$ part. However this last part, which arises from the interaction of the non-axisymmetric components, cannot be retained, as only one value of m is included. The axisymmetric part arising from this interaction, is included. When the non-axisymmetric terms are small this is a good approximation, but when the sizes of the two components are comparable, the neglect of any terms cannot be rigorously justified. However the interaction between just one non-axisymmetric mode and the axisymmetric fields is sufficient to overcome the constraint of Cowling's theorem, generating poloidal and toroidal field and producing a self-consistent dynamo. Of course, the value of m must be chosen a priori, and so the system is not allowed to choose its preferred wavenumber. The choice is based on the range of nonlinearly stable values obtained in magnetoconvection studies, and that which best fits the geomagnetic data.

2.5.2   Busse-Zhang dynamos

We use two different models, called Model 1 and Model 2 (see Appendices A and B), to study the (BZ) type dynamo solutions discussed in Chapter 1. The name arises from the similarities to the convective dynamo solutions first studied by these authors (Zhang and Busse 1989). In this parameter regime $E \approx 10^{-3} - 10^{-4}$ and $q = 1 - 10$, and initially solutions were obtained with imposed dipolar symmetry. Typical solutions obtained in this regime are comprehensively described in Sarson et. al. (1998b), but the main features are summarised below. The flow is (energetically) dominated

by non-axisymmetric convection, in the form of azimuthally drifting rolls aligned with the rotation axis, lying outside the tangent cylinder, with relatively weak zonal flows. This form of convection is suggestive of Ekman suction at the boundaries, which in turn suggests that the z-component of the flow is viscously limited, and that Taylor's constraint plays some role in the determination of the solutions. Dynamo action occurs for $Ra \gtrsim Ra_c$, and the magnetic fields produced do not satisfy Taylor's constraint very well, and have energy approximately equi-partitioned between non-axisymmetric and axisymmetric parts, with the total magnetic energy always several orders of magnitude larger than the total fluid energy, see Appendix A for a definition. Even although the magnetic field can vary appreciably with time, no reversals are observed. The velocity and magnetic field are approximately co-rotating, and the inner core rotation rate is very small ($\approx 0.1^o$/year). For solutions which exhibit rather chaotic time dependence, the structure of the solution can vary appreciably with time, but the large scale features are retained. Qualitatively similar behaviour is observed for different buoyancy source distributions. When the dipolar symmetry constraint is removed a quadrupolar magnetic field component, of similar magnitude, is generated, but the flow remains predominantly symmetric and the nature of the convection is relatively unchanged. The magnetic energy remains roughly equi-partitioned between the axisymmetric and non-axisymmetric parts. No solutions with fixed polarity, dipole or quadrupole, are obtained once the mixed symmetry solution has been established. This suggests that the bifurcation to mixed symmetry must occur before the system attains the strong field branch. The time dependence of the solutions has now become somewhat irregular, and whereas the magnetic field with dipolar symmetry was of fixed polarity, the magnetic field now undergoes frequent reversals. Although the solution structure will now look somewhat different, the large scale features are similar to those obtained with imposed symmetry, and are again consistent with time. Therefore, important aspects of the dynamo mechanism must be contained in the imposed symmetry problem, de-

33

spite having to view the solutions obtained as non-physical. Removing the symmetry constraint does not reliably help in satisfying Taylor's constraint. This is also true for (GR) type dynamo solutions, which may in fact satisfy this constraint more poorly, despite having a lower value of E. All the preceding solutions did not include any inertial effects, i.e. they were obtained with $Ro = 0$. The effect of including the inertial term to (BZ) dynamo solutions with mixed symmetry is discussed in Chapter 5.

2.5.3 Hyperdiffusivity

This method has been used for about thirty years in global climate modelling, astrophysical fluid dynamics and turbulence simulations. Hyperdiffusivity is a numerically prescribed form of enhanced diffusion, acting on the small length scale features. From a physical point of view, the enhanced diffusivity accounts for the presumed greater tendency for small-scale (resolved) eddies to transfer heat and momentum to sub-grid scale eddies.

There are many different approaches, but in numerical dynamo models, which are typically in spherical geometry and use spherical harmonics as expansion functions, the (constant) kinematic viscosity ν in (2.1) is replaced by a term, $\nu(l)$, which depends on the spherical harmonic degree l. This also applies to the thermal diffusivity, κ, and the magnetic diffusivity, η. As l is increases, the associated solution length scale becomes shorter, and so the diffusive operator increases in magnitude, and consequently the short length scales in the θ and ϕ directions are strongly damped while the longer length scales experience relatively less diffusion. The main benefit of using this method in numerical dynamo models, is that lower 'headline' values of E and q can be obtained, without numerical instabilities caused by the small length scales. Although the physical basis for using hyperdiffusivity appears reasonable, it is not clear how to interpret different forms of the hyperdiffusive operator, meaning that it is a somewhat artificial parameterisation. Recent work looking at the linear dynamic effects of hyper-

viscosity has suggested that it acts in a similar fashion to an imposed magnetic field on non-magnetic convection, destroying the dynamic features and altering the rotational control on the convective system (Zhang and Jones 1997). The controlling effect of the hyperviscosity results in large scale convection with or without a strong magnetic field. The main features of this pattern show very little change, even when the magnetic field is rapidly varying. A hyperdiffusive Ekman number of 10^{-5} acts more like an effective Ekman number (based on the size of the preferred wavenumber) of 10^{-2}. In addition, despite the small value of E, Taylor's constraint is not well satisfied, suggesting that the form of the hyperviscosity is playing a major role in controlling the geostrophic flow. Clearly the effect of hyperdiffusivity in numerical dynamo models merits further study.

2.5.4 Different approaches

The preceding sections have examined the development of self-consistent convectively driven dynamo models. Numerical solution of such models has only become possible in the past five years. Previously, to make any progress simpler approaches had to be adopted, and are still adopted, in order to obtain tractable problems. One such method is to study magnetoconvection, for which a magnetic field, representative of the magnetic field in the core, is imposed to a convecting system. As has previously been seen, care must be exercised in the choice of imposed magnetic field. Alternatively an arbitrary flow can be prescribed, and the induction equation, with suitable boundary conditions, solved to obtain the magnetic field. This approach is known as kinematic dynamo theory (Roberts 1994), and although the problem is linear, three dimensional solutions of (2.2) are still required. Parameterising the effects of non-axisymmetric flows and fields, allows the use of simpler axisymmetric models. To justify this approach one has to assume that the non-axisymmetric components are small or that the turbulent non-axisymmetric components have a small length scale. The induction

35

equation becomes:

$$\frac{\partial \mathbf{B}}{\partial t} = \nabla^2 \mathbf{B} + \nabla \times (\alpha \mathbf{B}) + \nabla \times (\mathbf{U} \times \mathbf{B}) \qquad (2.34)$$

where α parameterises the structure of the small scale helical turbulence, and $\mathbf{U}$ and $\mathbf{B}$ are the axisymmetric flow and field respectively. In its most general form, α is a tensor quantity, but is usually assumed to be a scalar for simplicity. It is convenient to consider magnetic field generation by fluid flow in terms of two different effects, the α-effect and the ω-effect. The former generates poloidal field from toroidal field via small scale helical turbulence, while the latter generates toroidal field from poloidal field via large scale zonal flow. The definitions of poloidal and toroidal can be found in Appendix A. Rather than prescribe the flow, (2.34) and (2.1) can now be solved for the flow and magnetic field. A dynamo which is driven entirely by the α-effect is referred to as an α^2 dynamo. If a strong differential rotation, parameterised by the ω-effect, is also prescribed then either an $\alpha\omega$ dynamo or an $\alpha^2\omega$-dynamo is produced, depending on the magnitude of the α-effect included. Unfortunately this approach is not very satisfactory for two reasons. Firstly, the distribution of turbulence in the outer core is still not well known, meaning that the prescribed α-effect distribution is somewhat arbitrary. Secondly, the behaviour of the dynamos produced is dependent on the form of the α-effect prescribed.

Chapter 3

The influence of Rayleigh number and azimuthal wavenumber

3.1 Introduction

In this Chapter we will use Model 1 to investigate the effects of varying Ra at two different values of m. Using this simpler model allows a very thorough examination of parameter space. Before discussing the results, we will take some time to explain our choice of survey parameters. There are five parameters which can be varied in this particular model, E, q, Ra, χ (the inner-outer core radius ratio), and m, and these are all defined in Chapter 2. We are also free to choose the inner core to outer core conductivity ratio (Σ). In most dynamo models this is set to be unity, and there is no good reason to believe that this ratio is any more than about 2 in the Earth. For some selected solutions, we have varied this parameter and found very little change on the solution obtained. Therefore it seems sensible to fix this parameter to be identically 1. The value of χ is well known for the Earth at present (≈ 0.33), but is continually changing over time as the inner core freezes from the outer core fluid. The effect on the solution of changing this parameter is discussed in Chapter 4. Geophysical values of the other parameters are less well known. As we have already seen, E is likely to take a very small value in the Earth's core, and q is also believed to be small, although using turbulent diffusivity values may make it closer to $O(1)$. Even the most

optimistically high estimate of E, and certainly the (molecular) value of q will be beyond computational reach for some time to come. For this reason, the values of both E and q which can be prescribed are severely restricted. However, for a solution obtained at small χ, a limited survey of values of E was possible (see Chapter 4). This leaves Ra as the only other practical parameter to vary, in this model, for a given value of m. Initial calculations with our model have assumed that thermal buoyancy arises from a specific type of heat source, uniform internal heating. We also examine whether a different heat source distribution has any effect on the behaviour observed, for a range of values of Ra.

3.1.1 Azimuthal wavenumber

The $2\frac{1}{2}D$ approximation focusses on the axisymmetric ($m = 0$) magnetic field, and fully retains the interaction of one ($m \neq 0$) mode of the non-axisymmetric magnetic field with this field. Provided that the axisymmetric magnetic field is reasonably strong, then this interaction is the most important role of the non-axisymmeric field, since the nonlinear interaction of non-axisymmetric modes produces an axisymmetric field, and a ($2m$) mode of the non-axisymmetric field. The latter term is excluded by the approximation.

Convection onsets at a single preferred wavenumber, meaning that with a judicious choice of m, the $2\frac{1}{2}D$ approximation is reasonable for $Ra \approx Ra_c$. As the value of Ra becomes increasingly super-critical, a different wavenumber will become preferred, making the approximation less appropriate since our value of m is fixed. Bearing this in mind, all our results are for $Ra \lesssim 5Ra_c$. Since the value of m has to be chosen in advance, it is important to establish what influence this choice has on the results. Previous geodynamo studies using this model, have normally chosen to prescribe the value $m = 2$, since this is the preferred value with a strong, but stable magnetic field (Zhang and Jones 1994). Observational evidence also supports this choice for m.

38

3.1.2 Ekman number

To summarise what we know so far about this parameter. In a rapidly rotating system ($E \ll 1$), as appropriate for the Earth, boundary layers of $O(E^{1/2})$ exist at the core-mantle boundary and the inner-core boundary. Additionally, in non-magnetic systems the convective length scale and the shortest length scale of the Stewartson layer structure is $O(E^{1/3})$. Since we have to numerically resolve these features, there is a limit to the size of E, which can be prescribed. Despite having a longer length scale, the convective structure may turn out to be more difficult to resolve than the boundary layer structure. This is because the boundary layers are at a known location, and suitable expansion functions (see Appendix A) or a suitably stretched grid (for finite difference schemes) can be used to help resolve these features. However, the location of the convective rolls emerges as part of the solution making these methods less effective. Whatever method is used adopting the geophysical value for E is impractical, and so an alternative approach is required.

Since E is expected to be very small, the magnetostrophic approximation ($E = 0$) could be adopted (see Chapter 2). So far, progress has been restricted to the nonlinear magnetoconvection problem (Fearn et al. 1994, Walker and Barenghi 1997a,b, 1998, 1999 and Walker 1998) due to difficulties associated with applying Taylor's constraint (Walker et al. 1998). The only other option is to adopt a larger finite value of E and hope that this value at least lies in the correct asymptotic regime. Much better progress has been made following this approach, which is the one adopted here. There is still then a question as to whether or not hyperdiffusivities should be used to obtain a lower value of E. The consequences and benefits of using this method are detailed in Chapter 2. Without hyperdiffusivity the best value of E which can normally be obtained is $O(10^{-4})$. However Glatzmaier and Roberts have obtained a very high resolution solution at $E = 10^{-6}$, without using hyperdiffusivity. This solution required

60 times the number of spherical harmonics, demonstrating the severe computational limitations involved in working with small E. Consequently, both Glatzmaier and Roberts and Kuang and Bloxham include hyperdiffusivity, but with different forms of $\nu(l)$. However, tractable values of E are still at best of $O(10^{-6})$, many orders of magnitude above a realistic value. The question of how low E must be taken to be representative of the Earth's core remains an open one.

3.1.3 Roberts number

Using a geophysical value of q also raises several major difficulties in numerical calculations. The form of the buoyancy term in equation (2.5) suggests that qRa may be an important quantity for dynamo action, and this has been verified by nonlinear dynamo models (Glatzmaier and Roberts 1995a,b and Jones et al. 1995). For $q = O(10)$, there is onset of dynamo action at values of Ra only modestly above Ra_c. However, at lower values of q, dynamo action only occurs when convection is highly supercritical. Another problem arises out of the effect of differential rotation. From linear studies, differential rotation, measured by the magnetic Reynolds number, $R_m = UL/\eta$, has a stabilising effect when $R_m = O(q)$. As R_m increases, convection typically becomes more concentrated in a region of width $O(R_m/q)^{-1/3}$ when $R_m \gg q$, for $q \leq O(1)$, see Fearn and Proctor (1983a,b). With the requirement that $R_m \geq O(1)$ for dynamo action, it is clear that small values of q pose potentially serious numerical resolution problems. Difficulties have also arisen from the small q limit in finding nonlinear magnetoconvective solutions satisfying Taylor's constraint (Soward 1986, Skinner and Soward 1988, 1990) and in linear magnetoconvection studies (Zhang and Jones 1996).

3.1.4 Rayleigh number

This is the control parameter and is a measure of the temperature gradient driving convection. Its value is unknown for any planetary interior, and so it is important to

determine how the choice of Ra influences the type of solution obtained. Our definition of Ra (see Appendix C) is reasonable for a uniform distribution of heat sources, but if a different heat source distribution is used, then care should be exercised in interpreting the results at a given value of Ra. This is examined in more detail in 3.2.2.

3.2   Calculations

Detailed surveys are performed with a fixed radius ratio $\chi = 0.33$ and conductivity ratio $\Sigma = 1$, for $m = 2$ and $m = 4$. We choose the values of E and q to be 10^{-3} and 10 respectively. These are the parameter values used to produce the Run (A) and Run (B) solutions described in Jones et al. (1995), and so will allow comparison with previous work. Run (A) is a weak field dynamo with $Ra = 85$, while Run (B) is a strong field dynamo with $Ra = 50$. Both of these solutions are also obtained in this study (see Figure 3.1). In all of the following discussion, any mention of the Run (A) and Run (B) solutions, is understood to refer explicitly to these solutions. Temporal resolution is such that τ (see Chapter 2) corresponds to 50,000 time steps. Spatially, 36 radial and 24 latitudinal modes are included for the flow, with 18 radial and 18 latitudinal modes included for the magnetic field and temperature. This level of truncation and temporal resolution is consistent with previous calculations performed using the code, although selected cases have also been run with higher truncations and lower time steps, giving good agreement with the original results. A version of the code using an adaptive time stepping algorithm (see Appendix A) has also been used to investigate any areas of parameter space where very rapid fluctuations in the coefficients occur.

At each value of Ra, the code is run until any transient behaviour has decayed. Once the temporal behaviour of the solution has been established, the value of Ra is changed, and a new calculation performed. This temporal behaviour is obtained by writing out the leading flow and magnetic field coefficients, in addition to other useful quantities, every 50 time steps. Representative plots are given in Figures (3.2, 3.4 etc.)

for the axisymmetric magnetic field. The quantities given in the legend are BI, and AI the axisymmetric inner core toroidal and poloidal magnetic fields, with BO and AO their counterparts in the outer core. Each time the coefficient values are written out, the magnetic and fluid energies are calculated and also written out, giving not only a view of how the real magnetic field and flow are varying with time, but also providing a measure of the average strength of the magnetic field and flow produced. This is obtained by taking the energy data from one diffusion time, redimensionalising to obtain the energy in Joules, and then taking the average over this diffusion time. The procedure is only really appropriate when the solution is settled, and more than one data set is tested for each solution to ensure that the result obtained is representative.

The structure of the magnetic field, flow and temperature produced are also plotted. It is usually desirable to plot the axisymmetric and non-axisymmetric structure separately. The full solution is written out at the end of the calculation, giving not only a snapshot of the magnetic field and flow structure, but also providing a set of initial conditions for further calculations. For the axisymmetric quantities we take a meridional slice and plot the toroidal magnetic field contours, the poloidal magnetic field lines, the angular velocity contours, the meridional streamlines, and the temperature contours. In this chapter we shall only be concerned with the magnetic field plots (e.g. Figure 3.3), however in Chapter 4 we shall also examine the flow structure. Appendix A provides a more detailed description of all the diagnostic procedures. For each figure, the parameter values given in the captions correspond to the plots from top to bottom in the figures.

Table 3.1a: The full range of calculations performed in varying Ra with $m = 2$ (Strong-field).

Ra	Comments	$Em(J)$	$Ef(J)$	Run Time
22	No convection	0	0	2.00
25	Steady convection	0	1.89×10^{15}	2.00
28	Steady convection	0	5.40×10^{15}	4.00
29	Convection	0	6.67×10^{15}	4.00
30	Strong vacillatory magnetic field	1.48×10^{21}	5.25×10^{15}	4.00
32	Strong vacillatory magnetic field	1.97×10^{21}	7.23×10^{15}	2.00
34	Strong quasi-periodic magnetic field	2.28×10^{21}	8.63×10^{15}	2.00
40	Strong quasi-periodic magnetic field	3.04×10^{21}	1.43×10^{16}	2.00
45	Strong chaotic magnetic field	3.53×10^{21}	1.96×10^{16}	2.00
50	Strong chaotic magnetic field	4.08×10^{21}	2.39×10^{16}	2.00
52	Strong chaotic magnetic field	4.32×10^{21}	2.56×10^{16}	2.00
55	Strong chaotic magnetic field	4.54×10^{21}	2.82×10^{16}	2.00
59	Strong chaotic magnetic field	4.91×10^{21}	3.26×10^{16}	2.00
60	Strong chaotic magnetic field	4.97×10^{21}	3.38×10^{16}	2.99
65	Strong field decays	0	6.72×10^{16}	1.98
70	Steady convection	0	7.63×10^{16}	1.00
75	Steady convection	0	8.54×10^{16}	1.00
80	Steady convection	0	9.46×10^{16}	1.00
85	Weak oscillatory magnetic field	4.15×10^{19}	1.04×10^{17}	8.00

Table 3.1b: The full range of calculations performed in varying Ra with $m = 2$ (Weak-field).

Ra	Comments	$Em(J)$	$Ef(J)$	Run Time
30	Steady convection	0	7.98×10^{15}	1.00
32	Steady convection	0	1.07×10^{16}	1.00
34	Steady convection	0	1.36×10^{16}	1.00
40	Steady convection	0	2.30×10^{16}	1.00
45	Steady convection	0	3.14×10^{16}	1.00
50	Steady convection	0	4.01×10^{16}	1.00
52	Steady convection	0	4.37×10^{16}	1.00
53	Weak oscillatory magnetic field	8.11×10^{18}	4.54×10^{16}	2.00
55	Weak oscillatory magnetic field	2.66×10^{19}	4.89×10^{16}	2.00
60	Weak oscillatory magnetic field	2.98×10^{19}	5.79×10^{16}	12.00
65	Steady convection	0	6.72×10^{16}	1.00
70	Steady convection	0	7.63×10^{16}	1.00
75	Steady convection	0	8.54×10^{16}	2.00
80	Steady convection	0	9.46×10^{16}	1.00
85	Weak oscillatory magnetic field	4.14×10^{19}	1.04×10^{17}	2.00
90	Oscillatory magnetic field	2.09×10^{20}	1.11×10^{17}	2.00
95	Strong chaotic magnetic field	6.46×10^{20}	1.15×10^{17}	2.00
100	Strong chaotic magnetic field	9.41×10^{20}	1.22×10^{17}	2.00

Table 3.2: The full range of calculations performed in varying Ra with $m = 4$ (Strong-field).

Ra	Comments	$Em(J)$	$Ef(J)$	Run Time
15	No convection	0	0	2.00
20	Steady convection	0	4.47×10^{13}	2.00
21	Steady convection	0	1.15×10^{15}	2.00
22	Strong vacillatory magnetic field	6.88×10^{20}	3.02×10^{15}	4.00
23	Strong vacillatory magnetic field	8.87×10^{20}	4.77×10^{15}	2.00
24	Strong vacillatory magnetic field	9.81×10^{20}	6.20×10^{15}	2.00
25	Strong vacillatory magnetic field	1.01×10^{21}	7.36×10^{15}	6.00
26	Strong vacillatory magnetic field	9.45×10^{20}	8.36×10^{15}	2.00
27	Strong vacillatory magnetic field	1.90×10^{20}	6.78×10^{15}	3.50
28	Strong vacillatory magnetic field	2.35×10^{20}	8.44×10^{15}	10.00
29	Strong vacillatory magnetic field	3.15×10^{20}	8.17×10^{15}	2.00
30	Strong vacillatory magnetic field	4.17×10^{20}	7.87×10^{15}	2.00
32	Strong vacillatory magnetic field	4.74×10^{20}	1.13×10^{16}	6.00
34	Strong vacillatory magnetic field	5.23×10^{20}	1.46×10^{16}	2.00
40	Strong vacillatory magnetic field	6.39×10^{20}	2.36×10^{16}	5.00
45	Strong vacillatory magnetic field	8.03×10^{20}	3.07×10^{16}	4.00
50	Strong chaotic magnetic field	6.72×10^{20}	4.24×10^{16}	5.00
52	Steady convection	5.92×10^{20}	4.69×10^{16}	2.00
55	Strong vacillatory magnetic field	7.20×10^{20}	5.19×10^{16}	2.00
60	Strong vacillatory magnetic field	9.32×10^{20}	6.09×10^{16}	3.00
65	Strong vacillatory magnetic field	8.47×10^{20}	7.24×10^{16}	2.00
70	Strong chaotic magnetic field	1.15×10^{21}	8.29×10^{16}	2.00
75	Strong chaotic magnetic field	2.16×10^{21}	8.70×10^{16}	2.00
80	Strong chaotic magnetic field	1.87×10^{21}	9.90×10^{16}	1.93

3.3 Results and discussion

3.3.1 Varying Ra for $m = 2$

The full range of values of Ra surveyed is presented in Tables 3.1 a,b. As can be seen from the tables, these values range from $Ra = 22$, where there is no convection or magnetic field through to $Ra = 100$ where strong, chaotic magnetic fields and convection are observed. Figure 3.1 demonstrates how the strength of the magnetic field and convection change as Ra changes, for selected values of Ra. It was previously believed that the Run (A) and Run (B) solutions were distinct, however Figure 3.1

clearly shows how they are related.

On the higher magnetic branch the dynamos are of strong field type. The time dependence of the solutions at three different values of Ra on this branch is displayed in Figure 3.2. Convection onsets at $Ra_c \approx 24$ (see Figure 3.1), and a magnetic field, with periodic time dependence (see Figure 3.2), is first generated at $Ra_m \approx 30$. A very gradual change is observed as the solution evolves to a quasi-periodic state when $Ra \approx 40$, and then to a chaotic state when $Ra \approx 50$. The corresponding axisymmetric magnetic field structures are displayed in Figure 3.3. These clearly show that, despite the increasing strength and changing time dependence, the same magnetic field structure is being maintained on this branch as Ra is increased. The evidence is particularly compelling since these structures are a snapshot of a solution which is changing with time.

If Ra is increased sufficiently then dynamo action ceases abruptly when $Ra \approx 65$ and the magnetic field switches to the lower branch (see Figure 3.1). This branch is characterised by solutions with weak or zero magnetic fields. The flow solution now jumps to a higher branch (Figure 3.1), on which the convection is steady, uninfluenced by the weak or non-existent magnetic fields. This branch is followed by the flow as Ra is increased all the way to 100. No magnetic field is generated again until $Ra \approx 85$, where a weak magnetic field is generated. The time dependence and structure of the axisymmetric field for this solution are displayed in Figures 3.4 and 3.5, clearly showing that a new solution has been obtained. The magnetic field becomes increasingly strong and chaotic as Ra is increased further. This chaotic behaviour may be due to the fact that our value of Ra is now more supercritical and the solution is constrained to be periodic in longitude as discussed in Section 3.1.1.

If Ra is now decreased again, the solution remains on the lower magnetic and upper flow branches. At values of $Ra < 85$, the weak magnetic field exhibits exponential decay, as shown in Figure 3.4 which gives the solution for $Ra = 70$. However, at $Ra \approx$

46
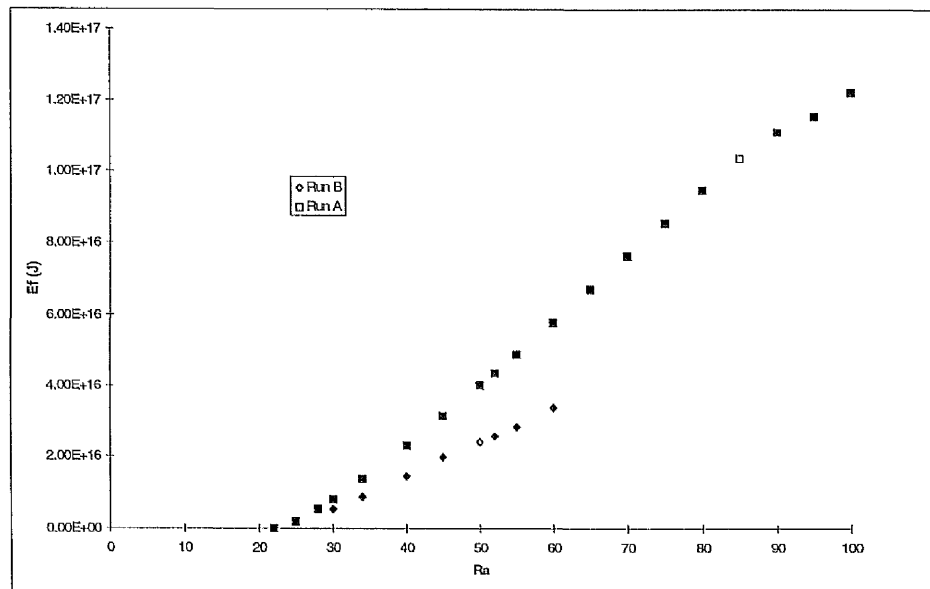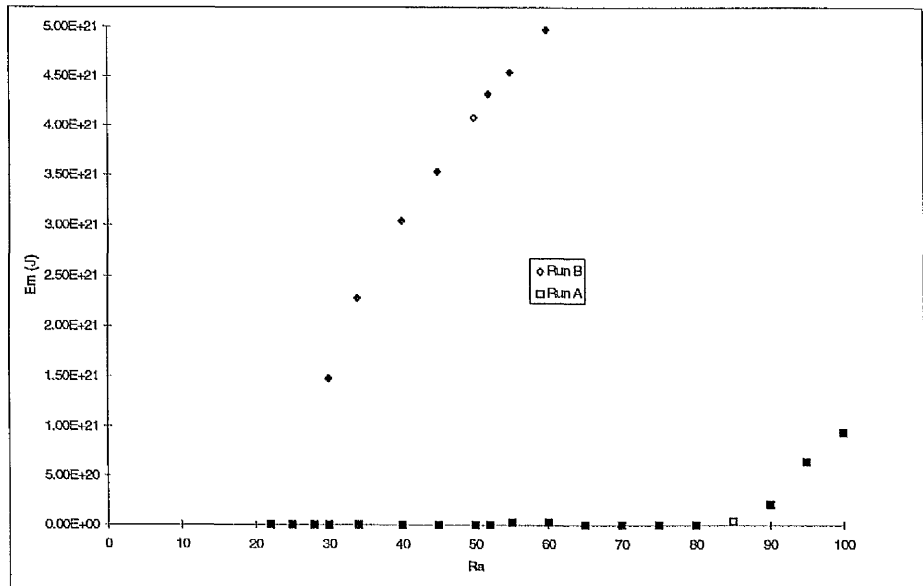
Figure 3.1: A plot of the time-averaged magnetic energy and fluid energy against Ra for $m = 2$.
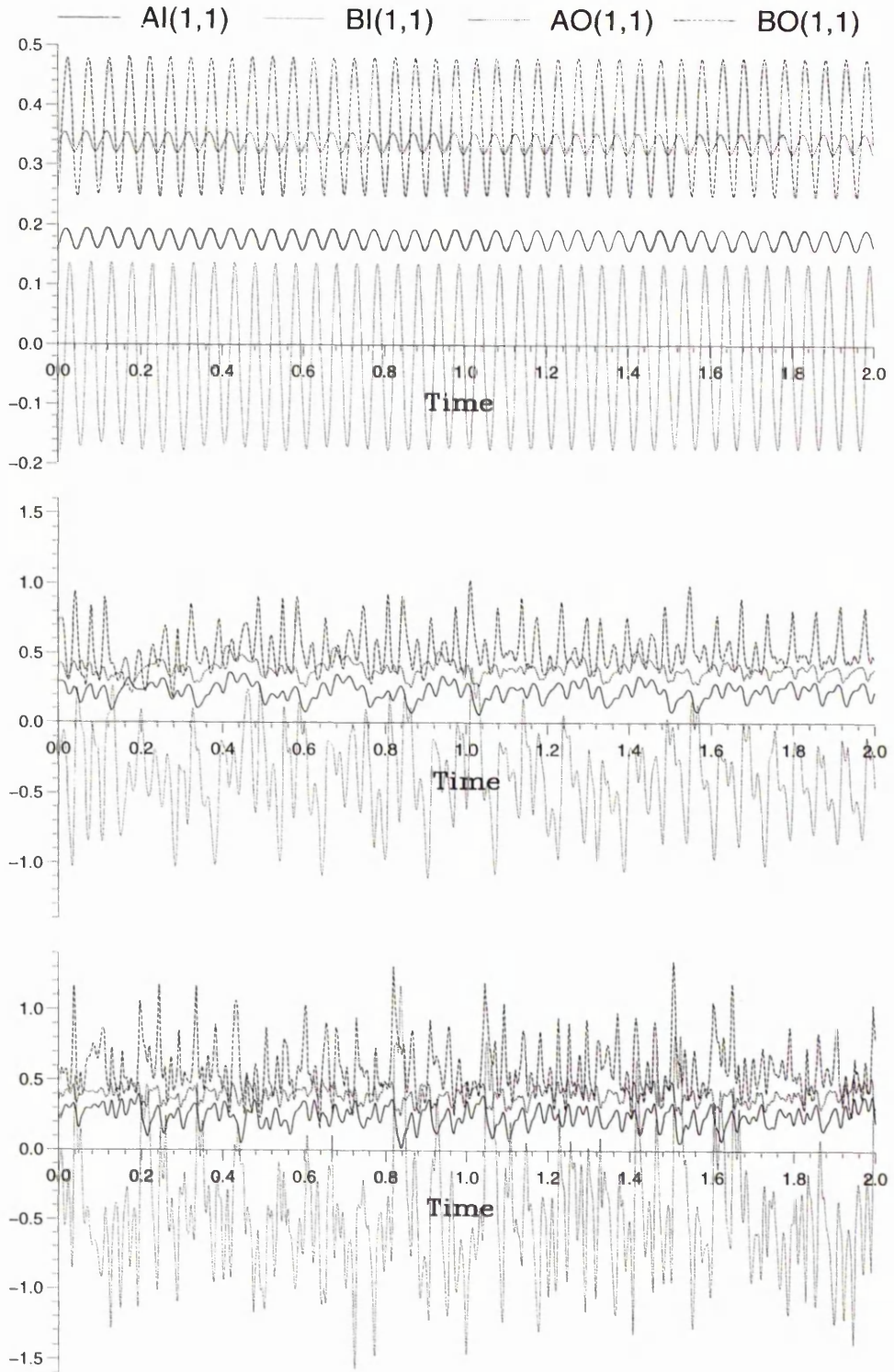
Figure 3.2: The time dependence of the axisymmetric magnetic field, for $Ra = 30$, 40 and 50 with $m = 2$.
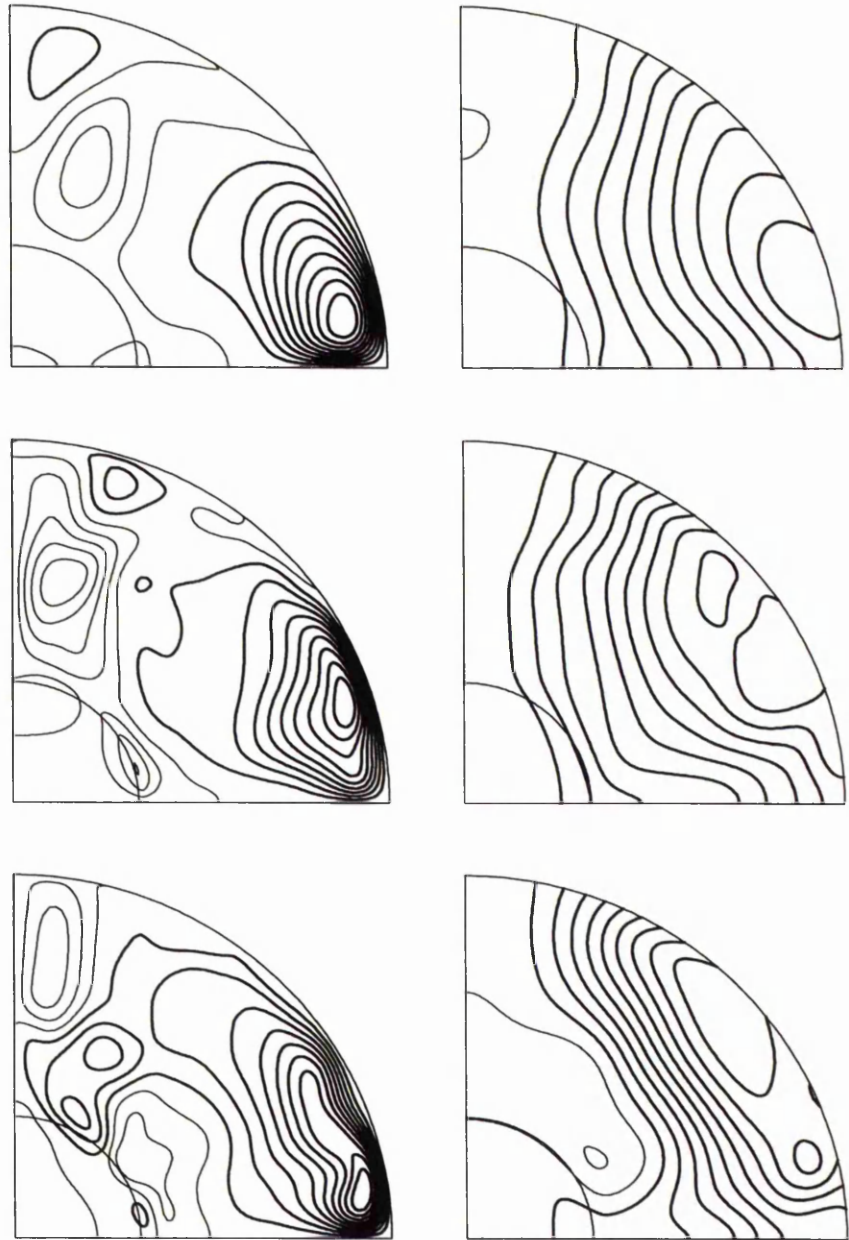
Figure 3.3: A snapshot of the axisymmetric toroidal magnetic field contours (left) and the poloidal magnetic field lines (right), for $Ra = 30$, 40 and 50 with $m = 2$.

60 a weak magnetic field is once again generated, with similar time dependence and structure (Figure 3.5) to that of the solution at $Ra = 85$. This behaviour is maintained until $Ra \approx 53$, when once again the weak magnetic field exhibits exponential decay. The structure of the corresponding axisymmetric fields is given in Figure 3.5. Clearly this is a different solution to that shown in Figure 3.3. Therefore, in the range $30 \lesssim Ra \lesssim 60$, at least two distinct solutions exist, that can be labelled strong field and weak field.

3.3.2 Different forms of driving

All of the preceding solutions have been obtained assuming uniform internal heating, but our thermally driven dynamo allows for other sources of thermal buoyancy. We may also choose differential heating, where all of the heating occurs at the ICB, or a temperature profile which is a combination of the two forms. For each form of heating the temperature at the boundaries is fixed. The mathematical details involved in choosing a different heat source are set out in Appendix C. The temperature profiles which are produced in the outer core are different in each of the different cases. For differential heating the maximum temperature gradient occurs at the ICB, and decreases outwards, whereas for internal heating the temperature gradient increases outwards, with a uniform distribution of heat sources throughout the outer core. The case of differential heating more closely resembles compositional convection, with the main source of buoyancy at the ICB. It has recently been suggested that this form of heating is more likely to give an Earth-like, dipole-dominated magnetic field, and that internal heating is less efficient for maintaining the dynamo, generally producing a quadrupole-dominated magnetic field (Kutzner and Christensen 2000). However in comparing the effect of the two forms of heating, the internal heating from the inner core was ignored, i.e. $\nabla T = 0$ at the ICB. This is a very drastic assumption, and represents a worst case scenario for internal heating. To gain further understanding of

50
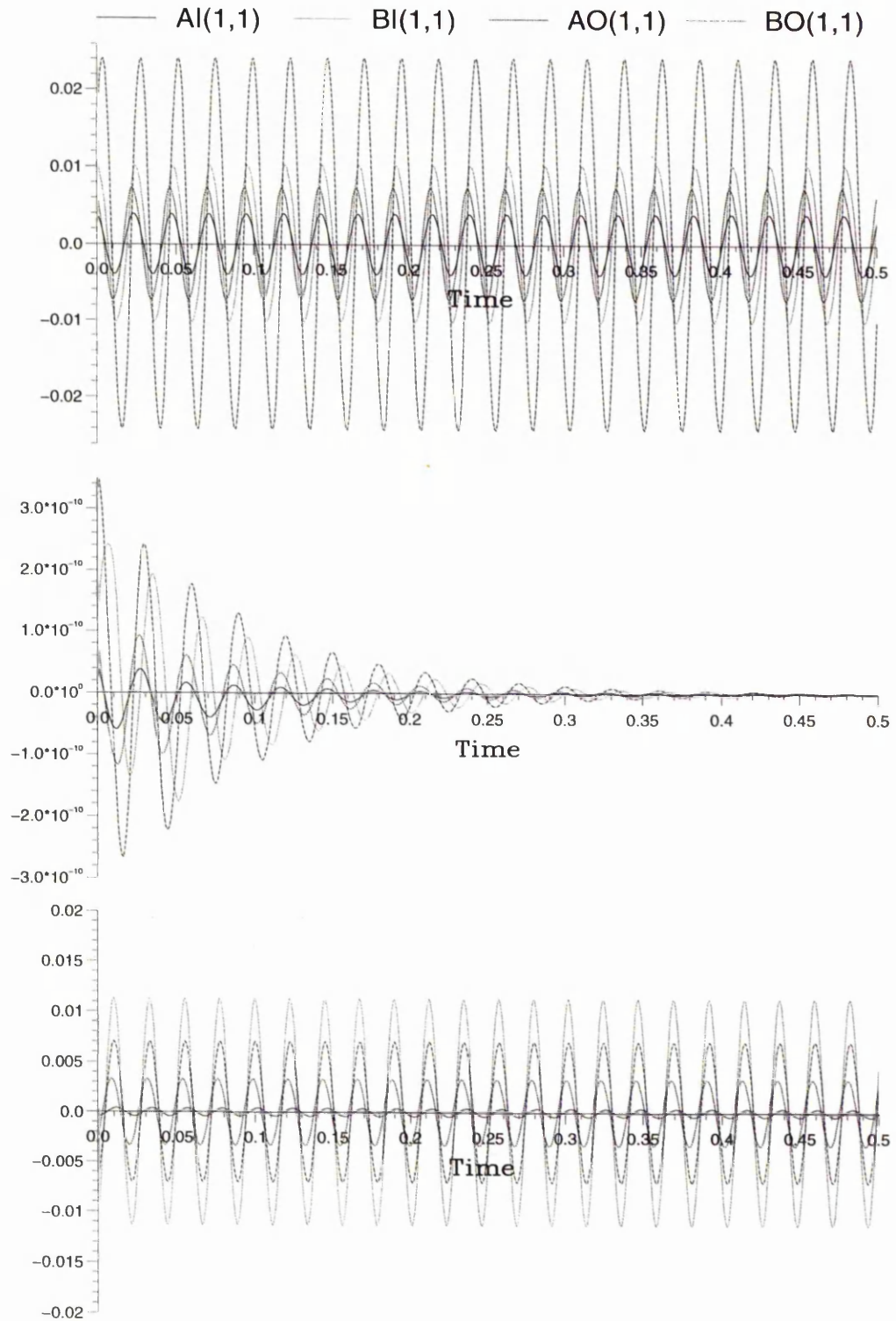
Figure 3.4: The time dependence of the axisymmetric magnetic field for $Ra = 85$, 70 and 60 with $m = 2$.
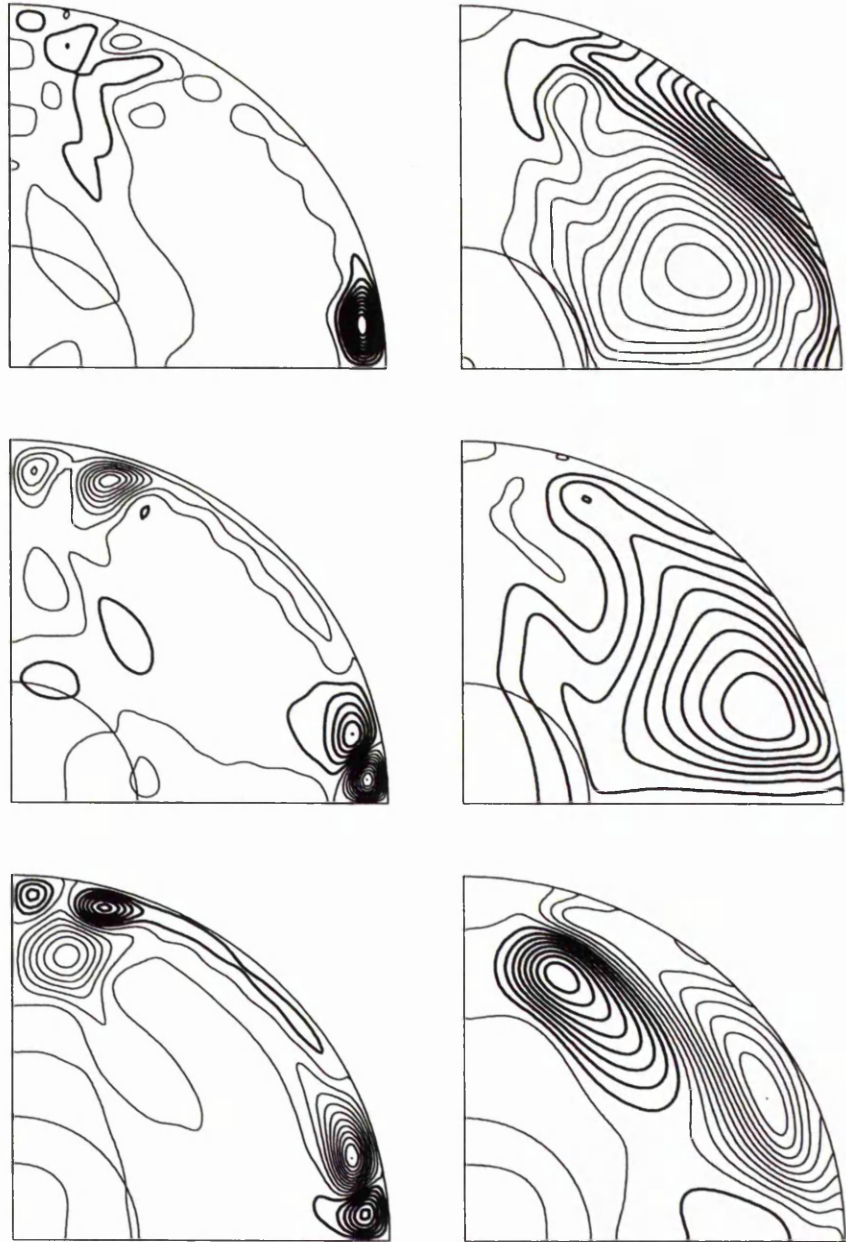
Figure 3.5: A snapshot of the axisymmetric toroidal magnetic field contours and poloidal magnetic field lines for $Ra = 85$, 70 and 60 with $m = 2$.

this important issue, we performed a study at four values of Ra, comparing the solutions obtained with uniform internal heating, differential heating, and an unperturbed temperature profile intermediate between the two. The results of our survey are neatly summarised in Figure 3.6, which shows the magnetic and fluid energies as a function of Ra.

We see that very similar behaviour is observed for each form of heating. It is also clear that the solutions obtained with differential heating have a smaller magnitude than those obtained when internal heating is present. This difference in magnitude must be interpreted in terms of our definition of Ra. The value of Ra depends upon both the temperature gradient, β and the gravitational acceleration g. In particular β is an average temperature gradient, defined to be the temperature difference between the boundaries divided by the length scale L. The case of uniform internal heating is clearly better approximated by this average value, than the case of differential heating. Additionally, in the case of internal heating β is strongest where g is strongest (at the CMB), as their magnitudes are proportional to r. Therefore the convection will be more strongly driven in this case. To aid our discussion, we introduce a parameter γ which controls the form of heating imposed (see Appendix C). Uniform internal heating corresponds to $\gamma = 1$, and differential heating to $\gamma = 0$, with γ taking values between 0 and 1. In our study we have chosen $\gamma = 0, 0.5$ and 1. Figure (3.7) provides a good comparison of the time dependence of the axisymmetric magnetic field for each form of driving at $Ra = 45$. The corresponding axisymmetric structures are given in Figure 3.8.

Aside from the caution which must be exercised in the interpretation of the Rayleigh number Ra, it seems that there is very little difference in choosing uniform internal heating or differential heating as a driving mechanism. Although our dynamo model is different to that of Kutzner and Christensen it is in approximately the same parameter regime, and so somewhat similar results would be expected. It may well be that the

53
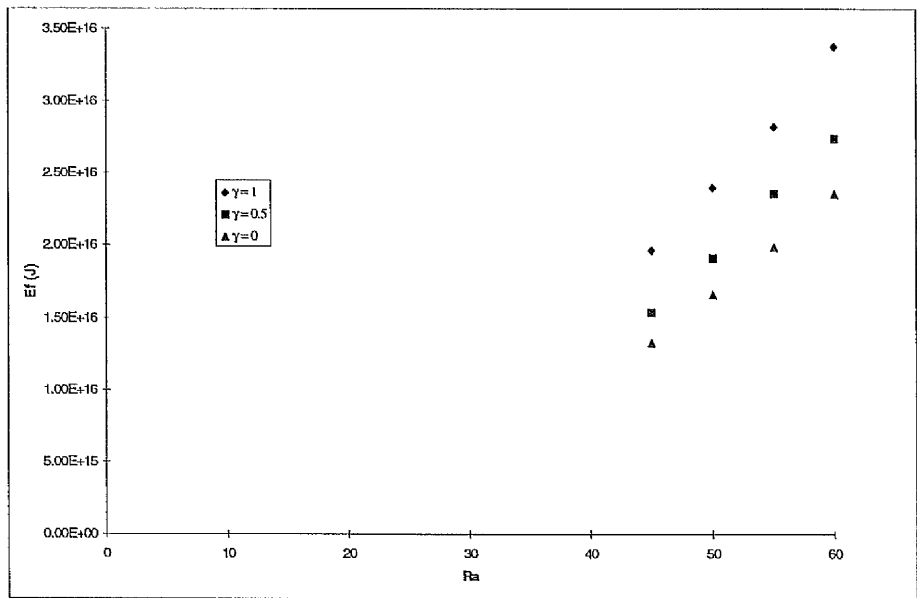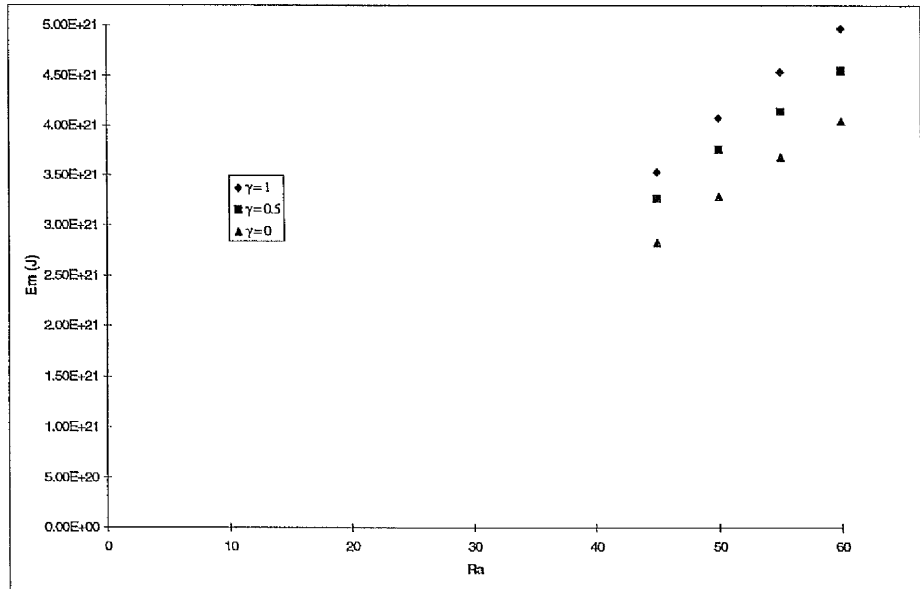
Figure 3.6: A plot of the time-averaged magnetic energy and fluid energy against Ra for three different values of γ.
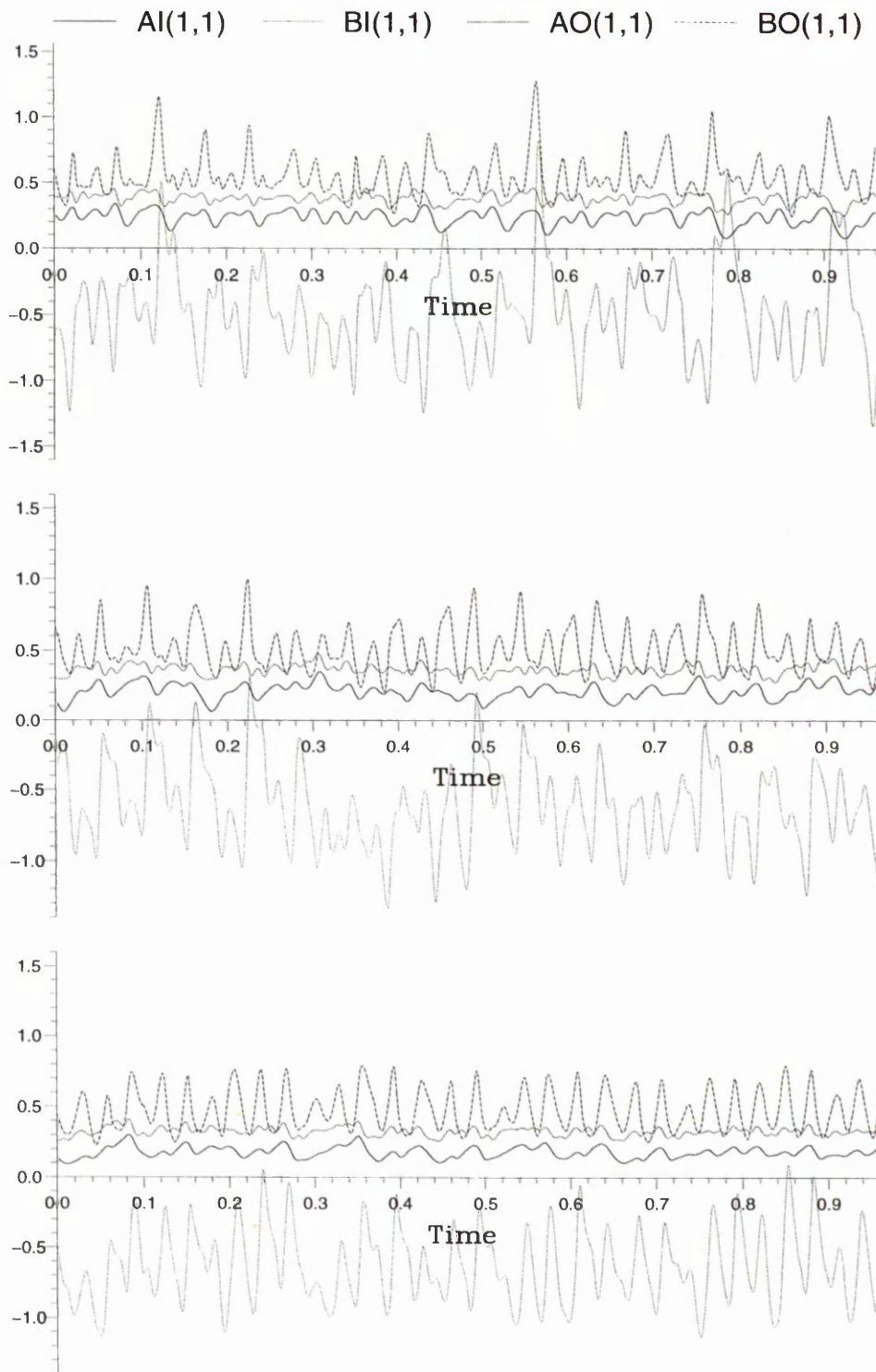
Figure 3.7: The time dependence of the axisymmetric magnetic field for, $\gamma = 1, \gamma = 0.5, \gamma = 0$, with $Ra = 45$.

55
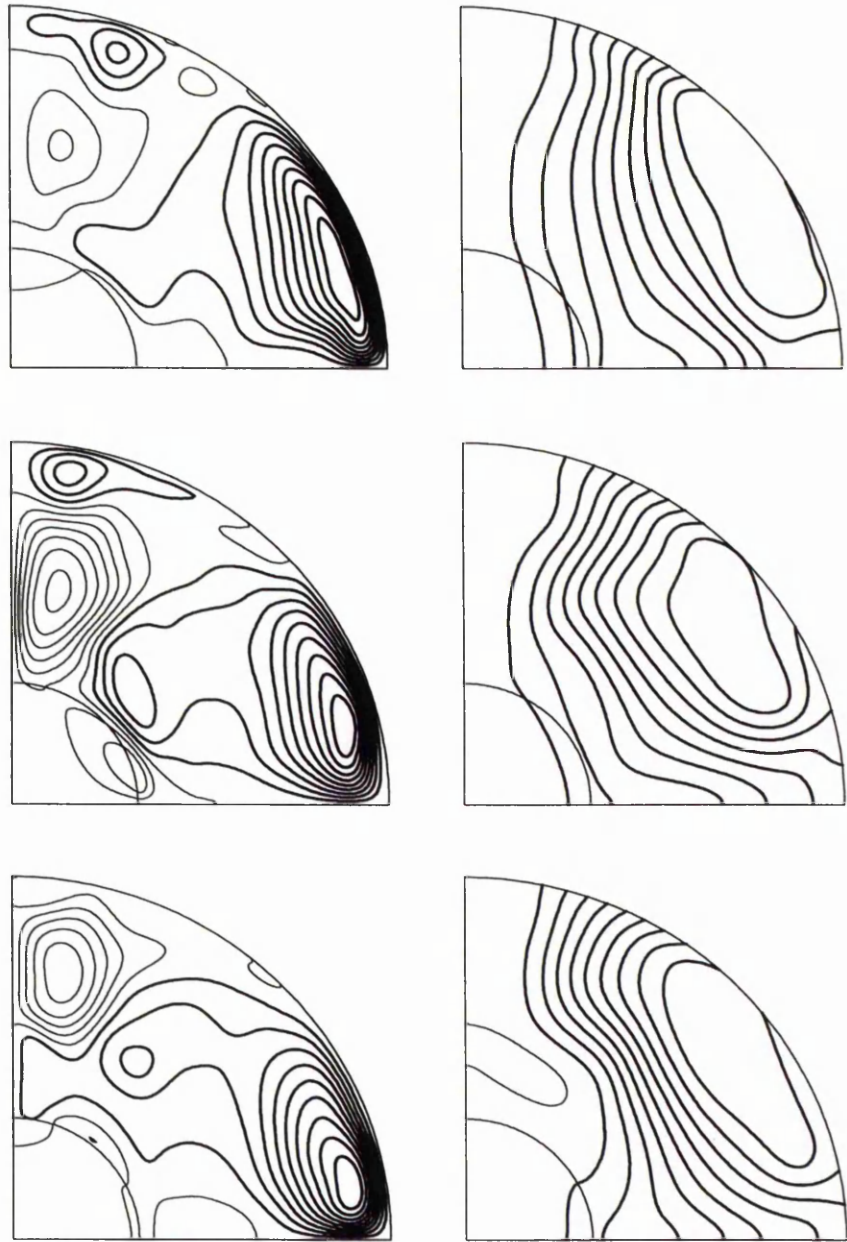
Figure 3.8: A snapshot of the axisymmetric toroidal magnetic field contours and poloidal magnetic field lines for $\gamma = 1, 0.5$ and 0 with $Ra = 45$.

very drastic internal heating assumption is responsible for the differences which they observe.

3.3.3 Varying Ra for $m = 4$

The full range of values of Ra surveyed is shown in Table 3.2. As can be seen from the table, these values range from $Ra = 15$, where there is no convection or magnetic field, to $Ra = 80$, where strong, chaotic magnetic fields and convection are observed. Figure 3.9 shows how the strength of the magnetic field and convection change as Ra changes for $m = 4$. In both cases the behaviour is clearly different to that observed for $m = 2$ (c.f. Figure 3.1). A highly irregular trend is followed by the magnetic field strength as Ra increases, but the strength of convection increases with Ra as expected. Checks performed on the averaging of the data, indicate that the different trend is not an artefact of our averaging process, described in Appendix A. Finally, note that the solution obtained when $Ra = 60$ is similar to one obtained by Sarson et al. (1997b) at the same parameter values.

An overview of the change in the time dependence of the solution as Ra increases is given in Figure 3.10. The magnetic field behaviour is mostly periodic, but extremely variable; even when Ra is changed by only a small amount, significant differences in time dependence are observed, in contrast to the behaviour observed for $m = 2$. Additionally, the magnetic fields are generally of weaker magnitude for $m = 4$, although a weak field solution is never obtained. The time dependence is initially periodic when $Ra \approx 40$, and then exhibits much more complicated behaviour when $Ra \approx 50$. The solution returns to periodic behaviour when $Ra \approx 60$ before becoming chaotic when $Ra \approx 70$ as shown in the last plot in Figure 3.10. The corresponding axisymmetric field structure for each of these solutions is shown in Figure 3.11, showing that there is a single strong field solution which remains mostly periodic, but can display very different time dependence, and ultimately becomes chaotic as Ra is increased far beyond critical.
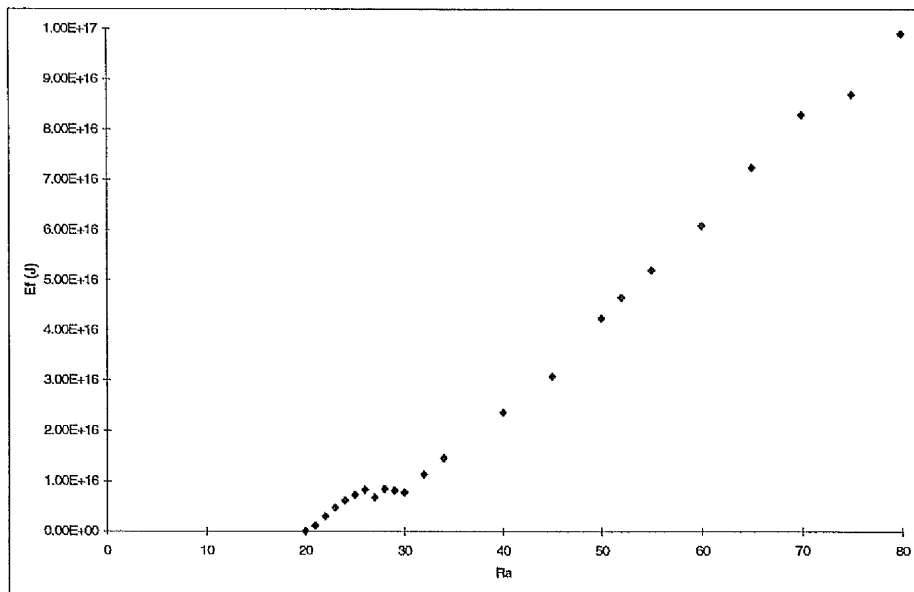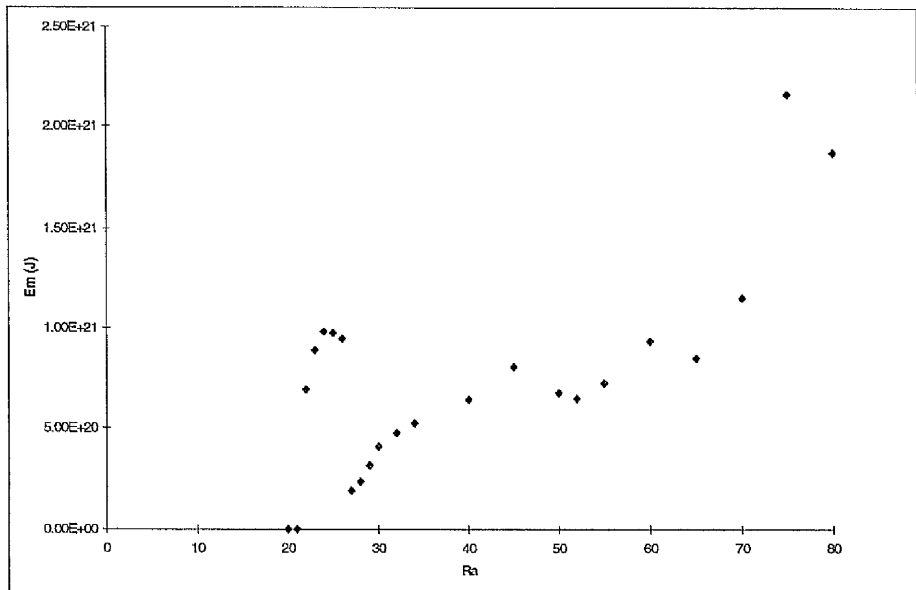
Figure 3.9: A plot of the time-averaged magnetic energy and fluid energy against Ra for $m = 4$.
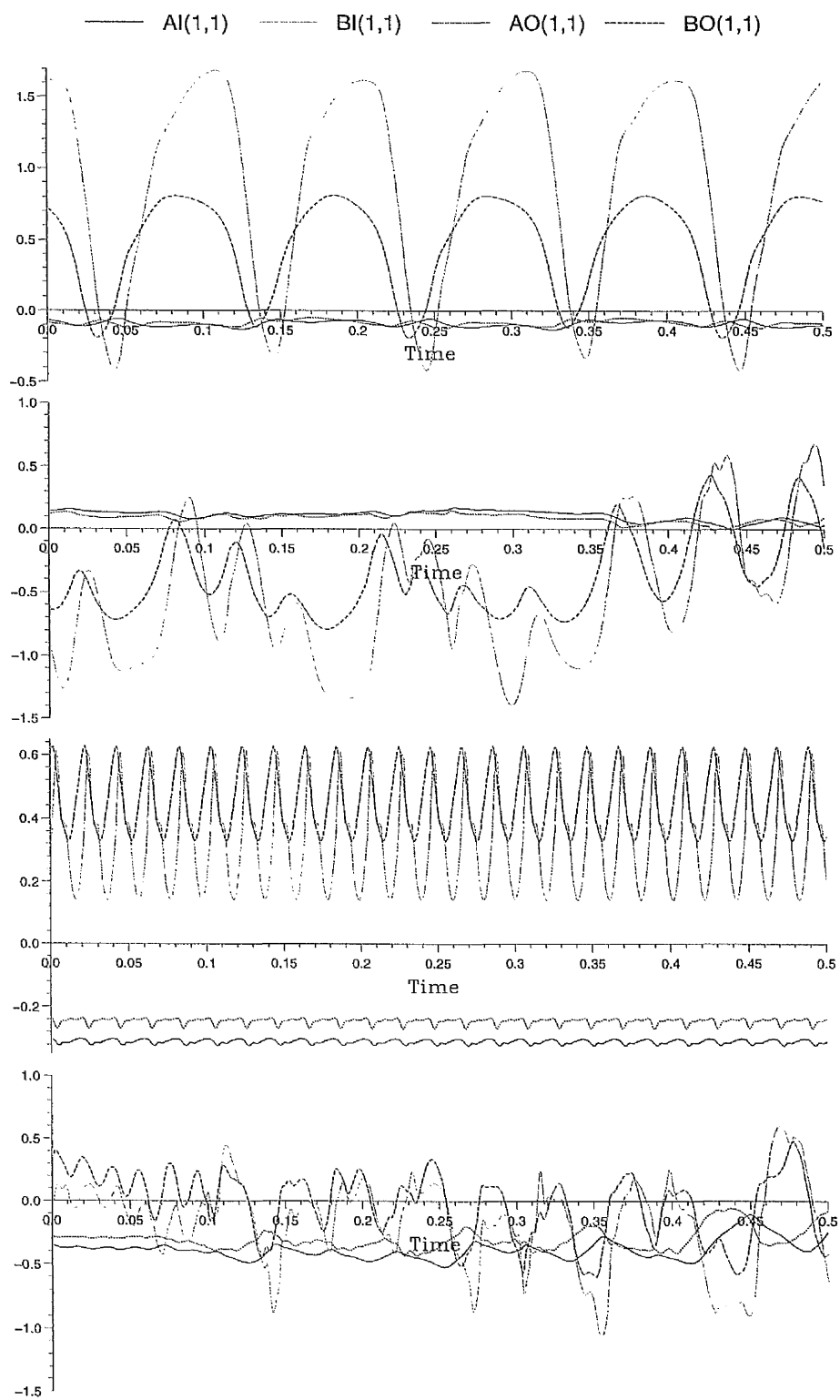
Figure 3.10: The time dependence of the axisymmetric magnetic field for $Ra = 40$, 50, 60 and 70 with $m = 4$.
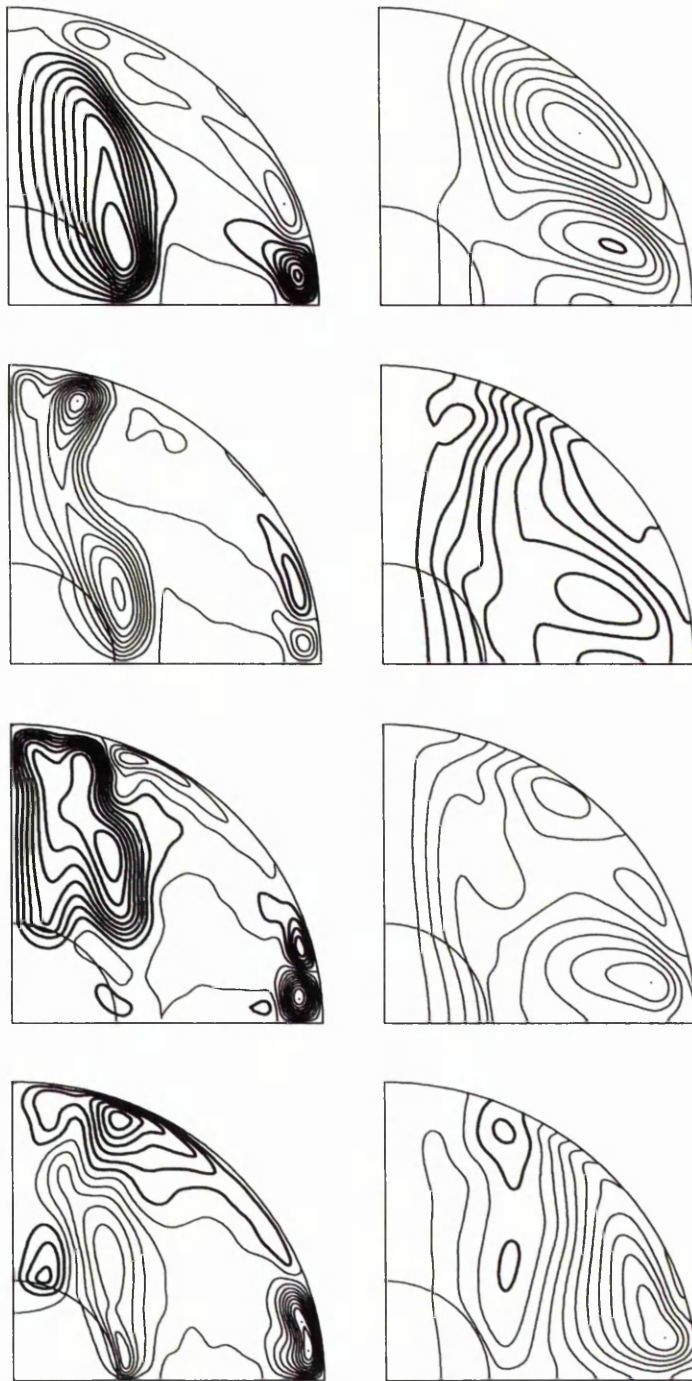
Figure 3.11: A snapshot of the axisymmetric magnetic fields for $Ra = 40, 50, 60$ and 70 with $m = 4$.

Chapter 4

The effect of varying the inner core radius

4.1 Introduction

So far, the Earth is the only planetary body for which an inner core has been directly detected. As has already been discussed, the inner core is slowly growing due to the freezing of iron from the outer core fluid at the inner core boundary. This means that the inner core radius is constantly changing. At present, the value of the radius ratio, χ, is about 0.33. A recent study suggests that the inner core first nucleated about 1700 Ma and is currently growing at a rate of about $500m/Myr$ (Labrosse et al. 1997). An inner core of radius one third the outer core radius, still only occupies 4% of the volume of the core. This led to initial dynamo models either adopting electrically insulating boundary conditions at the ICB, and so ignoring the magnetic field in the inner core, or working in a full sphere, and ignoring the presence of the inner core entirely. Hollerbach and Jones (1993a,b, 1995) showed that this neglect of the inner core was not justified. They found that a freely rotating, finitely conducting inner core had a strong impact on the core dynamics, and a stabilising effect on any generated magnetic field. Hollerbach and Jones compared the bifurcation sequence they obtained with an $\alpha\omega$-dynamo incorporating a finitely conducting inner core, to that obtained from a spherical model. They found that initially the same bifurcation sequence was

followed, but a new solution was found using the spherical shell model, whose main feature was that dynamo action was always restricted to the region just outside the tangent cylinder, regardless of inner core radius ($0.25 \leq \chi \leq 0.5$). Although the magnetic field in the outer core still exhibited a complicated time dependence, the dipole moment at the surface was periodic and of constant polarity. In the spherical model, starting from the same initial bifurcation sequence, the solutions became chaotic oscillations which reversed frequently. A similar stabilising effect has also been observed by Glatzmaier and Roberts (Glatzmaier and Roberts 1995b), who replaced a perfectly insulating inner core with one of finite conductivity. This changed the character of the magnetic field solutions from having a dipole part which reversed polarity about every thousand years, to having a dipole part of generally constant polarity, reversing only once in a 40,000 year simulation. The stabilising effect envisaged by Hollerbach and Jones, and observed by Glatzmaier and Roberts, was that a finitely conducting inner core, which has its own magnetic diffusion time, prevented very rapid fluctuations from dominating the dynamo process. In particular, a reversal could only take place when a fluctuation was large enough and lasted long enough to reverse the field in the inner core. Although they were working with an $\alpha\omega$-dynamo, this effect has also been seen in fully nonlinear dynamo models (Jones et al. 1995, Glatzmaier and Roberts 1995a,b, Sakuraba and Kono 1999). This idea has been extended by Gubbins, who argues that it is the stabilising effect of the inner core that prevents an excursion from becoming a full reversal (Gubbins 1999). Given the complexity of the geodynamo process it would be very surprising if the reversal frequency is controlled solely by the inner core. Nonetheless, the results from dynamo calculations consistently suggest that a finitely conducting inner core plays a significant role in the process. It is clearly important to study the effect of changing the inner core radius to give some idea of the possible effect of the growth of the inner core on the geodynamo, and in trying to understand the geomagnetic polarity time scale.

62

Table 4.1: The full range of calculations performed in varying χ with $m = 2$.

χ	Comments	$Em(J)$	$Ef(J)$	Run Time
0.025	Periodic magnetic field	2.62×10^{21}	1.02×10^{16}	3.73
0.05	Periodic magnetic field	2.67×10^{21}	1.10×10^{16}	3.97
0.10	Periodic magnetic field	2.90×10^{21}	1.23×10^{16}	4.00
0.15	Chaotic magnetic field	3.13×10^{21}	1.36×10^{16}	6.00
0.15	Chaotic magnetic field	3.13×10^{21}	1.38×10^{16}	6.00
0.20	Chaotic magnetic field	3.22×10^{21}	1.55×10^{16}	4.00
0.25	Chaotic magnetic field	3.44×10^{21}	1.55×10^{16}	4.00
0.30	Increasingly chaotic magnetic field	3.21×10^{21}	1.52×10^{16}	4.00
0.33	Quasi-periodic magnetic field	3.04×10^{21}	1.43×10^{16}	2.00
0.35	Almost periodic magnetic field	2.84×10^{21}	1.33×10^{16}	4.00
0.40	Periodic magnetic field	2.07×10^{21}	9.76×10^{15}	4.00
0.45	Steady convection	0	9.36×10^{15}	2.00
0.50	Steady convection	0	1.21×10^{15}	2.00

4.2 Calculations

In this Chapter only we will present our results in terms of new non-dimensional parameters, based on the outer core radius, r_o, instead of the gap width L. The non-dimensional parameters affected are τ, E and Ra. The following relations can be used to convert between the different parameter sets,

$$E_n = (1 - \chi)^2 E, \quad \tau_n = \frac{1}{(1 - \chi)^2}\tau, \quad Ra_n = \frac{1}{(1 - \chi)^3(1 + \chi)}Ra, \qquad (4.1)$$

with the subscript n denoting the new parameters. Individual calculations are performed using the same procedure as outlined in the introduction to Chapter 3, with χ being varied for $m = 2$. We have chosen to fix $Ra_n = 101$, $E_n = 4.44 \times 10^{-4}$ and $q = 10$ for these calculations. These values of Ra_n and E_n are equivalent to $Ra = 40$ and $E = 10^{-3}$. For our definitions of Ra_n and E_n (based on r_o), this means that the temperature gradient, β, remains fixed as χ is varied. Note that Ra and E which are based on the gap width, $L = r_o - r_i$, vary as χ is varied. If $\beta, \nu, \mathbf{g}$ and Ω remain fixed, then using L as the length scale leads to a confusing picture. The full range of calculations performed is displayed in Table 4.1. From the table it can be seen that

63

solutions were obtained for values of χ ranging from 0.025, where the magnetic field and convection are almost periodic, to 0.50, where the magnetic field decays to zero (for our fixed value of Ra_n), but the convection remains steady once the magnetic field is sufficiently weak. These results are true for our fixed value of Ra_n. Varying the value of Ra_n at different inner core radii leads to behaviour similar to that observed for $\chi = 0.33$, as we shall discuss later.

4.3 Results and discussion

The behaviour of the magnetic field and convection as χ is varied can be observed in Figure 4.1. The strength of both the magnetic field and the convection clearly increase as the inner core radius increases, reaching a maximum at $\chi \approx 0.25$. The magnetic field strength decreases as χ is increased further, decaying to zero at $\chi = 0.45$ and 0.50.

To gain further insight into the variation in magnetic field strength with inner core radius, the values of Ra_c, the critical value of Ra_n for the onset of convection (with $\mathbf{B} = \mathbf{0}$), are obtained using the code, and plotted in Figure 4.1. We have prescribed $m = 2$, in order to be consistent with our dynamo calculations, and find that Ra_c is independent of χ, until $\chi \approx 0.3$, but then increases with increasing χ. Recent calculations with a similar value of E to ours, have found that this pattern of behaviour emerges from a thermal convection calculation with both fixed m and full $3D$ resolution, (E. Dormy, personal communication), and a similar effect has also been observed by (Zhang 1992). These results suggest that our dynamo is most efficient at intermediate inner core radii.

4.3.1 Solutions at small inner core radii

For small values of the inner core radius ($\chi = 0.025, 0.05$), the time dependence of the axisymmetric magnetic field is almost periodic and the structure is independent of χ. The regularity of these solutions came as a surprise. Given the earlier work on the
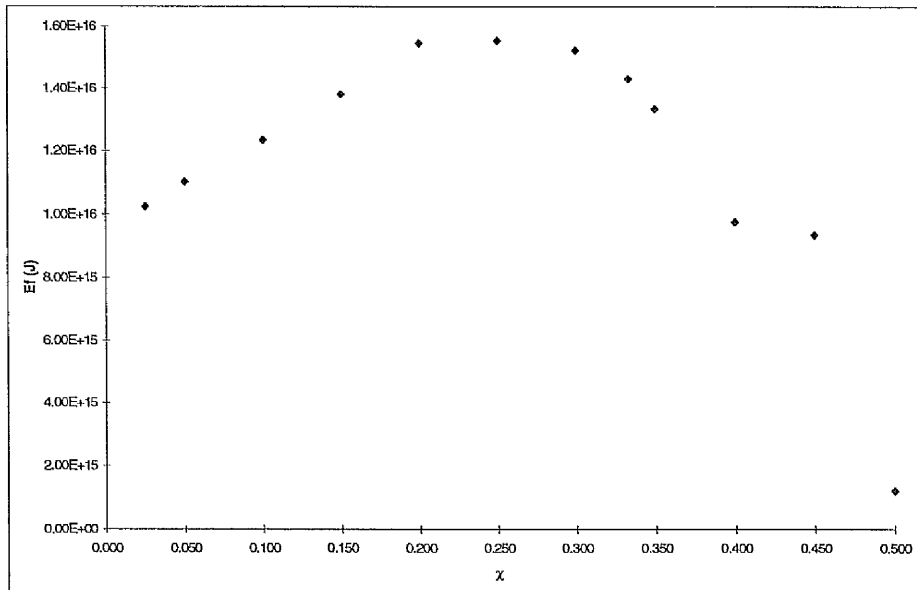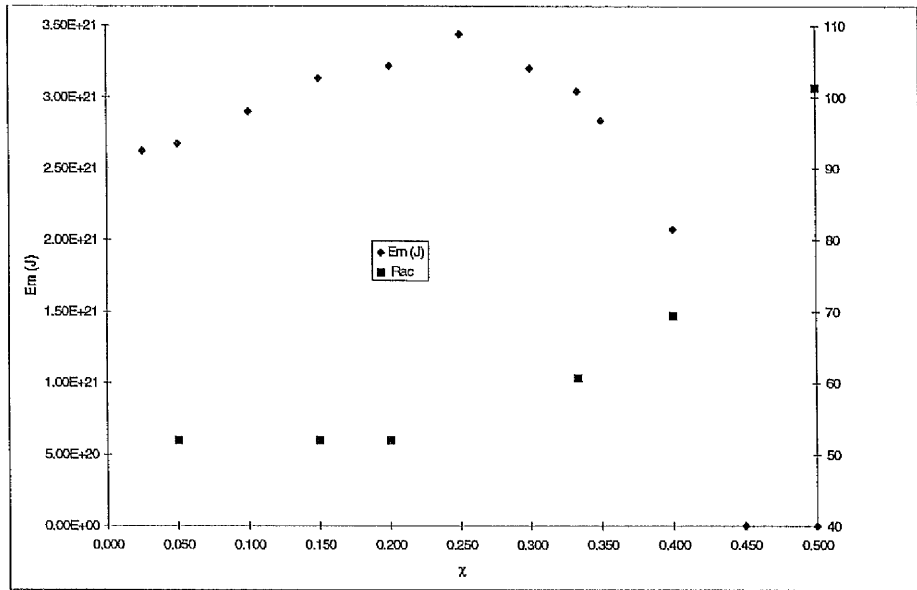
Figure 4.1: A plot of the time-averaged magnetic energy and Ra_c, and fluid energy, against χ.

stabilising effect of a finitely conducting inner core, we had expected that decreasing the inner core radius would produce more chaotic solutions. The periodicity is probably due to the simplification of the geometry since we are effectively working in a sphere rather than a spherical shell. At these smaller values of χ, competition between regions inside and outside the tangent cylinder is not so intense, leading to less complex time dependent behaviour. This is emphasised by studying Figure 4.2, which shows the time dependence of the axisymmetric magnetic field at four different values of Ra_n, for $\chi = 0.05$. The total survey was performed for values ranging from $Ra_n = 50$, where there is no magnetic field or convection, to $Ra_n = 111$, where the strong magnetic field collapses to zero and the convection becomes steady. The strength of the solution follows a similar trend with increasing Ra_n to that observed in Figure 3.1 for $\chi = 0.33$. The results of this study for small inner core radius strongly suggest that the underlying dynamo process is independent of inner core radius, although the critical values of the driving are different. Solutions with a simple time dependence seem to be preferred at small inner core radius, and the magnetic field is steady when first generated at $Ra_n \approx 72$. If Ra_n is increased further, the time dependence of the magnetic field becomes increasingly complicated, until the strong magnetic field suddenly collapses, in a similar fashion to the solution for $\chi = 0.33$. Examination of the axisymmetric magnetic field structures which are shown in Figure 4.3, emphasises the similarity of the solutions at small inner core radii. The dynamo process is consistently located outside of the tangent cylinder, in contrast to the solutions at larger inner core radii, which have magnetic field generation taking place inside the tangent cylinder (Figures 4.6, 4.7). However, this change in structure is merely due to the effect of geometry simplification, and not a change in the character of the dynamo, as we have already seen that the underlying dynamo process seems to be independent of χ.

The well-behaved, regular solutions also provide an opportunity to examine the influence of E. Figure 4.4, also shows the time dependence of the solutions for $\chi =$
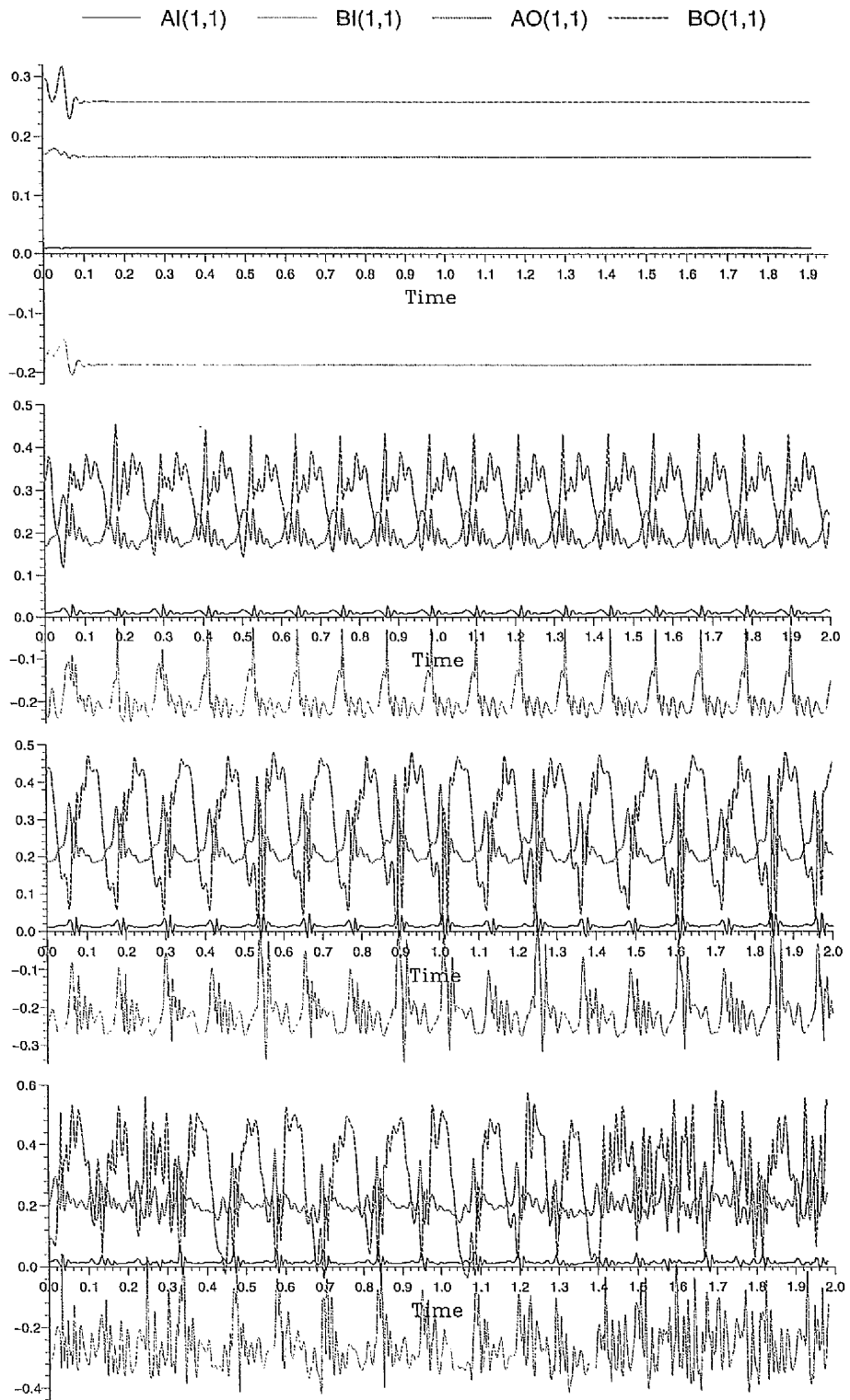
Figure 4.2: The time dependence of the axisymmetric magnetic field for, $Ra_n = 72$, 83, 94, and 106, with $\chi = 0.05$ and $m = 2$.

67
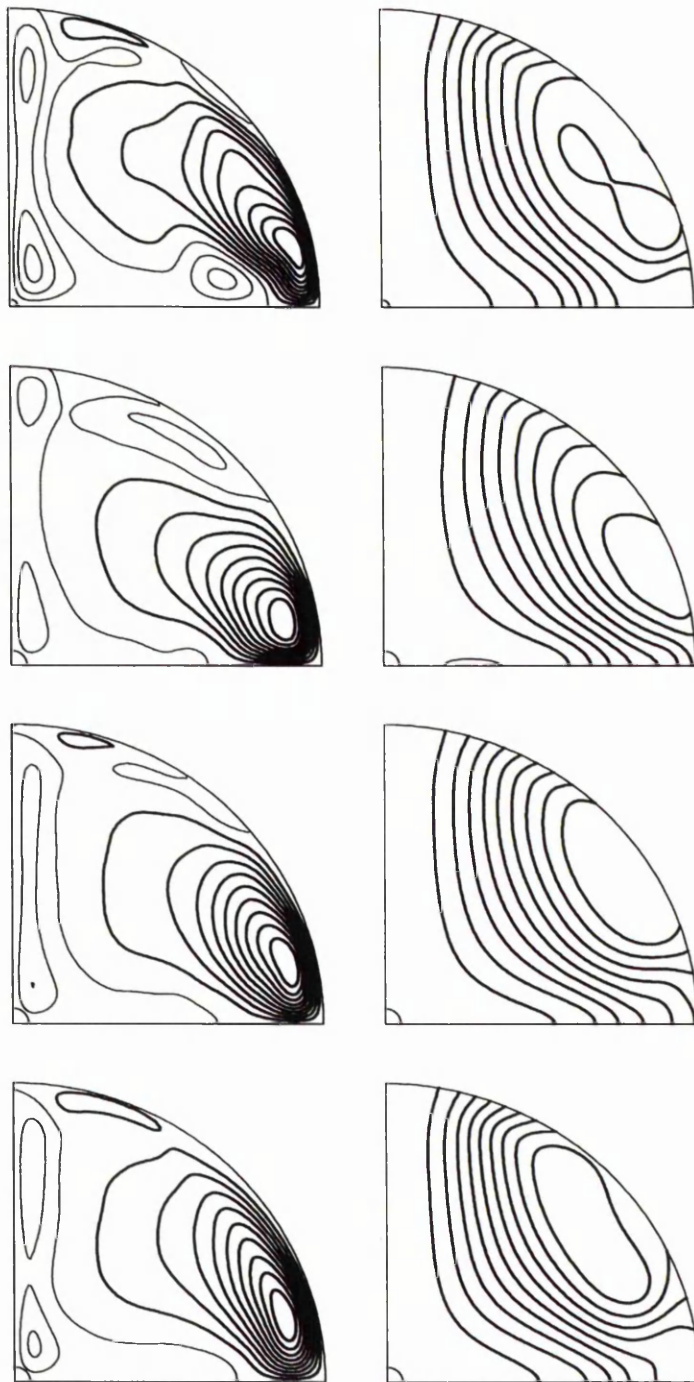
Figure 4.3: A snapshot of the axisymmetric toroidal magnetic field contours and poloidal magnetic field lines for $\chi = 0.025$, 0.05, 0.05-$Ra_n = 89$ and 0.05-$Ra_n = 89 - E = 9 \times 10^{-4}$ with $m = 2$.
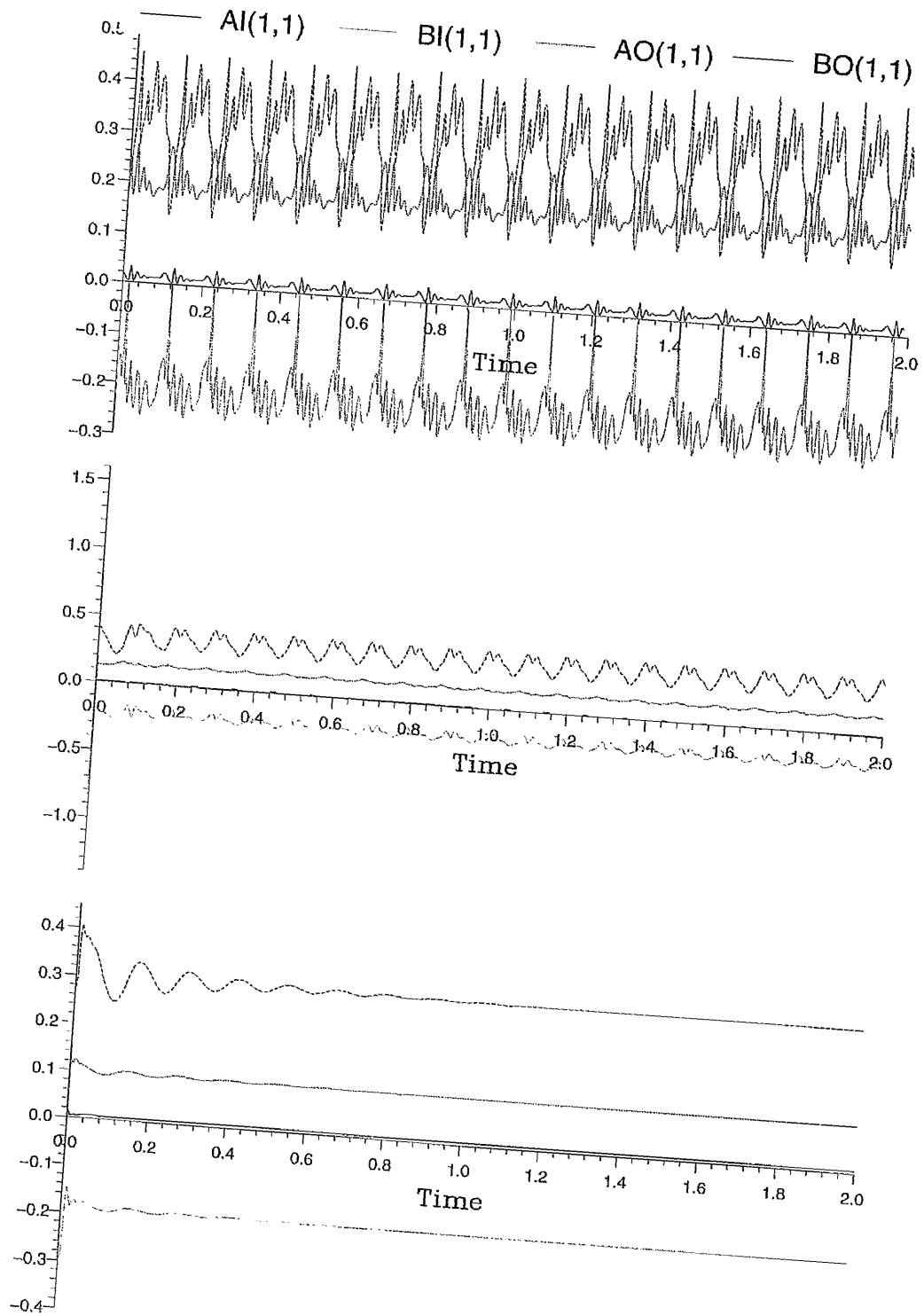
Figure 4.4: The time dependence of the axisymmetric magnetic field for $E_n = 4.4 \times 10^{-4}, 6.8 \times 10^{-4}$, and 9×10^{-4}, with $Ra_n = 89$ and $m = 2$.

69

0.05, $Ra_n = 127$ with different values of E_n. We found that the value of E_n could not be significantly decreased from 4.44×10^{-4} without greatly increasing the truncation and decreasing the time step, but that as it increased the solution became much more regular, until at $E_n \approx 9 \times 10^{-4}$ the solution is steady. Despite the change in time dependence, there is no significant change in the axisymmetric structure as can be seen by comparing the last two plots in Figure 4.3. So, at small χ, a modest change in E_n has resulted in a markedly different time dependence.

4.3.2 Solutions at larger inner core radii

The time dependence of the magnetic field for intermediate and large values of χ is shown in Figure 4.5. At $\chi = 0.10$, the axisymmetric magnetic field begins to show more quasi-periodic behaviour, and as χ is increased further the time dependence becomes increasingly chaotic and remains chaotic for intermediate inner core sizes (i.e. $0.10 \lesssim \chi \lesssim 0.33$. At $\chi = 0.35$ the solution has become more regular, and once $\chi = 0.40$ the time dependence of the solution has returned to a more regular periodic form, as predicted by the stabilising effect. As the inner core size is increased further to $\chi = 0.45$ and $\chi = 0.50$, then the dynamo switches off, although convection is still taking place. The corresponding axisymmetric magnetic field and flow structures are given in Figures 4.6 and 4.7. Again, allowing for the fact that we are viewing a snapshot of a time-varying solution the structures exhibit qualitatively similar features, but now there is some magnetic field generation taking place inside the tangent cylinder. This was not a feature of the solutions obtained by Hollerbach and Jones, but still an increasingly large inner core stabilises the magnetic field. This would suggest that the stabilising effect is not limited to solutions of the type obtained by Hollerbach and Jones.
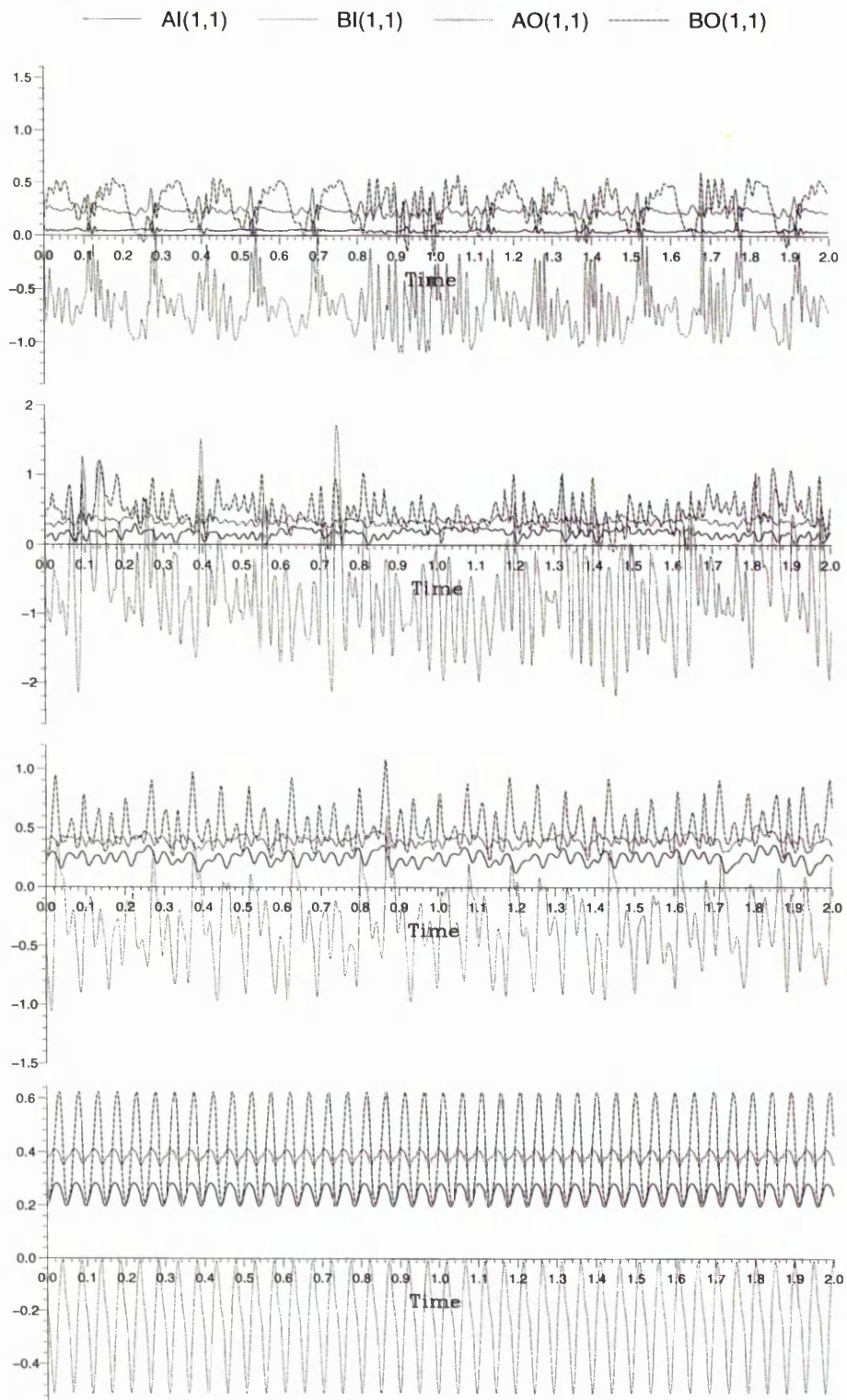
Figure 4.5: The time dependence of the axisymmetric magnetic field for $\chi = 0.10$, 0.25, 0.35 and 0.40 with $m = 2$.
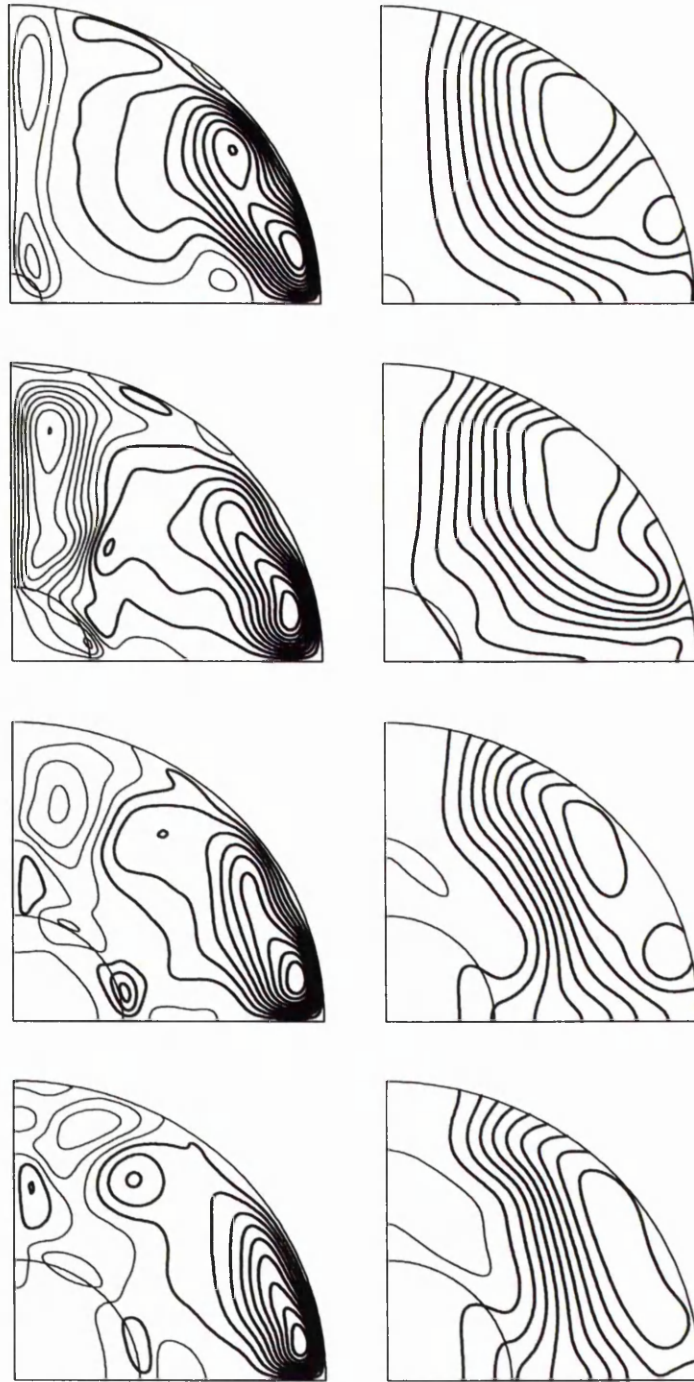
Figure 4.6: A snapshot of the axisymmetric toroidal magnetic field contours and poloidal magnetic field lines for $\chi = 0.10$, 0.25, 0.35 and 0.40 with $m = 2$.
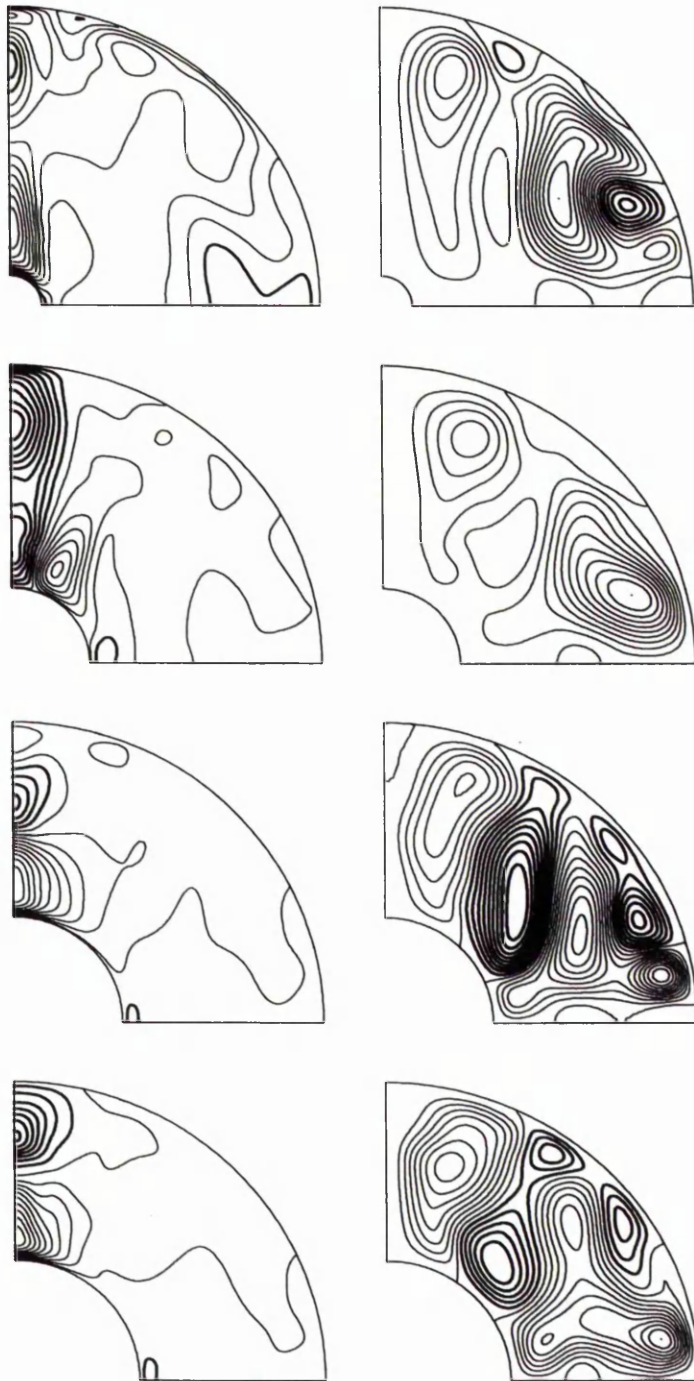
Figure 4.7: A snapshot of the axisymmetric angular velocity contours (left) and meridional streamlines (right) for $\chi = 0.10$, 0.25, 0.35 and 0.40 with $m = 2$.

4.3.3 Sensitivity to initial conditions

For certain inner core radii, the numerical solution obtained is also highly dependent on the initial conditions used. We have observed that, for a given set of parameter values, the magnetic field can sometimes collapse, leaving only steady convection. This is demonstrated in Figure 4.8, which shows some solutions at $\chi = 0.15$. In the first plot a strong, chaotic axisymmetric magnetic field can clearly be seen to be maintained for just over two diffusion times. Yet, suddenly the dynamo switches off, leaving only a steady convective solution. This phenomenon has been observed before for chaotically varying solutions. If the magnetic field becomes too weak for the Lorentz force to balance the Coriolis force, then the flow may revert to a weak-field configuration, from which it is very difficult to recover a strong-field solution (Sarson et al. 1999). The second set of initial conditions is obtained by running with the original initial conditions at a lower value of Ra, as shown in the second plot. Running at a larger value of Ra, produced a very rapid field collapse, as can be seen in the third plot. This is emphasised by comparison of the run time, which in this case is two, as opposed to four, time scales. The axisymmetric field produced by running at the original parameter values, with a snapshot of the solution in the second plot as initial conditions, is shown in the final plot. Clearly, a strong, chaotic magnetic field is now being maintained.
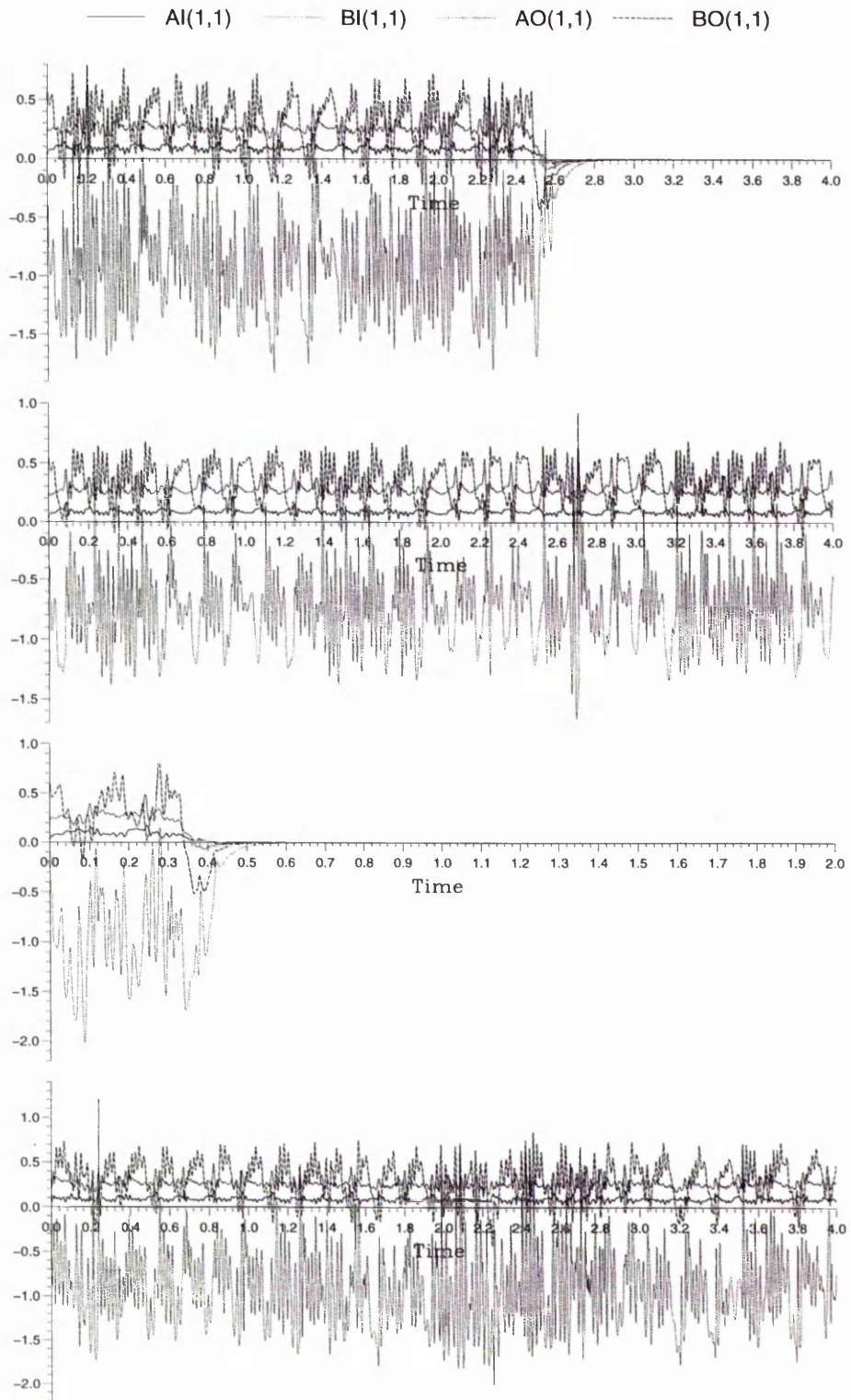
Figure 4.8: Time dependence of the axisymmetric magnetic field for $Ra_n = 177, 165, 190$ and 177 at $\chi = 0.15$ with $m = 2$.

Chapter 5

The introduction of the inertial term

5.1 Introduction

The parameters controlling the size of both the inertial term (Ro) and the viscous term (E), in the momentum equation assume very small geophysical values. We have already discussed the difficulties involved in obtaining solutions either with geophysical values of E, or with $E = 0$. The best that can be achieved is to prescribe a finite value and hope that it at least lies in the correct asymptotic regime. There is no such constraint on the choice of the Rossby number, although smaller values of Ro may be excluded by the numerical scheme employed. Setting $Ro = 0$ filters out rapid fluctuations associated with the rotational time scale, making solutions easier to obtain. To make progress, this is the approach which has been adopted until now with the $2\frac{1}{2}D$ model. Different numerical methods are required to solve the momentum equation with and without inertia present (see Appendices A and B). If the inertial term is to be included, then the fact that E is larger than it should be will also affect the choice of Ro. In the core, the viscous time scale can be as short as $O(E^{1/2})$, while the rotational time scale is $O(Ro)$, making the rotational time scale the shorter of the two even with the most pessimistically small value of E. The choice for Ro now rests on the assumption which is made for the relative size of these time scales. Retaining a value of Ro as close as

possible to geophysical, while having an unrealistically high Ekman number makes the rotational time scale unrealistically shorter than the viscous time scale, so that any motions acting on this time scale will be strongly damped e.g. torsional oscillations (see later). On the other hand, prescribing a value which is more commensurate with E, keeps these time scales closer to the correct proportion for the Earth's core, and so allows motions on the inertial time scale, although the value of Ro is now unrealistically high.

The $3D$ Kuang-Bloxham and Glatzmaier-Roberts dynamos produce magnetic fields which look very similar at the surface, but inside the core both the magnetic field and the flow morphology look very different. For the Glatzmaier-Roberts type solution, there are very strong azimuthal flows inside the tangent cylinder, with most of the axisymmetric flow concentrated near the rotation axis. The toroidal magnetic field is concentrated near the ICB, and the poloidal magnetic field fills the outer core, with strong closed loops near the ICB, but there is very little poloidal or toroidal magnetic field in the inner core. The strong axisymmetric magnetic fields and flows cause an eastwards super-rotation of the inner core. The Kuang-Bloxham type solution on the other hand has flow distributed throughout the outer core, and much simpler toroidal and poloidal field structure spread throughout the outer and inner cores. The inner core also super-rotates at about the same rate in this model, but in no fixed direction. Different assumptions are used to treat the viscous and inertial terms, but there is still some debate as to exactly what effects are responsible for the observed differences.

Glatzmaier and Roberts prescribe $E = 2 \times 10^{-6}$ and adopt no-slip boundary conditions for the flow. Kuang and Bloxham prescribe $E = 2 \times 10^{-5}$, and adopt stress-free boundary conditions for the flow, although both boundaries are rigid in the Earth. The advantage of adopting stress-free boundaries is that viscous effects are now only of $O(E)$ as opposed to $O(E^{1/2})$, and given that the value of E adopted is too large, then this will reduce the effect of viscosity in the model to a more realistic level. Kuang

and Bloxham claim that it is this assumption which results in the observed differences between the two models (Kuang and Bloxham 1997). They repeated their calculations at the same parameter values, but used no-slip boundary conditions for the flow. The solution obtained looked much more like that of Glatzmaier and Roberts, with the inner core rotating in a fixed (eastwards) direction. This suggests that the observed differences are not due to different parameter values, but due to the effect of viscous coupling on the flow at the boundaries. Further investigation indicated that the models were operating in different dynamical regimes, due to the different force balance in the momentum equation, with the solution with stress-free boundaries being closer to a Taylor state (see Chapter 2). However Glatzmaier and Roberts claim that the differences can be explained by the different prescribed values of Ro. They have adopted a value of Ro as close as possible to geophysical, setting $Ro = 10^{-9}$, whereas Kuang and Bloxham prescribe $Ro\, (= E) = 2 \times 10^{-5}$. In addition, both groups treat the inertial term in different ways. The non-axisymmetric inertial terms are ignored in both models, but different parts of the axisymmetric inertial term are retained. The Glatzmaier-Roberts solutions have very little magnetic field in the inner core, but strong toroidal and poloidal magnetic fields at the ICB, while both Kuang-Bloxham solutions have considerable magnetic fields in the inner core, particularly in the stress-free case. It may be that in the Glatzmaier-Roberts dynamo, the magnetic field doesn't have enough time to diffuse into the inner core, because the lower the value of Ro the faster the inner core can accelerate. The previously mentioned $3D$ models which are run in similar parameter regimes to ours all include the full inertial term, and usually prescribe Ro of $O(10^{-4}) - O(10^{-5})$, with E of $O(10^{-3}) - O(10^{-4})$.

Zhang has performed a very thorough investigation of the onset of thermal convection in a rapidly rotating spherical shell, using a model which includes inertia. He found different preferred modes depending on the value of the Prandtl number, $Pr = \nu/\kappa$. For $Pr \gtrsim O(1)$ columnar convection rolls of the type predicted by Busse

78

(1970) are preferred. With a slightly smaller value, a spiralling columnar convection mode is preferred (Zhang 1992), and with smaller values still, equatorially trapped Poincaré modes are preferred (Zhang 1994). For the typical values of Pr which we will be considering then columnar convection rolls aligned with the rotation axis would be expected, and in any case it is not clear if any of these modes of convection operate in a magnetic system. In addition Kuang and Bloxham find that including inertia does not affect the onset of convection or the slightly super-critical flow, in the absence of a magnetic field (Kuang and Bloxham 1999). Very little work on the effect of inertia in the dynamo problem has been carried out to date, as most models initially excluded inertial effects. Jault (1995), using an $\alpha\omega$-dynamo model, has found that restoring just the axisymmetric inertial term ($Ro\partial\omega_G/\partial t$, the geostrophic shear), can help to prevent the physical and numerical instabilities associated with small viscosity. This makes possible the investigation of solutions at these small viscosities, and allows the evolution of a steady solution to a Taylor state.

Changes in the Earth's rotation rate occur on many different time scales, but variations in the length of the day with period of about a decade give good agreement with the changes in core angular momentum inferred from core flow models (see for example Bloxham 1998). This suggests that the crucial factor in explaining these observations is the exchange of angular momentum between the core and the mantle. Waves occurring on decadal time scales in the core are likely to be in the form of torsional oscillations. These z-independent oscillations arise when Taylor's condition is not satisfied and an inertial torque balances the non-vanishing Lorentz torque on the co-axial cylinders. Each cylindrical annulus rotates as a rigid body, linked to the neighbouring annuli by the radial magnetic field. Damping of these oscillations enables the system to evolve to a Taylor state. Since the mantle is to a good approximation an insulator, then changes in the magnetic field at the Earth's surface can give some indication of the changes at the CMB, which can in turn be used to infer the flow at the CMB. Identifying the

79

variations in the magnetic field at the CMB due to torsional oscillations can give an insight as to how the magnetic field is changing deeper in the core, since the resulting motion is independent of z.

5.2 Calculations

We use Model 2 which includes the inertial term, requiring a different method of solution, as described in Appendix B. The model which we have chosen to use also has no imposed symmetry and some of the solutions presented in Chapter 3 will be used as starting points. Much of the work will again centre on the Run B solution, which has parameter values $\chi = 0.33, E = 1 \times 10^{-3}, q = 10, Ra = 50, \Sigma = 1$ and $m = 2$. The spectral coefficients describing $\mathbf{B}, \mathbf{U}$ and T for this solution are transformed to the new coefficients as described in Appendix B, and the initial value of Ro is chosen to be 1×10^{-4}. This choice represents a compromise, as the value of Ro has to be low enough so as not to be too different from the initial conditions, and high enough to allow a sensible time step for the calculation to be employed. Solutions have subsequently been obtained at lower and higher values of Ro, with the full range investigated given in Table 5.1. The choice of time step was influenced by the value of Ro and the fact that the quadrupole component grew very quickly when the symmetry constraint was removed, giving a solution with mixed symmetry. As discussed in Chapter 2, the mixed symmetry solutions tend to have rather irregular time dependence, and so lower time steps may have to be adopted. The prescribed value of the time step is continually checked, and the truncation was chosen to be consistent with previous work, but different levels were adopted for $\mathbf{B}, \mathbf{U}$ and T, with $KB = 24, LB = 36, KU = 36, LU = 48, KT = 18, LT = 36$, (see Appendix B). To obtain an idea of the effect of varying Ra at a given Rossby number, we also performed a short survey for $Ro = 5 \times 10^{-4}$. A solution for $Ro = 1 \times 10^{-4}, Ra = 60$ has also been obtained with $m = 4$, to establish whether any of the effects which we see are peculiar to a given value of m. Our initial condition in this

80

case was chosen to be the solution obtained in Chapter 3 at $Ra = 60$, with the same values of E and q. This is also a strong-field dynamo, but with a lower characteristic magnetic energy.

Presentation of results will be significantly different to that in Chapters 3 and 4, being given mostly in terms of the real dimensional quantities. This allows a clearer comparison with the previously obtained solutions, which use a different set of expansions. The axisymmetric structures are plotted using the same method as employed in Chapters 3 and 4, although clearly the solution in the full meridional plane now needs to be included. Additionally we can calculate the magnitudes of some of the forces and torques in the momentum equation at individual points, to give some idea of the balance in the momentum equation. The Coriolis, Lorentz, viscous and buoyancy forces are all evaluated, along with the $Ro\partial U/\partial t$ part of the inertial force, at two different points, one inside the tangent cylinder and one outside, at about the mid radius of the outer core (see Appendix B). This should ensure that the points chosen are as 'typical' as possible. The components of the torque about the z-axis, can then be easily calculated. In particular, we wish to establish some idea of the size of the inertial term relative to the other forces as Ro is varied. Since we do not calculate the pressure, it is difficult to check on the actual force balance in the momentum equation. However, by considering the z-components of the torque (about the z-axis), due to the axisymmetric forces at the same points, a clearer picture of the balance can be obtained. The buoyancy and pressure gradient do not contribute, and the $(\mathbf{U} \cdot \nabla)\mathbf{U}$ part of the inertial term can now be more easily calculated (see Appendix B).

81

Table 5.1: Calculations performed varying Ro at $Ra = 50$ with all other parameters fixed and $m = 2$.

Ro	Comments	$Em(J)$	$Ek(J)$	Run Time
0	Chaotic magnetic field	1.62×10^{20}	1.02×10^{16}	10.00
5.0×10^{-5}	Weak periodic magnetic field	2.27×10^{20}	3.68×10^{16}	1.25
7.5×10^{-5}	Weak periodic magnetic field	3.40×10^{20}	3.54×10^{16}	3.30
8.75×10^{-5}	Weak periodic magnetic field	7.85×10^{20}	3.31×10^{16}	1.50
1.0×10^{-4}	Weak periodic magnetic field	4.74×10^{20}	3.40×10^{16}	2.00
1.0×10^{-4}	Chaotic magnetic field	1.80×10^{21}	2.83×10^{16}	4.00
2.0×10^{-4}	Chaotic magnetic field	1.76×10^{21}	2.68×10^{16}	3.50
5.0×10^{-4}	Weaker chaotic magnetic field	8.60×10^{21}	2.95×10^{16}	3.20
6.25×10^{-4}	Magnetic field decays slowly	0	4.11×10^{16}	0.50
7.5×10^{-4}	Magnetic field decays slowly	0	4.12×10^{16}	2.00

Table 5.2: Calculations performed varying Ra at with all other parameters fixed and $m = 2$.

Ra	Comments	$Em(J)$	$Ek(J)$	Run Time	Ro
55	Chaotic magnetic field	2.82×10^{21}	3.09×10^{16}	1.50	1×10^{-4}
45	Chaotic magnetic field	8.07×10^{20}	2.31×10^{16}	2.50	5×10^{-4}
55	Strong, stable magnetic field	3.63×10^{21}	1.94×10^{16}	3.00	5×10^{-4}
60	Strong, stable magnetic field	3.94×10^{21}	2.25×10^{16}	2.00	5×10^{-4}

5.3 Results and discussion

Our numerical models give a solution with $Ro = 0$ and dipolar symmetry imposed, and solutions with $Ro \neq 0$ and no imposed symmetry. It is also of interest to obtain a solution with $Ro = 0$ and no imposed symmetry. Such a solution was obtained by (Graeme Sarson, personal communication), and it is this result that is displayed in Table 5.1. The time-averaged magnetic and kinetic energies, calculated as before, are plotted against Ro in Figure 5.1. It is immediately obvious that there are two possible solutions at $Ro = 1 \times 10^{-4}$ which have been labelled chaotic and periodic, based on the time dependence displayed by the solution. Although the magnitude of the Lorentz force is smaller than that of the chaotic solutions, the periodic solutions still have a magnetic energy about four orders of magnetic greater than the kinetic energy, and so

82
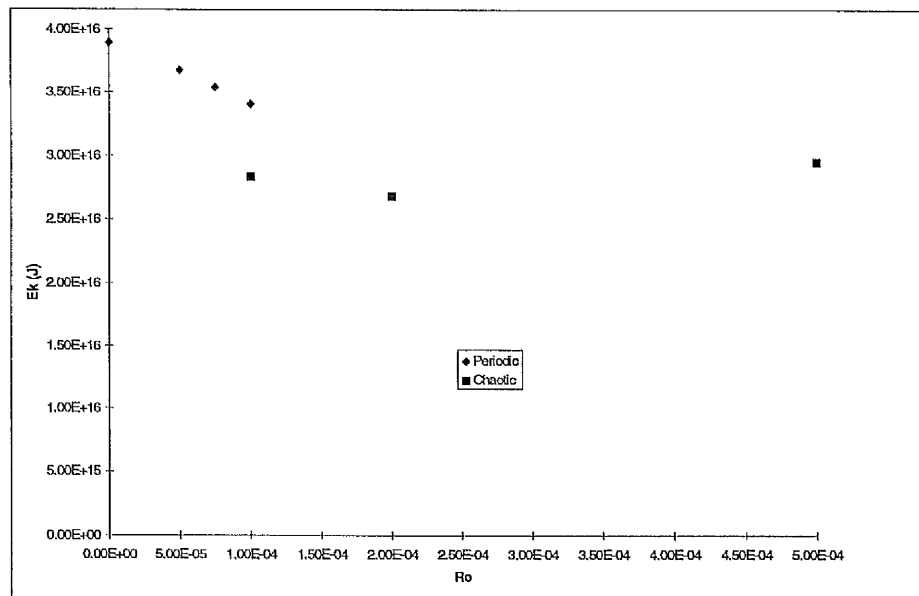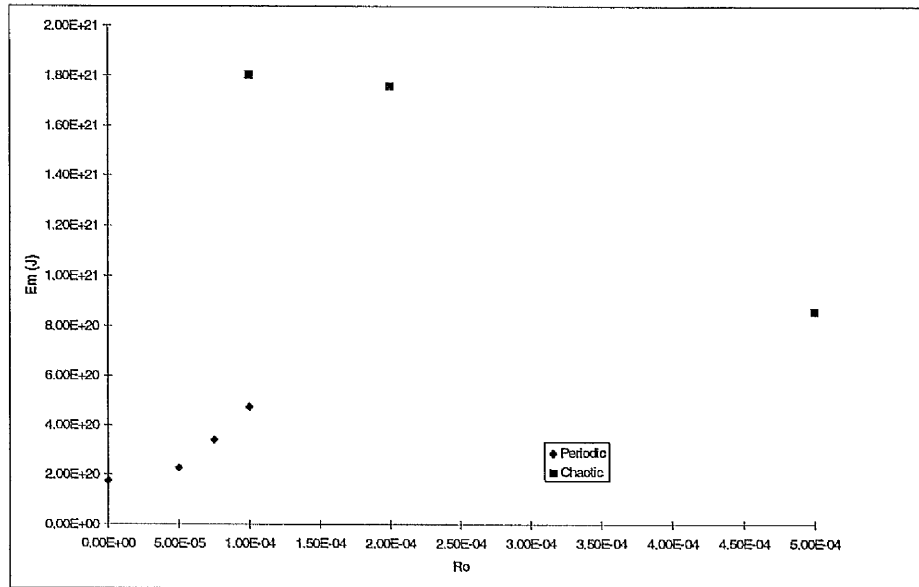
Figure 5.1: A plot of the time-averaged magnetic energy and fluid energy, against Ro.

cannot really be described as weak field in the familiar sense. Periodic solutions are obtained in the range $5 \times 10^{-5} \lesssim Ro \leq 1 \times 10^{-4}$, with chaotic solutions only seemingly obtained in the range $1 \times 10^{-4} \lesssim Ro \lesssim 5 \times 10^{-4}$. Even for $Ro = 1.25 \times 10^{-4}$ a chaotic solution was obtained, and so 1×10^{-4} seems to be the only value of Ro for which different solutions are possible.

5.3.1   Chaotic solutions

For the initial solution obtained with $Ro = 1 \times 10^{-4}$, a quadrupole component of about equal magnitude to the initial dipole component is very quickly generated. Once the solution is of mixed symmetry type we find that the time dependence is somewhat chaotic, with frequent, irregularly occurring reversals of the magnetic field. The flow can also experience large variations, particularly the axisymmetric zonal component. All of these observations are somewhat consistent with the effects of including mixed symmetry to solutions previously obtained without inertia. After obtaining this initial (chaotic) solution at $Ro = 1 \times 10^{-4}$, the value of Ro is varied. By increasing Ro qualitatively similar solutions were obtained at $Ro = 2 \times 10^{-4}$ and 5×10^{-4}, although the solution at $Ro = 5 \times 10^{-4}$ had significantly weaker magnetic energy, and much less rapid variation in the flow. This suggests that by restoring inertia the flow cannot respond as quickly to any changes in the core conditions, as one might expect. Figure 5.2 displays the axisymmetric and non-axisymmetric magnetic energy, as a function of time for the mixed symmetry solution obtained with $Ro = 0$ and two other non-zero values of Ro. In this chapter we will also consider the order of plots in the figures to be from top to bottom.

The most obvious qualitative difference between the solutions is that the non-axisymmetric magnetic energy is roughly equal to the axisymmetric magnetic energy for $Ro = 0$, but it has become about a factor 2 larger for $Ro = 1 \times 10^{-4}$ and 5×10^{-4}. Comparison of the amplitude of the magnetic energy shows that the solution

at $Ro = 1 \times 10^{-4}$ is about an order of magnitude larger, than the solution without inertia, and the weaker solution at $Ro = 5 \times 10^{-4}$ is also about seven times larger. Consideration of a longer time series, for the first plot in Figure 5.2, suggests that the magnetic energy seems to be repeatedly growing and decaying. By restoring inertia we seem to have allowed enough time for the magnetic field to increase in strength, without a rapid variation in the flow returning it to a weaker state. However by increasing the value of Ro, the inertial term begins to play a more significant role in the force balance, making it harder to generate a magnetic field.

Despite the differences in magnitude, the similarity of the axisymmetric structures obtained with and without inertia are quite striking. Figure 5.3 shows a snapshot of the solution for $Ro = 0$, where the quantities plotted as described in Chapters 3 and 4, and C is the codensity, which can be thought of as being equivalent to the temperature T (Sarson et al. 1997a). The magnetic field is essentially confined to one hemisphere, with most of the toroidal field being generated close to the CMB, and most of the poloidal field generated in the interior of the fluid. Both the flow and the temperature have remained highly symmetric about the equator, with a very well defined tangent cylinder appearing for the flow. Snapshots taken at different times throughout the run show broadly similar features. In Figure 5.4 a snapshot of the solution for $Ro = 2 \times 10^{-4}$ is shown for comparison. Again the magnetic field is confined to one hemisphere, although this is not always the case, with the toroidal field generated mostly at the CMB, and the poloidal field mostly in the interior of the fluid. The flow structure has also retained its symmetric character and adopts a similar form to the solution without inertia, with the greatest similarity in the fluid angular velocity. Interestingly this is also very similar to the fluid angular velocity obtained by Kuang and Bloxham when they employed no-slip boundary conditions for the flow (see Kuang and Bloxham 1997).

At this stage it is sensible to make some further comment on the magnitude of the

magnetic and kinetic energy. These have decreased somewhat from that obtained with the dipole symmetry and no inertia, however the magnetic energy is greater than that observed for the mixed symmetry solution without inertia. Closer examination reveals that, for the chaotic solutions ($1 \times 10^{-4} \lesssim Ro \lesssim 5 \times 10^{-4}$), the maximum value obtained by E_m is similar to the dipole value obtained without inertia, but the smaller average value can be accounted for by the fact that the magnetic field is continually reversing, and so will spend longer in a relatively weak state. Normally we have observed an increase in kinetic energy when the magnetic field becomes sufficiently weak, but in this case the kinetic energy has decreased, because with inertia retained it is harder to drive the fluid.

By increasing the value of Ro to 7.5×10^{-4} the magnetic field could no longer be maintained, although it decayed very slowly, as if the solution was just marginally critical. Despite this, we found that using a different set of initial conditions or increasing the value of Ra did not make field generation possible. Similar behaviour was obtained for $Ro = 6.25 \times 10^{-4}$. By considering the force balance in the momentum equation we find that the inertial term is playing an increasingly significant role in the force balance in the momentum equation, while the viscous force remains significant, with the Lorentz force generally becoming weaker to compensate. Under these conditions the convective motions will be very strongly damped, making dynamo action harder to achieve. Perhaps adopting the approach favoured by Kuang and Bloxham will aid the generation process here.

5.3.2 Periodic solutions

By decreasing the value of Ro to 7.5×10^{-5}, the solution behaves in a similar manner to that observed at $Ro = 1 \times 10^{-4}$ for about 1.5 diffusion times. However this is a transient feature and the chaotic solution is lost, with a weaker oscillatory magnetic field being obtained instead. These solutions persist for lower and higher values of
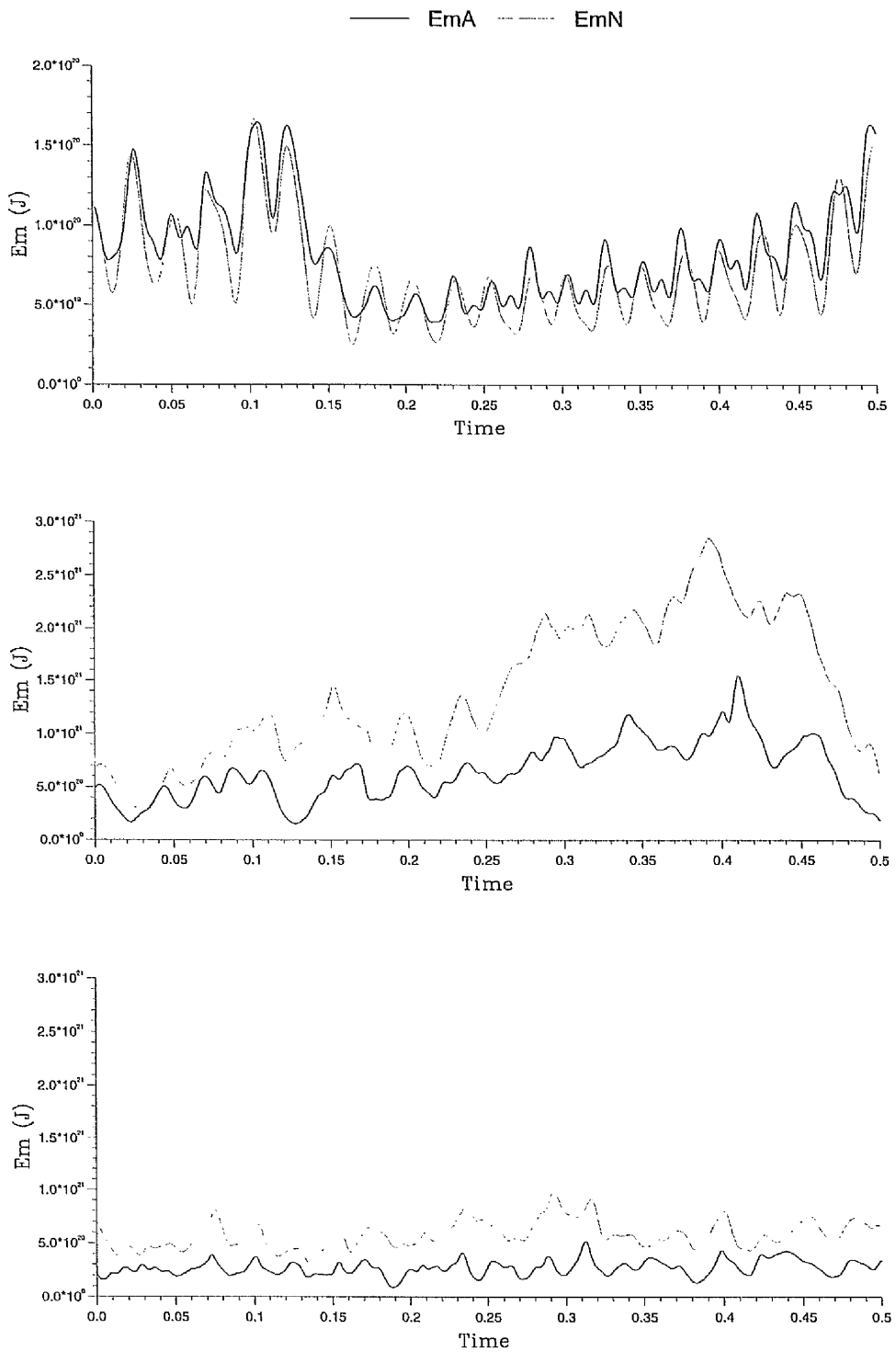
Figure 5.2: The time dependence of the axisymmetric magnetic energy for, $Ro = 0, 1 \times 10^{-4}$, and 5×10^{-4}, with $m = 2$.
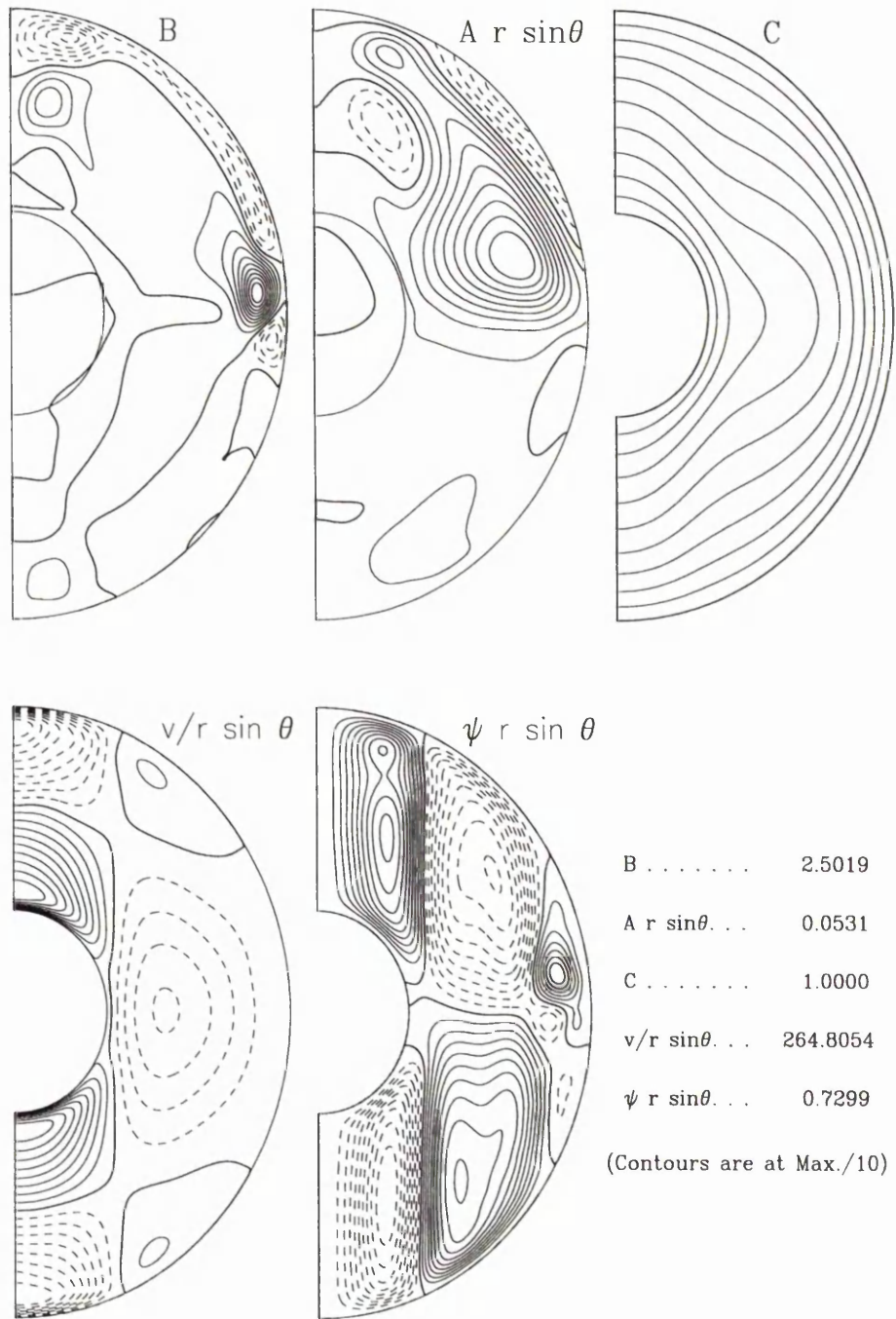
Figure 5.3: A snapshot of the axisymmetric quantities for $Ro = 0$, with $m = 2$.
(Obtained by Graeme Sarson)
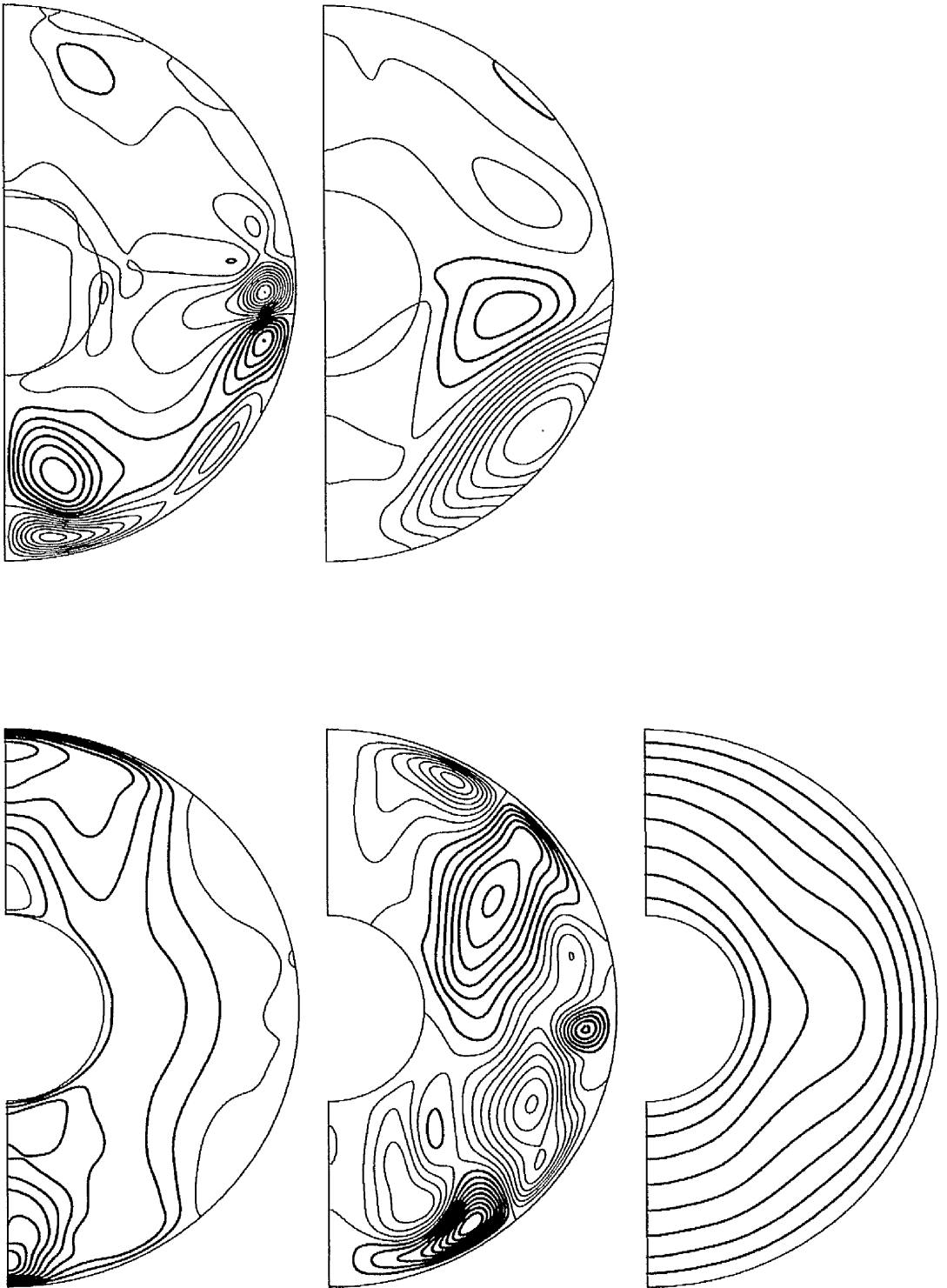
Figure 5.4: A snapshot of the axisymmetric quantities for $Ro = 2 \times 10^{-4}$, with $m = 2$.

Ro, and the time dependence of the magnetic energy for three representative values is displayed in Figure 5.5. The periodicity of these solutions is clearly evident, and in this case the solution strength increases in magnitude with increasing Ro. A snapshot of the axisymmetric structures for the solution at $Ro = 7.5 \times 10^{-5}$ is given in Figure 5.6, but the solutions at other values of Ro are similar. Clearly the magnetic field structure is dominated by the quadrupole component, but is still qualitatively similar to the mixed symmetry solution at $Ro = 0$. The flow structure is now highly symmetric, and even more reminiscent of the solution without inertia (c.f. Figure 5.3). In fact this type of solution is also very similar to the weak-field solution obtained at $Ra = 55$ with dipole symmetry imposed and $Ro = 0$ (see Figure 5.7). The lack of magnetic field around $Ra = 50$, on the weak field branch, may be due to the mixed symmetry solution becoming preferred in that region of parameter space. As we have already stated, by increasing the value of Ro from 1×10^{-4} to $Ro = 5 \times 10^{-4}$ the periodic solution returns to the chaotic state, as described in the above section. This suggests that there must be a very subtle balance between the chaotic and periodic solutions. As further evidence of this some snapshots of the chaotic solution at $Ro = 1 \times 10^{-4}$ look very similar to those of the periodic solutions.

5.3.3 Varying Ra

Our motivation in performing this study was partly to investigate varying Ra, and partly to obtain some different starting solutions to be used for higher values of Ro. Decreasing the value of Ra to 45 has little effect on the time dependence of the magnetic field produced, with a somewhat similar axisymmetric structure also retained, although the time averaged magnetic energy has decreased slightly, (see Table 5.2). Conversely, increasing the value of Ra to 55, has a significant effect on the nature of the magnetic field, changing if from chaotic and frequently reversing to a fixed polarity, with much larger time-averaged magnetic and kinetic energy (see Table 5.2), although this is still
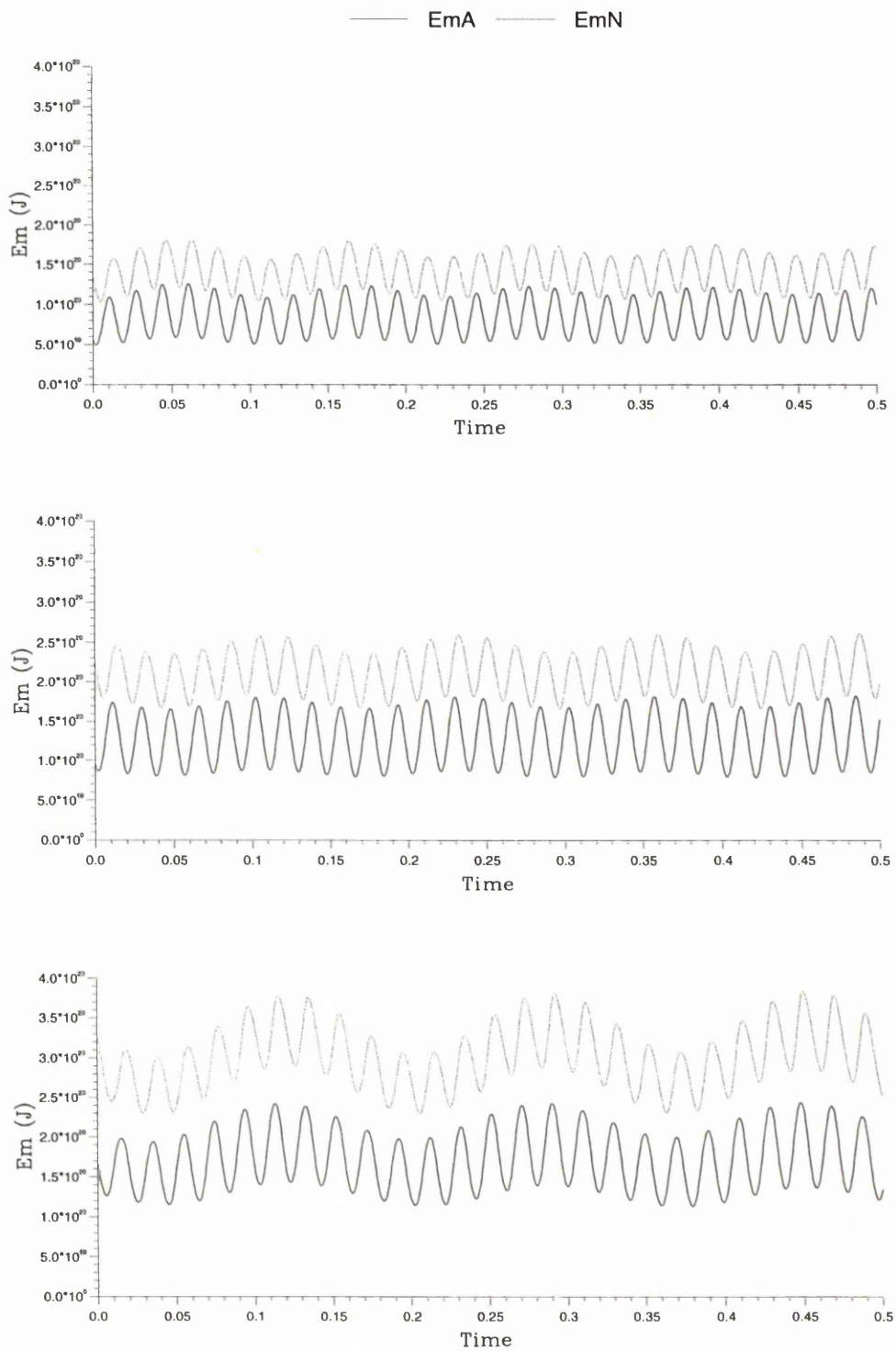
Figure 5.5: The time dependence of the axisymmetric and non-axisymmetric magnetic energy for, $Ro = 5 \times 10^{-5}, 7.5 \times 10^{-5}$, and 1×10^{-4}, with $m = 2$.

91
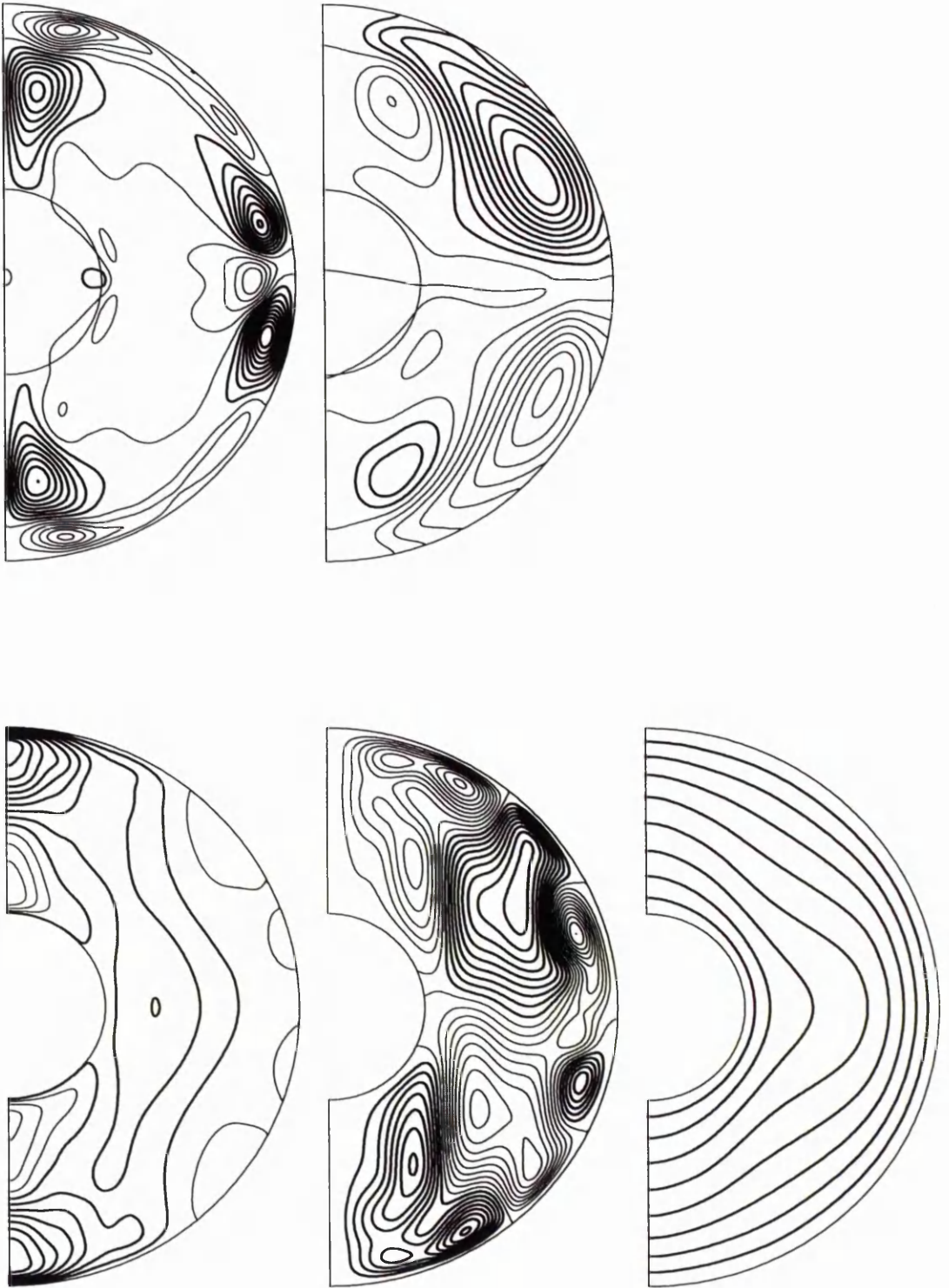
Figure 5.6: A snapshot of the axisymmetric quantities for $Ro = 7.5 \times 10^{-5}$, with $m = 2$.
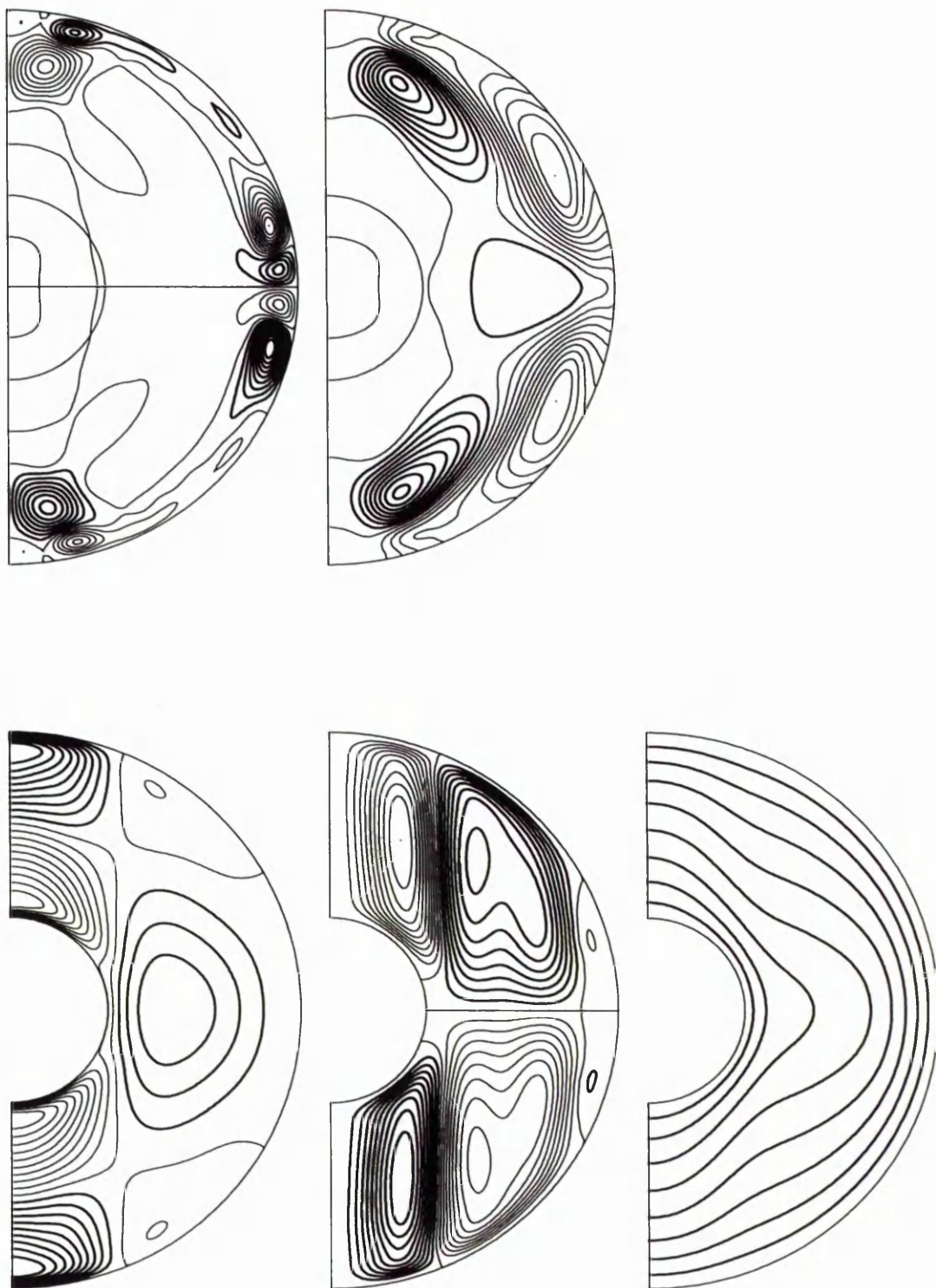
Figure 5.7: A snapshot of the axisymmetric quantities for the weak-field, dipole-imposed, solution with, $Ro = 0$, $Ra = 55$ and $m = 2$.

less than the stable, dipole solution without inertia. The reversing nature of the field is obtained by following the $k = 1, l = 1$ coefficient of the axisymmetric outer core poloidal field. Similar solution behaviour is observed at $Ra = 60$, with a corresponding increase in magnetic energy. This is not repeated at a lower value of Ro. By prescribing $Ro = 1 \times 10^{-4}$ and $Ra = 55$, the magnetic field retains its chaotic, reversing time dependent character.

For the stable magnetic fields, the structure of the axisymmetric magnetic field has now become much more dipole-dominated and there is now significant poloidal and toroidal magnetic field in the inner core (see Figure 5.8). This unexpected change in behaviour may be explained in the following way. An increase in Ra will produce an increase in the buoyancy force, which is uniformly distributed throughout the outer core. There will therefore be an increase in the buoyancy near the ICB, producing enhanced magnetic field generation, and so a stronger magnetic field. With a higher value of Ro, this strong magnetic field may persist at the ICB for a sufficient time to allow diffusion into the inner core. Once the strong magnetic field has diffused into the inner core, it will have a stabilising effect on the magnetic field, as described in Chapter 4. At the lower value of Ro the fluid is able to vary much more rapidly and so the magnetic field at the ICB may not be in a suitable configuration for long enough to allow diffusion into the inner core

5.3.4 Solution with $m = 4$

A run was also performed at $Ro = 1 \times 10^{-4}$ with $m = 4$, to look at the effect of introducing inertia in a different type of solution. Again a large quadrupole mode is very quickly generated, resulting in an increase in the magnitude of the non-axisymmetric magnetic energy, while the axisymmetric energy remains about the same. However, there is no discernible change in the strength of the convection. The time dependence of the magnetic field looks very similar to that of the chaotic solution at $Ro = 1 \times 10^{-4}$.

94
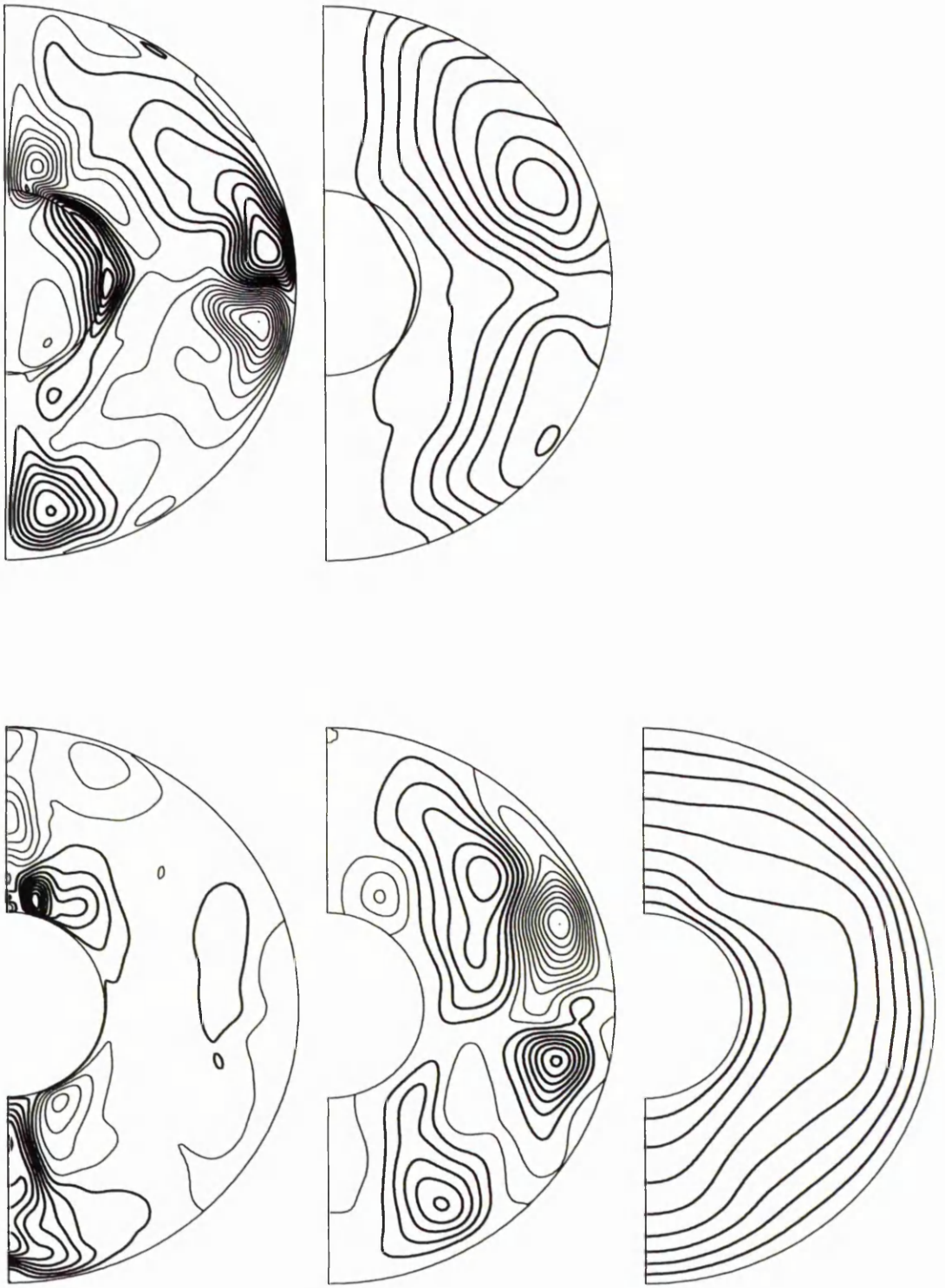
Figure 5.8: A snapshot of the axisymmetric quantities for $Ro = 5 \times 10^{-4}, Ra = 55$, with $m = 2$.

There is then a sudden change in the character of the solution, with the time dependence of the magnetic field, now much more like that of the periodic solutions. There is also similarity in the axisymmetric flow structure, but the magnetic field is more reminiscent of the solution obtained without inertia (see Figure 5.9). This behaviour is maintained for about half a diffusion time, when the solution returns to the chaotic state, reflected in the solution snapshot displayed in Figure 5.10. Although the solution is intermittently changing between chaotic and periodic states, it is qualitatively very similar in nature to the solution(s) we observe for $m = 2$. It is difficult to obtain a sensible measure of the strength of the magnetic field when the solution character is intermittently changing, but the magnitudes obtained in the different states are representative of those obtained with $m = 2$

5.3.5 Force balance in the momentum equation

As part of our calculation, the force terms on the right hand side of the momentum equation are obtained in real space. We want to exploit this information to gain further insight into our dynamo, and to establish the extent of the effect of the inertial (and other) terms. The method is discussed more fully in Appendix B, and there are some important considerations for interpretation of the results. Clearly the first drawback is that we are calculating the forces at single points, one inside and one outside the tangent cylinder. In addition it is difficult to see how the magnitudes of these forces evolve through time, and we do not of course obtain the full force balance since we do not calculate all of the forces. The non-axisymmetric terms are also problematical to deal with as the parts associated with $\cos(m\phi)$ and $\sin(m\phi)$ are treated separately, and so at any point the magnitude of the full non-axisymmetric force is in some sense the "sum" of these two components. It is clear that our method is by no means ideal, but is probably the most computationally efficient, and has given us a valuable insight into the relative importance of some of the forces in the momentum equation. This
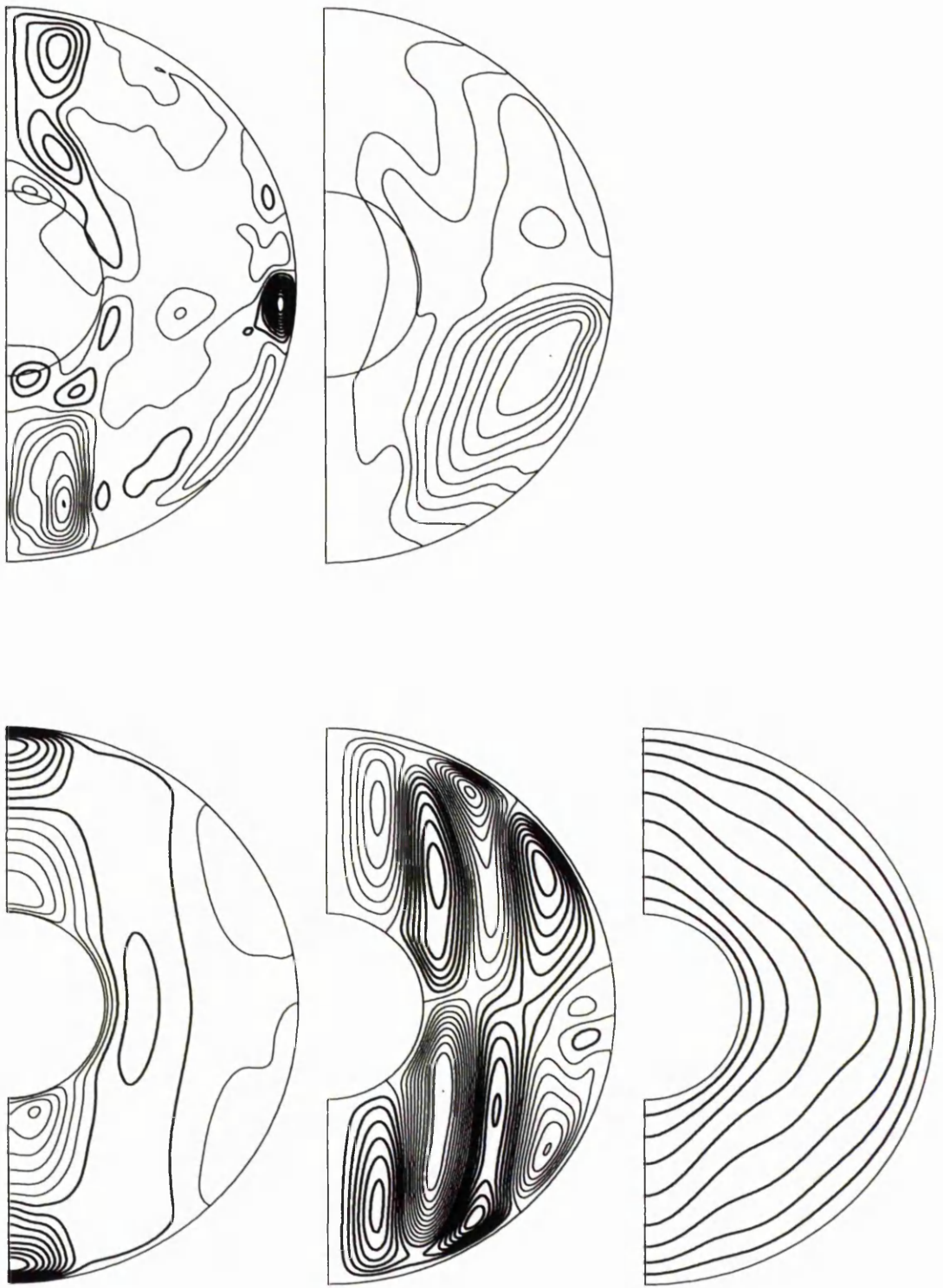
Figure 5.9: A snapshot of the axisymmetric quantities for $Ro = 1 \times 10^{-4}$, $Ra = 60$, at $\tau = 1$ with $m = 4$.
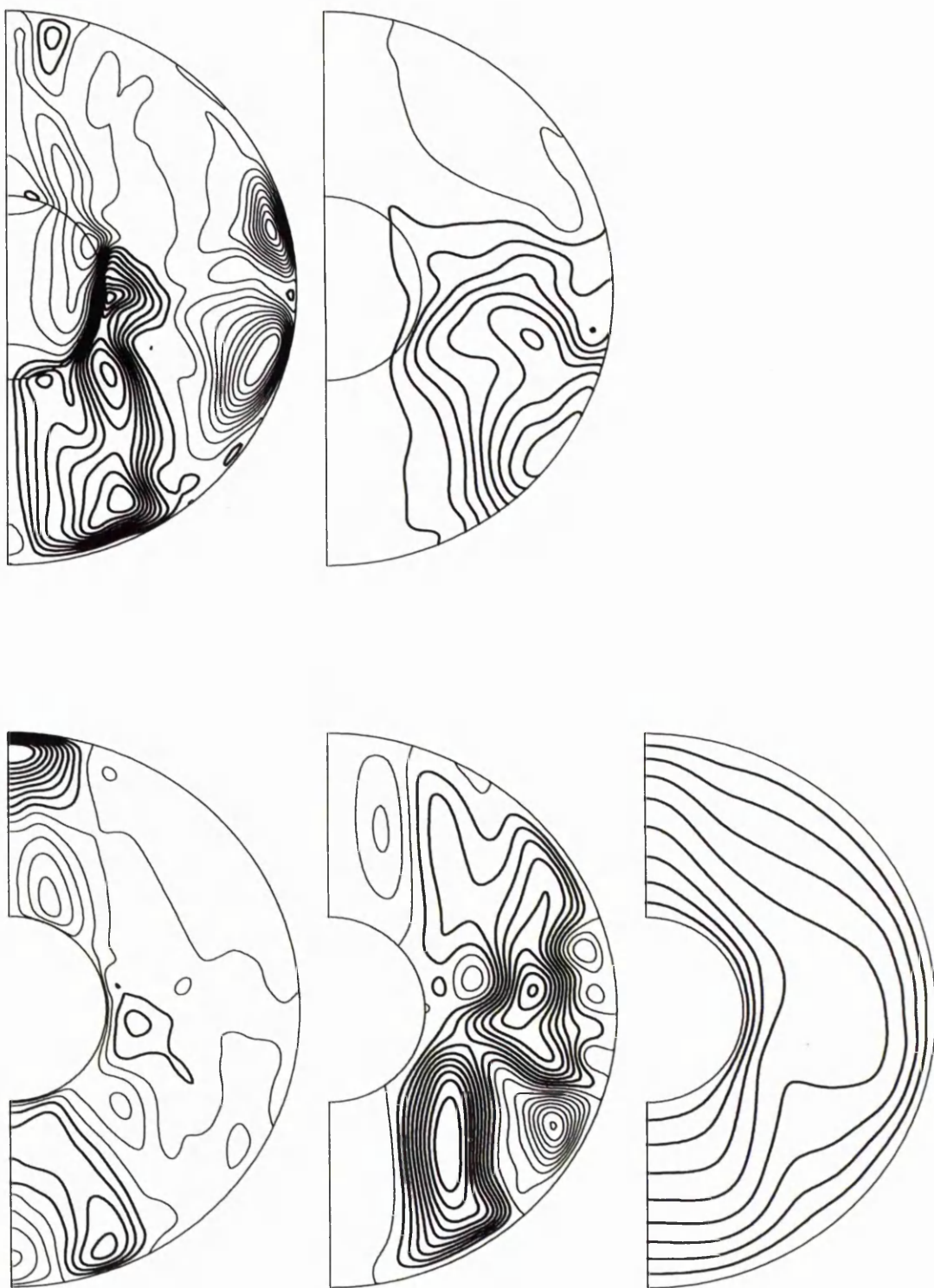
Figure 5.10: A snapshot of the axisymmetric quantities for $Ro = 1 \times 10^{-4}$, $Ra = 60$, at $\tau = 2$ with $m = 4$.

discussion will therefore be limited to a qualitative analysis. However, for the chaotic and periodic solutions obtained at $Ro = 1 \times 10^{-4}$, the magnitudes of the z-components of the corresponding axisymmetric torques about the z-axis, due to these forces are calculated and compared in Table 5.3. The pressure gradient, about which we have no direct information, and the buoyancy do not contribute to this component of the torque, and so a clearer understanding of the balance of the other forces in the momentum equation, for our model, can be obtained.

Before discussing the effect of varying Ro on the force balance, it seems sensible to discuss the balance in the absence of inertia. In this case of course the $Ro \partial \mathbf{U} / \partial t$ term will not appear. The momentum equation is separated into its three (r, θ, ϕ) components, with the axisymmetric and non-axisymmetric forces calculated separately. For the dipole solution with $Ro = 0$, the dynamo appears to be operating in a different dynamic regime, inside and outside the tangent cylinder. The buoyancy force is, of course, only present in the r component, and is always the dominant term inside the tangent cylinder, but outside the tangent cylinder it is not so dominant, although it still appears at leading order with the Lorentz force. Inside the tangent cylinder the Coriolis and Lorentz forces generally occur at leading order, with the viscous force generally at least one order of magnitude behind, although it can occasionally assume a more prominent role. Outside the tangent cylinder the viscous force can play a significant role in the momentum equation. This appears to be at the expense of the Coriolis force which can assume very small values.

When inertia is included in the model, the same general behaviour is observed, but with some important differences. Inside the tangent cylinder the inertial force is usually the weakest, although it can be of the same order as the viscous force. As the value of Ro increases the inertial term begins to play a more significant role in the momentum balance. This seems to be coupled with a general weakening of the Lorentz force. Outside the tangent cylinder, on the other hand, inertia seems to play very a

99

lesser role as Ro is increased. The buoyancy and Lorentz forces are still dominant, and the Coriolis force plays more of a role in the θ and ϕ components, but can still be very weak in the r component. We have already commented on the role played by the increasingly significant inertial term in halting magnetic field generation.

The differences between the chaotic and periodic solutions are subtle, with only very small perturbations seeming to be required to change state. It is therefore of interest to see if examination of the torque balance for each of the different solutions will yield any further understanding of these differences. The results for the z-component of the axisymmetric torques inside and outside the tangent cylinder are given in Table 5.3. The relative weakness of the inertial term, for this value of Ro, can be clearly seen. The main difference between the two solutions seems to lie in the Lorentz force, which is weakest for the periodic solution. These results have been produced by calculating the magnitudes of the forces for the final solution of each run, but similar results are obtained using different (available) points.

Table 5.3: The magnitude of the z-components of the torques in the axisymmetric momentum equation for the chaotic and periodic solutions at $Ro = 1 \times 10^{-4}$.

	Inside TC ($r \approx 1, \theta \approx \pi/10$)		Outside TC ($r \approx 1, \theta \approx \pi/5$)	
	Chaotic	Periodic	Chaotic	Periodic
$Ro\partial\mathbf{U}/\partial t$	-1.02×10^{-1}	-7.54×10^{-2}	1.27×10^{-2}	-9.02×10^{-2}
$Ro(\mathbf{U} \cdot \nabla)\mathbf{U}$	1.41×10^{-1}	2.57×10^{-2}	5.20×10^{-1}	1.58×10^{0}
$(\nabla \times \mathbf{B}) \times \mathbf{B}$	-1.37×10^{0}	-4.30×10^{-1}	2.15×10^{0}	9.63×10^{-2}
$E\nabla^2\mathbf{U}$	2.29×10^{-1}	-3.93×10^{-1}	-1.06×10^{-1}	7.13×10^{-1}
$\mathbf{1}_z \times \mathbf{U}$	-1.17×10^{0}	-7.75×10^{-1}	1.51×10^{0}	-6.87×10^{-1}
$Total$	4.85×10^{-3}	-2.04×10^{-3}	-9.39×10^{-4}	-1.83×10^{-3}

Chapter 6

Conclusions

The aim of this thesis is to investigate the influence of the choice of different parameter values on $2\frac{1}{2}D$ hydromagnetic dynamo solutions. We believe that our results have broad implications for numerical dynamo modelling, while retaining some relevance to the more complicated $3D$ numerical dynamo models. Some parameters are more amenable to change than others, and we have conducted as extensive a survey as has been possible. Three separate studies have been undertaken, one to establish the influence of varying Ra at two different values of m, one to obtain the important effect of varying χ, and the last study which establishes the effect of introducing inertia to a solution, and also examines the effect of varying the value of Ro.

From the first study we have observed that at both $m = 2$ and $m = 4$, the time dependence of the axisymmetric magnetic field is highly dependent on the value of Ra. This suggests that interpreting the details of any dynamo solutions obtained for a single value of Ra, may be specific to that value, and so care should be exercised in both the initial choice of Ra, and interpreting the results obtained with it. Since the value of Ra is unknown for the Earth, or any other planetary body, then this is a serious consideration for numerical dynamo modelling. Qualitatively similar behaviour is observed for different sources of thermal buoyancy, suggesting that the actual form of driving does not significantly change the behaviour observed. By comparing the results for the two different values of m, it is clear that the dependence on Ra is completely

different for the two values of m. This means that the $2\frac{1}{2}D$ model, at least in the Busse-Zhang parameter regime, is too severely truncated in ϕ. Work currently under way to increase the truncation in ϕ has found that the dominant value of m increases with the number of modes included (Sarson et al. 1998a) confirming this to be the case.

In Chapter 4 we have found that the effect of varying the radius of a finitely conducting inner core is not quite as expected. For an inner core, which is large enough to allow significant competition between regions inside and outside the tangent cylinder, then the time dependence of the magnetic field is chaotic. The behaviour of the magnetic field becomes less complicated as the inner core size increases, as might be anticipated, and in fact becomes periodic. It is at small inner core radii, where the time dependence of the solution remains regular and independent of χ, that the results are unexpected. As discussed in Chapter 4, this behaviour can be attributed to the weak interaction between regions inside and outside the tangent cylinder. So do we contradict the assertion of Hollerbach and Jones that the inner core is the key to the reversal frequency?

The strong-field dynamos we obtain for $m = 2$ never reverse. It is equally possible that our run time is too short, or that the solution itself does not reverse. All work carried out to date suggests that reversals are not observed until the full symmetry is included. Despite not finding any reversals, we believe that we reinforce the claim of Hollerbach and Jones for the following reasons. Our model is fully dynamic, rather than an $\alpha\omega$ model, with a solution which exhibits different time dependence and structure. Yet still we find that, for a reasonable size of inner core, the magnetic field in the outer core is stabilised as the inner core radius increases as predicted. Additionally, Hollerbach and Jones found no solutions for $\chi \leq 0.25$ and so could not really make any predictions as to what would occur at these small radii.

It is also worth remarking on the results for $\chi = 0.45$ and 0.50, which suggest that

the growth of the inner core may be capable of shutting off the dynamo. A similar effect has also been observed at a slightly smaller inner core radius by Jault (1996) in a mixed parity model. This effect is due to the increase in Ra_c with χ as the convection is constrained to a thinner shell. Increasing Ra sufficiently does generate a magnetic field, with significant increase in the value of Ra required at $\chi = 0.50$.

With the full inertial term included in the problem we find solutions with similar structure to those obtained with $Ro = 0$. These solutions themselves bear some resemblance to weak field solutions which were obtained in our study in Chapter 3. Indeed we find two possible solutions, one with chaotic time dependence which reverses frequently, and one with periodic time dependence which oscillates regularly. These solutions only seem to co-exist for $Ro \approx 1 \times 10^{-4}$. If Ro is increased beyond $Ro = 5 \times 10^{-4}$ then no magnetic field is maintained, even with a larger value of Ra and/or different initial conditions. This may be explained by consideration of the force balance in the momentum equation. As the value of Ro increases the more significant the role played by the inertial term in this balance. The viscous force remains at about the same magnitude, and it is the Lorentz force which is weakened to compensate. With stronger inertia and viscosity the fluid will be more difficult to set in motion, while decreasing the Lorentz force, results in a lower value of Λ, which in turn increases the value of Ra_c. This suggests that using stress-free boundary conditions to model viscous effects may have some merit, given our value of E. For values of $Ro \lesssim 1 \times 10^{-4}$ the periodic solutions are preferred, with the flow structure becoming increasingly similar to that obtained with $Ro = 0$.

In summary inertia can have a considerable effect on the time dependence of the magnetic field and flow, although it seems to have less effect on the flow structures obtained. If no-slip boundary conditions have to be employed then it will be advantageous to prescribe as low a value of Ro as possible. With inertia present, and if the choice is available, stress-free boundary conditions may not only better represent the

103

expected viscous effects, but may also permit a wider examination of parameter space. Future work with the code should consider this in more detail.

Our model of the geodynamo is as simple as possible, while retaining the essential physics, and throughout the text we have made the simplifications explicit. Nevertheless, our results have broad implications for numerical dynamo modelling. In particular, we show that by systematically changing the radius of a finitely conducting inner core, the diffusion time of the inner core and the changing geometry of the convecting region, both have an effect on the generated magnetic field. Too much emphasis cannot be placed on a solution obtained for a fixed value of Ra, and in models which use thermal buoyancy, the actual source of the buoyancy does not appear to be qualitatively important. We have also produced the first results with a $2\frac{1}{2}D$ model which includes the full inertial term. These results seem to confirm our suspicion that inertia can have a significant effect on the time dependence of the solution when included in a model with strong viscosity, and perhaps suggest that viscous effects should be minimised, by incorporating stress-free boundary conditions, to better represent the force balance in the core.

References

Abramowitz, M. & Stegun, I.A., 1965. Handbook of mathematical functions, Dover, New York.

Bergman, M.I. & Fearn, D.R., 1994. Chimneys on the Earth's inner-outer core boundary? *Geophys. Res. Lett.* **21** 477-480.

Bergman, M.I., Fearn, D.R., Bloxham, J. & Shannon, M.C., 1997. Convection and channel formation in solidifying Pb-Sn alloys. *Metall. Trans.* **28A** 859-866.

Bloxham, J., 1998. Dynamics of angular momentum in the Earth's core. *Ann. Rev. Earth Planet. Sci* **26** 501-517.

Braginsky, S.I., 1994. The nonlinear dynamo and Model-Z, In: M.R.E. Proctor and A.D. Gilbert (Editors), Lectures on solar and planetary dynamos, Cambridge University Press, Cambridge, pp. 267-304

Busse, F.H., 1970. Thermal instabilities in rapidly rotating systems. *J. Fluid Mech.* **44** 441-460.

Busse, F.H., Grote, E. & Tilgner, A., 1998. On convection driven dynamos in rotating spherical shells. *Studia geoph. et geod.* **42** 1-6.

Canuto, C., Hussaini, M.Y., Quarteroni, A. & Zang, T.A., 1988. Spectral methods in fluid dynamics, Springer-Verlag, Berlin.

Cardin, P. & Olson, P., 1994. Chaotic thermal convection in a rapidly rotating spherical shell - consequences for flow in the outer core. *Phys. Earth Planet. Int.* **82** 235-259.

Carrigan, C.R. & Busse, F.H., 1983. An experimental and theoretical investigation of the onset of convection in rotating spherical shells. *J. Fluid Mech.* **126** 287-305.

Chalmers, B., 1964. Principles of solidification, Wiley, New York.

Chandrasekhar, S., 1961. Hydrodynamic and hydromagnetic stability, Oxford University Press, London.

Channell, J.E.T., Hodell, D.A., McManus, J. & Lehman, B., 1998. Orbital modulation of the Earth's magnetic field intensity. *Nature* **394** 464-468.

Christensen, U., Olson, P. & Glatzmaier, G.A., 1998. A dynamo model interpretation of geomagnetic field structures. *Geophys. Res. Lett.* **25** 1565-1568.

Christensen, U., Olson, P. & Glatzmaier, G.A., 1999. Numerical modelling of the geodynamo: a systematic parameter study. *Geophys. J. Int.* **138** 393-409.

Copley, S.M., Giamei A.F., Johnson, S.M. & Hornbecker, M.F., 1970. The origin of freckles in unidirectionally solidified castings. *Metall. Trans.* **1** 2193-2204.

Cowling, T.G., 1934. The magnetic field of sunspots. *Mon. Not. R. Astr. Soc.* **94** 39-48.

Creager, K.C., 1997. Inner core rotation rate from small-scale heterogeneity and time-varying travel times. *Science* **278** 1284-1288.

Fearn, D.R., 1994. Nonlinear planetary dynamos, In: M.R.E. Proctor and A.D. Gilbert (Editors), Lectures on solar and planetary dynamos, Cambridge University Press, Cambridge, pp. 219-244

Fearn, D.R., 1998. Hydromagnetic flows in planetary cores. *Rep. Prog. Phys.* **61** 175-235.

Fearn, D.R. & Proctor, M.R.E., 1983a. Hydromagnetic waves in a differentially rotating sphere. *J. Fluid Mech.* **128** 1-20.

Fearn, D.R. & Proctor, M.R.E., 1983b. The stabilising role of differential rotation on hydromagnetic waves. *J. Fluid Mech.* **128** 21-36.

Fearn, D.R., Proctor, M.R.E. & Sellar, C.C., 1994. Nonlinear magnetoconvection in a rapidly rotating sphere and Taylor's constraint. *Geophys. Astrophys. Fluid Dynam.* **77** 111-132.

Glatzmaier, G.A. & Roberts, P.H., 1995a. A three dimensional convective dynamo solution with rotating and finitely conducting inner core and mantle. *Phys. Earth Planet. Int.* **91** 63-75.

Glatzmaier, G.A. & Roberts, P.H., 1995b. A 3-D self consistent computer simulation of a geomagnetic field reversal. *Nature* **377** 203-209.

Glatzmaier, G.A. & Roberts, P.H., 1996a. On the magnetic sounding of planetary interiors. *Phys. Earth Planet. Int.* **98** 207-220.

Glatzmaier, G.A. & Roberts, P.H., 1996b. An anelastic evolutionary geodynamo simulation driven by compositional and thermal convection. *Physica D* **97** 81-94.

Glatzmaier, G.A. & Roberts, P.H., 1996c. Rotation and magnetism of the earth's inner core. *Science* **274** 1887-1891.

Glatzmaier, G.A. & Roberts, P.H., 1997. Simulating the geodynamo. *Contemporary Physics* **38** 269-288.

Glatzmaier, G.A. & Roberts, P.H., 1998. Dynamo theory then and now. *Int. J. Eng. Sci.* **36** 1325-1338.

Glatzmaier, G.A., Coe, R.S., Hongre, L. & Roberts, P.H., 1999. How the Earth's mantle controls the frequency of geomagnetic reversals. *Nature* Submitted.

Greenspan, H.P., 1968. The theory of rotating fluids, Cambridge University Press, London.

Gubbins, D., 1999. The distinction between geomagnetic excursions and reversals. *Geophys. J. Int.* **137** F1-F3.

Guyodo, Y. & Valet, J.-P., 1999. Global changes in intensity of the Earth's magnetic field during the past 800 kyr. *Nature* **399** 249-252.

Hollerbach, R., 1994a. Imposing a magnetic field across a nonaxisymmetric shear layer in a rotating spherical shell. *Phys. Fluids* **6** 2540-2544.

Hollerbach, R., 1994b. Magnetohydrodynamic Ekman and Stewartson layers in a rotating spherical shell. *Proc. Roy. Soc. Lond. A.* **444** 333-346.

Hollerbach, R., 1996. On the theory of the geodynamo. *Phys. Earth Planet. Int.* **98** 163-185.

Hollerbach, R., 1999. A spectral solution of the magnetoconvection equations in spherical geometry. *Int. J. Numer. Meth. Fluids* submitted.

Hollerbach, R. & Jones, C.A., 1993a. A geodynamo model incorporating a finitely conducting inner core. *Phys. Earth Planet. Int.* **75** 317-327.

Hollerbach, R. & Jones, C.A., 1993b. Influence of the Earth's inner core on geomagnetic fluctuations and reversals. *Nature* **365** 541-543.

Hollerbach, R. & Jones, C.A., 1995. On the magnetically stabilising role of the Earth's inner core. *Phys. Earth Planet. Int.* **87** 171-181.

Hollerbach, R. & Proctor, M.R.E, 1993. Non-axisymmetric shear layers in a rotating spherical shell, In: M.R.E. Proctor, P.C. Matthews and A.M. Rucklidge (Editors), Solar and planetary dynamos, Cambridge University Press, Cambridge, pp. 145-152

Huppert, H.E., 1990. The fluid mechanics of solidification. *J. Fluid Mech.* **212** 209-240.

Jacobs, J.A., 1953. The Earth's inner core. *Nature* **172** 297-300.

Jault, D., 1995. Model-Z by computation and Taylor's condition. *Geophys. Astrophys. Fluid Dynam.* **79** 99-124.

Jault, D., 1996. Sur l'inhibition de la régénération du champ magnétique dans certains modèles de dynamo planétaire en présence d'une graine solide. *C. R. Acad. Sci. II.* **323** 451-458.

Jones, C.A., Longbottom, A.W. & Hollerbach, R., 1995. A self-consistent convection driven geodynamo model using a mean field approximation. *Phys. Earth Planet. Int.* **92** 119-141.

Juarez, M.T., Tauxe, L., Gee, J.S. & Pick, T., 1998. The intensity of the Earth's magnetic field over the past 160 million years. *Nature* **394** 878-881.

Kageyama, A. & Sato, T., 1997. Generation mechanism of a dipole field by a magnetohydrodynamical dynamo. *Phys. Rev. E* **56** 4617-4626.

Kerswell, R.R, 1996. Upper bounds on the energy dissipation in turbulent precession. *J. Fluid Mech.* **321** 335-370.

Knittle, E. & Jeanloz, R., 1989. Simulating the core-mantle boundary: An experimental study of high-pressure reactions between silicates and liquid iron . *Geophys. Res. Lett.* **16** 609-612.

Knobloch, E., 1998. Rotating convection: recent developments. *Int. J. Eng. Sci.* **36** 1421-1450.

Kuang, W. & Bloxham, J., 1997. An Earth-like numerical dynamo model. *Nature* **389** 371-374.

Kuang, W. & Bloxham, J., 1999. Numerical modelling of magnetohydrodynamic convection in a rapidly rotating spherical shell I: weak and strong field dynamo action. *J. Comp. Phys.* **153** 51-81.

Kutzner, C. & Christensen, U., 2000. Effects of driving mechanisms in geodynamo models. *Geophys. Res. Lett.* **27** 29-32.

Labrosse, S.,Poirier, J.P. & Le-Mouel, J.L., 1997. On the cooling of the Earth's core. *Phys. Earth Planet. Int.* **99** 1-17.

Larmor, J., 1919a. Possible rotational origin of magnetic fields of sun and earth. *Elec. Rev.* **85** 412-.

Larmor, J., 1919b. How could a rotating body such as the Sun become a magnet?. *Rep. Br. Assoc. Adv. Sci. A* 159-160.

Lehmann, I., 1936. . *P. Bur. Centr. Seism. Internat. A* **14** 3-31.

Lister, J.R. & Buffett, B.A. , 1995. The strength and efficiency of thermal and compositional convection in the geodynamo. *Phys. Earth Planet. Int.* **92** 17-30.

Loper, D.E., 1983. Structure of the inner core boundary. *Geophys. Astrophys. Fluid Dynam.* **25** 139-155.

Loper, D.E. & Roberts, P.H., 1981. A study of conditions at the inner core boundary of the Earth. *Phys. Earth Planet. Int.* **24** 302-307.

McElhinny, M.W. & Senanayake, W.E., 1980. Paleomagnetic evidence for the existence of the geomagnetic field 3.5 Ga ago. *J. Geophys. Res.* **85** 3523-3528.

Malkus, W.V.R., 1994. Energy sources for planetary dynamos, In: M.R.E. Proctor and A.D. Gilbert (Editors), Lectures on solar and planetary dynamos, Cambridge University Press, Cambridge, pp. 161-179

Malkus, W.V.R. & Proctor, M.R.E, 1975. The macrodynamics of α-effect dynamos in rotating fluids. *J. Fluid Mech.* **67** 417-433.

Mao, H. & Hemley, R.J., 1998. New windows on the Earth's Deep Interior. *Rev. Mineral.* **37** 1-28.

110

Merrill, R.T., McElhinny, W., & McFadden, P.L., 1996. The magnetic field of the Earth, Academic Press, San Diego.

Milankovitch, M. , 1941. Serb. Akad. Beogr. Spec. Publ., 132, (Translated - Israel Program for Scientific Translation, Jerusalem, 1969).

Morelli, A., Dziewonski, A.M. & Woodhouse, J.H., 1986. Anisotropy of the inner core inferred from PKIKP travel times . *Geophys. Res. Lett.* **13** 1545-1548.

Okal, E.A. & Cansi, Y., 1998. Detection of PKJKP at intermediate periods by progressive multi-channel correlation. *Earth Planet. Sci. Lett.* **164** 23-30.

Poirier, J.P., 1994. Physical properties of the Earth's core. *C. R. Acad. Sci. II.* **318** 341-350.

Roberts, P.H., 1968. On the thermal instability of a rotating fluid sphere containing heat sources. *Phil. Trans. Roy. Soc. Lond. A.* **263** 93-117.

Roberts, P.H., 1994. Fundamentals of dynamo theory, In: M.R.E. Proctor and A.D. Gilbert (Editors), Lectures on solar and planetary dynamos, Cambridge University Press, Cambridge, pp. 1-58

Rohm, A.H.E., Trampert, J., Paulssen, H. & Snieder, R.K., 1999. Bias in reported seismic arrival times deduced from the ISC Bulletin. *Geophys. J. Int.* **137** 163-174.

Sakuraba, A. & Kono, M., 1999. Effect of the inner core on the numerical simulation of the magnetohydrodynamic dynamo. *Phys. Earth Planet. Int.* **111** 105-121.

Sarson, G.R. & Jones, C.A., 1999. A convection driven geodynamo reversal model. *Phys. Earth Planet. Int.* **111** 3-20.

Sarson, G.R., Jones, C.A. & Longbottom, A.W., 1997a. The influence of boundary region heterogeneities on the geodynamo. *Phys. Earth Planet. Int.* **101** 13-32.

Sarson, G.R., Jones, C.A., Zhang, K. & Schubert, G., 1997b. Magnetoconvection dy-

namos and the magnetic fields of Io and Ganymede. *Science* **276** 1106-1108.

Sarson, G.R., Jones, C.A. & Hollerbach, R., 1998a. Three-dimensional geodynamo calculations of limited azimuthal resolution. Poster SEDI.

Sarson, G.R., Jones, C.A. & Longbottom, A.W., 1998b. Convection driven geodynamo models of varying Ekman number. *Geophys. Astrophys. Fluid Dynam.* **88** 225-259.

Sarson, G.R., Jones,C.A. & Zhang, K., 1999. Dynamo action in a uniform ambient field. *Phys. Earth Planet. Int.* **111** 47-68.

Schubert, G., Zhang, K., Kivelson, M.G. & Anderson, J.D., 1996. The magnetic field and internal structure of Ganymede. *Nature* **384** 544-545.

Shearer, P. & Masters, G., 1990. The density and shear velocity contrast at the inner core boundary. *Geophys. J. Int.* **102** 491-498.

Skinner, P.H. & Soward, A.M., 1988. Convection in a rotating magnetic system and Taylor's constraint I. *Geophys. Astrophys. Fluid Dynam.* **44** 91-116.

Skinner, P.H. & Soward, A.M., 1990. Convection in a rotating magnetic system and Taylor's constraint II. *Geophys. Astrophys. Fluid Dynam.* **60** 335-356.

Song, X. & Helmberger, D.V., 1998. Seismic evidence for an inner core transition zone. *Science* **282** 924-927.

Song, X. & Richards, P.G., 1996. Seismological evidence for differential rotation of the Earth's inner core. *Nature* **382** 221-224.

Souriau, A., Roudil, P. & Moynot, B., 1997. Inner core differential rotation: facts and artefacts. *Geophys. Res. Lett.* **24** 2103-2106.

Souriau, A., 1998a. Earth's inner core - Is the rotation real? *Science* **281** 55-56.

Souriau, A., 1998b. New seismological constraints on differential rotation of the inner core from Novaya Zemlya events recorded at DRV, Antarctica. *Geophys. J. Int.* **134**

F1-F5.

Soward, A.M., 1977. On the finite amplitude thermal instability of a rapidly rotating fluid sphere. *Geophys. Astrophys. Fluid Dynam.* **9** 19-74.

Soward, A.M., 1986. Non-linear marginal convection in a rotating magnetic system. *Geophys. Astrophys. Fluid Dynam.* **35** 329-371.

Stevenson, D.J., Spohn, T. & Schubert, G., 1983. Magnetism and thermal evolution of the terrestrial planets. *Icarus* **54** 466-489.

Stewartson, K., 1966. On almost rigid rotations part 2. *J. Fluid Mech.* **26** 131-144.

Stixrude, L. & Brown, J.M., 1998. The Earth's core. *Rev. Mineral.* **37** 261-282.

Su, W. & Dziewonski, A.M., 1995. Inner core anisotropy in three dimensions. *J. Geophys. Res.* **100** 9831-9852.

Tait, S. & Jaupart, C., 1992. Compositional convection in a reactive crystalline mush and melt differentiation. *J. Geophys. Res.* **97** 6735-6756.

Taylor, J.B., 1963. The magnetohydrodynamics of a rotating fluid and the Earth's dynamo problem. *Proc. Roy. Soc. Lond. A.* **274** 274-283.

Walker, M.R., 1998. Nonlinear magnetoconvection and the geostrophic flow-subcritical solutions. *Studia geoph. et geod.* **42** 272-279.

Walker, M.R. & Barenghi, C.F., 1997a. Magnetoconvection in a rapidly rotating sphere. *Geophys. Astrophys. Fluid Dynam.* **85** 129-162.

Walker, M.R. & Barenghi, C.F., 1997b. On a numerical solution to the magnetoconvection problem. *Acta Astron. et Geophys. Univ. Comenianae* **XIX** 293-303.

Walker, M.R. & Barenghi, C.F., 1998. Accurate numerical computations of Taylor integrals. *Geophys. Astrophys. Fluid Dynam.* **87** 173-191.

Walker, M.R. & Barenghi, C.F., 1999. Nonlinear magnetoconvection and the geostrophic

flow. *Phys. Earth Planet. Int.* **111** 35-46.

Walker, M.R., Barenghi, C.F., & Jones C.A., 1998. A note on dynamo action at asymptotically small Ekman number. *Geophys. Astrophys. Fluid Dynam.* **88** 261-275.

de Wijs, G.A., Kresse, G., Vocadlo, L., Dobson, D., Alfé, D., Gillan, M.J. & Price, G.D., 1998. The viscosity of liquid iron at the physical conditions of the Earth's core. *Nature* **392** 805-807.

Woodhouse, J.H., Giardini, D. & Li, X.D., 1986. Evidence for inner core anisotropy from free oscillations. *Geophys. Res. Lett.* **13** 1549-1552.

Worster, M.G., 1997. Convection in mushy layers. *Ann. Rev. Fluid. Mech.* **29** 91-122.

Zhang, K., 1992. Spiralling columnar convection in rapidly rotating spherical fluid shells. *J. Fluid Mech.* **236** 535-556.

Zhang, K., 1994. On coupling between the Poincaré equation and the heat equation. *J. Fluid Mech.* **268** 211-229.

Zhang, K. & Busse, F.H., 1989. Magnetohydrodynamic dynamos in rotating spherical shells. *Geophys. Astrophys. Fluid Dynam.* **49** 97-116.

Zhang, K. & Fearn, D.R., 1994. Hydromagnetic waves in rapidly rotating spherical shells generated by magnetic toroidal decay modes. *Geophys. Astrophys. Fluid Dynam.* **77** 133-157.

Zhang, K. & Jones, C.A., 1994. Convective motions in the Earth's fluid core. *Geophys. Res. Lett.* **21** 1939-1942.

Zhang, K. & Jones, C.A., 1996. On small Roberts number magnetoconvection in rapidly rotating systems. *Proc. Roy. Soc. Lond. A.* **452** 981-995.

Zhang, K. & Jones, C.A., 1997. The effect of hyperviscosity on geodynamo models.

Geophys. Res. Lett. **24** 2869-2872.

Appendix A

Model 1

A.1   Numerical method

From Chapter 2 the governing equations are

$$\mathbf{1}_z \times \mathbf{U} = -\nabla P + E\nabla^2 \mathbf{U} + (\nabla \times \mathbf{B}) \times \mathbf{B} + qRaT\mathbf{r} \tag{A.1}$$

$$\frac{\partial \mathbf{B}}{\partial t} = \nabla \times (\mathbf{U} \times \mathbf{B}) + \nabla^2 \mathbf{B} \tag{A.2}$$

$$\frac{\partial T}{\partial t} + \mathbf{U} \cdot \nabla T = q\nabla^2 T + \hat{\epsilon} \tag{A.3}$$

$$\nabla \cdot \mathbf{U} = \nabla \cdot \mathbf{B} = 0 \tag{A.4}$$

The quantities $\mathbf{B}$, $\mathbf{U}$, T and P are separated into axisymmetric and non-axisymmetric components as follows,

$$\mathbf{B} = \overline{\mathbf{B}} + \mathbf{b}, \quad \mathbf{U} = \overline{\mathbf{U}} + \mathbf{u}, \quad T = T_0 + \overline{T} + T', \quad P = \overline{P} + p \tag{A.5}$$

The numerical method which we employ excludes the pressure P, but it is included here for completeness. The barred variables represent the axisymmetric components and T_0 is the temperature profile in the absence of convection. This separation into axisymmetric and non-axisymmetric components leads to two sets of equations as follows:

116

Non-axisymmetric equations

$$\mathbf{1}_z \times \mathbf{u} - E\nabla^2\mathbf{u} = -\nabla p + (\nabla \times \overline{\mathbf{B}}) \times \mathbf{b} + (\nabla \times \mathbf{b}) \times \overline{\mathbf{B}} + qRaT'\mathbf{r} \qquad (A.6)$$

$$\frac{\partial \mathbf{b}}{\partial t} - \nabla^2\mathbf{b} = \nabla \times (\overline{\mathbf{U}} \times \mathbf{b} + \mathbf{u} \times \overline{\mathbf{B}}) \qquad (A.7)$$

$$\frac{\partial T'}{\partial t} - q\nabla^2 T' = -\overline{\mathbf{U}} \cdot \nabla T' - \mathbf{u} \cdot \nabla(T_0 + \overline{T}) \qquad (A.8)$$

$$\nabla \cdot \mathbf{u} = \nabla \cdot \mathbf{b} = 0 \qquad (A.9)$$

Since a finitely conducting inner core is included, the following equations must also be solved in the inner core,

$$\frac{\partial \mathbf{b}}{\partial t} - \nabla^2\mathbf{b} = -\Omega_i \frac{\partial \mathbf{b}}{\partial \phi} \qquad (A.10)$$

$$\nabla \cdot \mathbf{b} = 0. \qquad (A.11)$$

Axisymmetric equations

$$\mathbf{1}_z \times \overline{\mathbf{U}} - E\nabla^2\overline{\mathbf{U}} = -\nabla \overline{P} + (\nabla \times \overline{\mathbf{B}}) \times \overline{\mathbf{B}} + \overline{(\nabla \times \mathbf{b}) \times \mathbf{b}} + qRa(T_0 + \overline{T})\mathbf{r} \qquad (A.12)$$

$$\frac{\partial \overline{\mathbf{B}}}{\partial t} - \nabla^2\overline{\mathbf{B}} = \nabla \times (\overline{\mathbf{U}} \times \overline{\mathbf{B}}) + \nabla \times \overline{(\mathbf{u} \times \mathbf{b})} \qquad (A.13)$$

$$\frac{\partial \overline{T}}{\partial t} - q\nabla^2\overline{T} = -\overline{\mathbf{U}} \cdot \nabla(T_0 + \overline{T}) - \overline{\mathbf{u} \cdot \nabla T'} + \hat{\epsilon} \qquad (A.14)$$

$$\nabla \cdot \overline{\mathbf{U}} = \nabla \cdot \overline{\mathbf{B}} = 0 \qquad (A.15)$$

The equations to be solved in the inner core are in this case,

$$\frac{\partial \overline{\mathbf{B}}}{\partial t} - \nabla^2\overline{\mathbf{B}} = 0 \qquad (A.16)$$

$$\nabla \cdot \overline{\mathbf{B}} = 0 \qquad (A.17)$$

The nonlinear terms with the overbar are the axisymmetric parts of the quadratic non-axisymmetric forcing terms, which can be thought of as an azimuthal average,

$$\bar{f}(r,\theta) \equiv \frac{1}{2\pi} \int_0^{2\pi} f(r,\theta,\phi) d\phi \qquad (A.18)$$

The poloidal-toroidal decomposition is adopted for the flow and the magnetic field as follows:

$$\overline{\mathbf{U}} = \nabla \times (\psi \mathbf{1}_\phi) + v \mathbf{1}_\phi \qquad (A.19)$$

$$\overline{\mathbf{B}} = \nabla \times (A \mathbf{1}_\phi) + B \mathbf{1}_\phi \qquad (A.20)$$

$$\mathbf{u} = \nabla \times (e \mathbf{1}_r) + \nabla \times \nabla \times (f \mathbf{1}_r) \qquad (A.21)$$

$$\mathbf{b} = \nabla \times (g \mathbf{1}_r) + \nabla \times \nabla \times (h \mathbf{1}_r) \qquad (A.22)$$

Such a decomposition automatically satisfies equations (A.4), and reduces the vector equations, to equations involving the scalars ψ, v, A, B, e, f, g and h, as well as $\overline{T}$, T_0 and T'. Each of these scalars is expanded in the outer core as shown below.

$$A(r,\theta) = \sum_{n=1}^{N1} \sum_{l=1}^{M1+2} A_{nl}^{(o)} \widehat{T}_{l-1}(x_o) P_{2n-1}^1(\cos\theta) \qquad (A.23)$$

$$B(r,\theta) = \sum_{n=1}^{N1} \sum_{l=1}^{M1+2} B_{nl}^{(o)} \widehat{T}_{l-1}(x_o) P_{2n}^1(\cos\theta) \qquad (A.24)$$

$$\psi(r,\theta) = \sum_{n=1}^{N2} \sum_{l=1}^{M2+4} \psi_{nl}^{(o)} \widehat{T}_{l-1}(x_o) P_{2n}^1(\cos\theta) \qquad (A.25)$$

$$v(r,\theta) = \sum_{n=1}^{N2} \sum_{l=1}^{M2+2} v_{nl}^{(o)} \widehat{T}_{l-1}(x_o) P_{2n-1}^1(\cos\theta) \qquad (A.26)$$

118

$$\overline{T}(r,\theta) = \sum_{n=1}^{N1} \sum_{l=1}^{M1+2} \overline{T}_{nl}^{(o)} \widehat{T}_{l-1}(x_o) P_{2n-2}^0(\cos\theta) \qquad (A.27)$$

$$g(r,\theta,\phi) = \sum_{n=1}^{N1} \sum_{l=1}^{M1+2} g_{nl}^{(o)} \widehat{T}_{l-1}(x_o) P_{2n+m-2}^m(\cos\theta) e^{im\phi} \qquad (A.28)$$

$$h(r,\theta,\phi) = \sum_{n=1}^{N1} \sum_{l=1}^{M1+2} h_{nl}^{(o)} \widehat{T}_{l-1}(x_o) P_{2n+m-1}^m(\cos\theta) e^{im\phi} \qquad (A.29)$$

$$e(r,\theta,\phi) = \sum_{n=1}^{N2} \sum_{l=1}^{M2+2} e_{nl}^{(o)} \widehat{T}_{l-1}(x_o) P_{2n+m-1}^m(\cos\theta) e^{im\phi} \qquad (A.30)$$

$$f(r,\theta,\phi) = \sum_{n=1}^{N2} \sum_{l=1}^{M2+4} f_{nl}^{(o)} \widehat{T}_{l-1}(x_o) P_{2n+m-2}^m(\cos\theta) e^{im\phi} \qquad (A.31)$$

$$T'(r,\theta,\phi) = \sum_{n=1}^{N1} \sum_{l=1}^{M1+2} T_{nl}'^{(o)} \widehat{T}_{l-1}(x_o) P_{2n+m-2}^m(\cos\theta) e^{im\phi} \qquad (A.32)$$

$$T_0(r) = \sum_{l=1}^{M1+2} \Theta_l \widehat{T}_{l-1}(x_o). \qquad (A.33)$$

Although we have explicitly assumed that $T_0 = T_0(r)$, in general θ and ϕ dependence can be included , by using suitable expansion functions. The quantity x_o takes values in the range (-1,1), with the transformation between x_o and the non-dimensional radius, r given by

$$r = \frac{r_1 + r_2}{2} + \frac{r_2 - r_1}{2} x_o \qquad (A.34)$$

where r_1 and r_2 are the non-dimensional radii of the ICB and CMB respectively. In addition A, B, g and h are expanded in the inner core as

$$A(r,\theta) = \sum_{n=1}^{N1} \sum_{l=1}^{\frac{M1}{2}+1} A_{nl}^{(i)} \widehat{T}_{2l-1}(x_i) P_{2n-1}^1(\cos\theta) \qquad (A.35)$$

119

$$B(r, \theta) = \sum_{n=1}^{N1} \sum_{l=1}^{\frac{M1}{2}+1} B_{nl}^{(i)} x_i \widehat{T}_{2l-1}(x_i) P_{2n}^1(\cos \theta) \tag{A.36}$$

$$g(r, \theta, \phi) = \sum_{n=1}^{N1} \sum_{l=1}^{\frac{M1}{2}+1} g_{nl}^{(i)} x_i^{k_1} \widehat{T}_{2l-1}(x_i) P_{2n+m-2}^m(\cos \theta) e^{im\phi} \tag{A.37}$$

$$h(r, \theta, \phi) = \sum_{n=1}^{N1} \sum_{l=1}^{\frac{M1}{2}+1} h_{nl}^{(i)} x_i^{k_2} \widehat{T}_{2l-1}(x_i) P_{2n+m-1}^m(\cos \theta) e^{im\phi} \tag{A.38}$$

The quantity x_i takes values in the range (0,1), with the transformation between x_i and r given by

$$x_i = \frac{r}{r_1} \tag{A.39}$$

In the expansions of g and h in the inner core $k_1 = 2$ and $k_2 = 1$ for even m, and $k_1 = 1$ and $k_2 = 2$ for odd m to ensure that the proper radial symmetry is attained. The radial expansion functions are Chebyshev polynomials, $\widehat{T}_l(x)$ (see Abramowitz and Stegun 1965). We will now see how using these functions allows the concentration of resolution near the boundaries (i.e. $x_o = \pm 1$), where thin boundary layers are expected to develop. Spherical harmonics, of appropriate order m, are used as the expansion functions in latitude and longitude, and, as the name suggests, are the natural expansion functions in a spherical geometry. Each spherical harmonic consists of a polynomial in θ, combined with an $e^{im\phi}$ term. The functions denoted $P_n^0(\cos \theta)$ are Legendre polynomials (see Abramowitz and Stegun 1965), and are used for the scalars describing $\overline{T}$ and T_0. Technically speaking these are the most natural functions to use for all the axisymmetric quantities, but A, B, v and ψ use $P_n^1(\cos \theta)$ which are associated Legendre polynomials of order 1, because of the poloidal-toroidal decomposition chosen. For the non-axisymmetric scalars, the expansion is done using associated Legendre polynomials $(P_n^m(\cos \theta))$ of order m, where m is the chosen value of the azimuthal wavenumber. This code adopts dipolar symmetry (see Chapter 2), which must be

120

achieved by a suitable choice of expansion functions for the individual scalars. To obtain the correct equatorial symmetry, A, v, $\overline{T}$, g, f, and T' must be symmetric about the equator and B, ψ, h, and e must be anti-symmetric. The symmetry adopted by each scalar will also be used in the numerical solution of the momentum equation. Each Legendre function is a polynomial in $\cos\theta$ and $\sin\theta$, the precise form of which depends on the degree n. By examining the symmetry of these polynomials about $\theta = \pi/2$, we can include only the polynomials, i.e. only the degrees which have the appropriate symmetry. In practice even degrees will be used for symmetric quantities and odd degrees for anti-symmetric quantities when m is even (including $m = 0$), and vice versa when m is odd. In a fully $3D$ code, we would also have to sum over m, but the $2\frac{1}{2}D$ approximation involves the prescription of just a single value. As a result the longitudinal solution structure is constrained to be periodic. In the code the spectral coefficients of the non-axisymmetric scalars are treated as complex quantities, with the physical variable being the real part of the quantity.

The radial truncation for the magnetic field and temperature is $M1$, while that for the flow is $M2$. In general $M2$ will be larger than $M1$ to take account of the finer structure observed for the flow. The summation range in l has either one, two or four extra coefficients included in order to deal with the boundary conditions. Similarly, $N1$ is the latitudinal truncation for the magnetic field and temperature, while that for the flow is $N2$.

A.1.1   Inner core rotation

We have already seen in Chapter 2 that the inner core rotation results from the action of electromagnetic and viscous torques on the boundary, via the equation (2.18). Since the inertia of the fluid is not included for this model, then the inertia of the inner core should also be excluded, because the inertial time scale of the inner core is comparable to the inertial time scales of the outer core. The equation determining Ω_i then reduces

to $\Gamma = 0$, which does not seem to include Ω_i at all. However if we evaluate the torques given in (2.19) individually then the following relation is found to hold

$$\frac{8\pi}{3} E r_1^4 \frac{d}{dr} \left(\frac{v(r)}{r} \right)_{r=r_1} = -(r_1)^3 \int_0^\pi \int_0^{2\pi} (b_r b_\phi + \overline{B}_r \overline{B}_\phi)_{r=r_1} \sin^2 \theta \, d\theta d\phi \qquad (A.40)$$

We require that the azimuthal flow on the ICB be equivalent to the solid body rotation of the inner core and achieve this by setting an inhomogeneous boundary condition for the appropriate spectral coefficients of v at the ICB. The relation given in (A.40) then acts as this boundary condition for v, since $\mathbf{B}$ is known at each time step. Having obtained v, the inner core rotation rate Ω_i is then obtained from the inhomogeneous boundary condition on v. Thus the calculation of the inner core rotation rate is performed in a very roundabout manner.

A.2 Momentum Equation

In the following discussion we will examine the numerical method for the non-axisymmetric momentum equation (A.6). The axisymmetric equation (A.12) is solved in a similar manner. Notice that (A.6) has now been presented with the viscous term on the left hand side, meaning that the linear diffusive operator is dealt with implicitly, in this case along with the Coriolis force. We don't want to have to calculate the pressure gradient $(-\nabla P)$, which is, in any case, believed to play essentially a passive role in the geodynamo. The method used to remove ∇P involves applying the curl operator, as $\nabla \times (\nabla \varphi) = \mathbf{0}$, for any arbitrary scalar φ. The remaining nonlinear Lorentz and buoyancy force terms are calculated explicitly. By applying the curl operator twice to the momentum equation and considering only the r component, then the equations to be solved are as follows

$$\mathbf{1}_r \cdot \nabla \times [\mathbf{1}_z \times \mathbf{u} - E\nabla^2 \mathbf{u}] = \mathbf{1}_r \cdot \nabla \times \mathbf{F}_m \qquad (A.41)$$

$$\mathbf{1}_r \cdot \nabla \times \nabla \times [\mathbf{1}_z \times \mathbf{u} - E\nabla^2 \mathbf{u}] = \mathbf{1}_r \cdot \nabla \times \nabla \times \mathbf{F}_m \qquad (A.42)$$

where

$$\mathbf{F}_m = qRaT'\mathbf{r} + (\nabla \times \overline{\mathbf{B}}) \times \mathbf{b} + (\nabla \times \mathbf{b}) \times \overline{\mathbf{B}}. \qquad (A.43)$$

These vector partial differential equations are reduced to two sets of simultaneous equations, which must be solved to obtain the spectral coefficients of the scalars describing the velocity. Unfortunately the presence of the Coriolis force on the left hand side means that these equations are coupled for the spectral coefficients e and f, through the spherical harmonic degree n, although the equations can still be treated separately for each m. By substituting for the components of the vector $\mathbf{u}$, using (A.30) and (A.31), the unit vector $\mathbf{1}_z = (\cos\theta, -\sin\theta, 0)$, and calculating the form of the ∇^2 operator gives the following equations,

$$\sum_{m,n} \left[-\frac{n(n+1)}{r^2} EL_n - \frac{2im}{r^2} \right] e_{nm}(r) P_n^m(\cos\theta) e^{im\phi} \qquad (A.44)$$

$$+ \frac{2}{r^2} \left(\frac{n(n+1)}{r} - \frac{\partial}{\partial r} \right) f_{nm}(r) \sin\theta \frac{d}{d\theta} P_n^m(\cos\theta) e^{im\phi}$$

$$2\frac{n(n+1)}{r^2} \left(\frac{2}{r} - \frac{\partial}{\partial r} \right) f_{nm}(r) \cos\theta P_n^m(\cos\theta) e^{im\phi}$$

$$= \mathbf{1}_r \cdot \nabla \times \mathbf{F}_m$$

$$\sum_{m,n} \left[\frac{n(n+1)}{r^2} EL_n - \frac{2im}{r^2} \right] L_n f_{nm}(r) P_n^m(\cos\theta) e^{im\phi} \qquad (A.45)$$

$$+ \frac{2}{r^2} \left(\frac{n(n+1)}{r} - \frac{\partial}{\partial r} \right) e_{nm}(r) \sin\theta \frac{d}{d\theta} P_n^m(\cos\theta) e^{im\phi}$$

$$2\frac{n(n+1)}{r^2} \left(\frac{2}{r} - \frac{\partial}{\partial r} \right) e_{nm}(r) \cos\theta P_n^m(\cos\theta) e^{im\phi}$$

$$= \mathbf{1}_r \cdot \nabla \times \nabla \times \mathbf{F}_m,$$

where

$$L_n = \frac{d^2}{dr^2} - \frac{n(n+1)}{r^2}. \qquad (A.46)$$

The coupling in the equations can be calculated by using the recursion relations,

$$\sin\theta \frac{d}{d\theta} P_n^m(\cos\theta) = \frac{n(n-m+1)}{2n+1} P_{n+1}^m(\cos\theta) - \frac{(n+m)(n+1)}{2n+1} P_{n-1}^m(\cos\theta) \quad (A.47)$$

and

$$\cos\theta P_n^m(\cos\theta) = \frac{n-m+1}{2n+1}P_{n+1}^m(\cos\theta) - \frac{n+m}{2n+1}P_{n-1}^m(\cos\theta). \qquad (A.48)$$

see Abramowitz and Stegun (1965). From these relations we find that e_{nm} couples only to $f_{n\pm1,m}$ and that f_{nm} couples only to $e_{n\pm1,m}$, and so the n structure decouples into two symmetry classes, odd n for e and even n for f for the first, and vice versa for the second. Although the symmetry classes are distinct the same procedure is used to solve them. The $2im/r^2$ term makes it convenient to use complex arithmetic for the non-axisymmetric quantities, but this is not necessary for the axisymmetric ($m = 0$) quantities. By treating the radial derivatives arising in the diffusive terms with a Crank-Nicolson scheme the equations (A.41) and (A.42) essentially take the form:

$$\underline{X}\varepsilon = \mathbf{F} \qquad (A.49)$$

where $\underline{X}$ contains the details of the terms on the left hand sides of (A.41) and (A.42), the matrix ε contains the spectral coefficients of e and f for the appropriate symmetry class and $\mathbf{F}$ contains the r components of the first and second curls. The coupling in n leads to a tri-diagonal block banded structure for the two $\underline{X}$ matrices. These must be inverted to obtain the spectral coefficients e and f. The nonlinear terms which are incorporated in $\mathbf{F}$ are obtained using a pseudo-spectral method, which is detailed more fully below, for the magnetic field, $\mathbf{B}$ and temperature, T at a given time step. The matrices $\underline{X}$ do not change from one time step to the next, and so can be precomputed, along with their LU decomposition enabling efficient inversion of the equations at each time step. The LU decomposition and inversion of the matrices is carried out by the NAG routines F01NAF and F04NAF respectively. The boundary conditions are incorporated in the last two rows of each diagonal block for e, and the last four rows of each diagonal block for f. For the no-slip boundary conditions which we exclusively consider, then the condition

$$u_r = u_\theta = u_\phi = 0, \qquad (A.50)$$

124

at $r = r_i, r_o$, for the non-axisymmetric flow, translates to

$$e_{nm}(r) = f_{nm}(r) = \frac{d}{dr} f_{nm}(r) = 0, \tag{A.51}$$

at $r = r_1, r_2$ in the non-dimensional system. Consider now the relation $e_{nm}(r) = 0$ at $r = r_1, r_2$. On substituting the radial expansion as given in (A.30) then we find that

$$\sum_{l=1}^{M2+2} (-1)^l e_{lnm} = \sum_{l=1}^{M2+2} e_{lnm} = 0. \tag{A.52}$$

Thus we see that the boundary conditions are implemented by setting the last two rows of the appropriate block to be $[-1, 1, -1, 1, \ldots]$ and $[1, 1, 1, 1, \ldots]$, and setting the appropriate entries in $\mathbf{F}_m$ to be zero. Note that the inner core rotation is implemented by setting the appropriate entry in the axisymmetric $\mathbf{F}_m$ to be the value given by (A.40) instead of 0.

A.2.1 Pseudo-spectral method

First we have to take the spectral coefficients v, ψ etc., and calculate the real $\mathbf{B}, \mathbf{U}$ and T. Further we then have to calculate not only the nonlinear forcing terms on the right hand side of each equation, but also the r component of their first and second curls. Finally the quantities have to be separated back into the spherical harmonic coefficients required to time step the equations. The separation in ϕ is trivially done analytically, but the separation in r and θ must be included in this method. In fact the pseudo-spectral method involves repeatedly switching back and forth between spectral and real space (Canuto et al 1988). The first stage is to calculate $\mathbf{B}, \mathbf{U}$ and T at certain collocation points in real space, allowing the construction of the nonlinear forcing terms in real space. The curls are performed after transforming back to spectral space, returning the spectral coefficients in the required form for solving/time stepping the equations. One single subroutine can be set up to perform the curls since the terms on the right hand sides of the momentum and induction equations all involve the same operations, namely the r components of the first and second curls of $\mathbf{F}_m$ (and $\mathbf{F}_i$ for

the induction equation). So far only slow transforms have been used to convert from real to spectral space (and back again) because there is little advantage in using fast transforms at our modest truncation levels.

The first stage in the computation is to calculate explicitly what radial and latitudinal structures are required to calculate $\mathbf{B}, \mathbf{U}$ and their curls in real space. By precomputing all these functions at the appropriate collocation points, the evaluation in real space is reduced to simple matrix multiplication. The radial collocation points are taken to be the K zeros of $T_K(x_o)$ and the latitudinal collocation points are taken to be the L zeros of $P_L(\cos\theta)$. All of the angular terms will be exactly dealiased if

$$2L \geq (3LU + 1, LU + 2LB + 1, LU + 2LT + 1), \qquad (A.53)$$

but the r structure will never be exactly dealiased, although if K is chosen to satisfy an inequality similar to (A.53), then the radial structure will essentially be dealiased too (Hollerbach 1999). Each of the components of $\mathbf{F}_{m,i}$ can then be calculated by multiplying the appropriate components of $\mathbf{B}$ and $\mathbf{U}$. Having obtained the forcing terms we need to transform back to spectral space in r and θ, and so we need to know which functions the r, θ and ϕ components will be expanded in. For the radial structure we use Chebyshev polynomials, but for the angular structure we use $P_n^m(\cos\theta)$ for the r component, and $P_n^m(\cos\theta)/\sin\theta$ for the θ and ϕ components for $m \neq 0$ and $P_n^m(\cos\theta)\cdot\sin\theta$ for $m = 0$ (see Hollerbach 1999). By precomputing the functions appearing in the operator $\mathbf{1}_r \cdot \nabla\times$ at the same collocation points as before, allows the calculation of the terms on the left hand side of (A.41) and (A.42) by another matrix multiplication. One final matrix multiplication is required to transform back to spectral space, giving the spectral coefficients of the nonlinear terms. Although we seem to be performing endless matrix multiplications, once we have separated the forcing terms into separate azimuthal modes, the whole complicated procedure as described above, can be performed by just one matrix multiplication for each of the radial and latitudinal

126

structures, since matrix multiplication is associative, giving a very efficient method.

A.3   Induction and heat equations

We again treat the diffusive terms implicitly, with a second order Runge-Kutta method used to treat the time derivatives and a Crank Nicolson scheme employed for the diffusive terms. The remaining nonlinear terms are treated explicitly, and are calculated using a psuedo-spectral method as described above. This gives

$$\mathbf{1}_r \cdot \left[\frac{\partial \mathbf{B}}{\partial t} - \nabla^2 \mathbf{B} \right] = \mathbf{1}_r \cdot [\nabla \times (\mathbf{u} \times \mathbf{B})] \tag{A.54}$$

$$\mathbf{1}_r \cdot \nabla \times \left[\frac{\partial \mathbf{B}}{\partial t} - \nabla^2 \mathbf{B} \right] = \mathbf{1}_r \cdot \nabla \times [\nabla \times (\mathbf{u} \times \mathbf{B})] \tag{A.55}$$

We use the magnetic field $\mathbf{B}$ to illustrate the general time stepping algorithm employed, but the numerical solution of both of these equations is discussed in more detail in Appendix B, as the same method is adopted. The terms on the right hand side must be evaluated twice per time step, with the *predictor* step, giving the spectral coefficients accurate to $O(\delta t)$

$$\frac{\mathbf{B}^{(n+1)} - \mathbf{B}^{(n)}}{\delta t} - \frac{1}{2} \nabla^2 (\mathbf{B}^{(n+1)} + \mathbf{B}^{(n)}) = \mathbf{F}_i^{(n)} \tag{A.56}$$

We use this result in the *corrector* step which gives the spectral coefficients to an accuracy of $O(\delta t^2)$.

$$\frac{\mathbf{B}^{(n+1)} - \mathbf{B}^{(n)}}{\delta t} - \frac{1}{2} \nabla^2 (\mathbf{B}^{(n+1)} + \mathbf{B}^{(n)}) = \frac{1}{2} [\mathbf{F}_i^{(n+1)} + \mathbf{F}_i^{(n)}] \tag{A.57}$$

This algorithm can be very neatly summarised in a matrix system of the following form

$$\underline{X} \mathbf{B}^{(n+1)} = \underline{Y} \mathbf{B}^{(n)} + \delta t \mathbf{F}_i^{(n)} \tag{A.58}$$

i.e.

$$\mathbf{B}^{(n+1)} = \underline{X}^{-1} [\underline{Y} \mathbf{B}^{(n)} + \delta t \mathbf{F}_i^{(n)}] \tag{A.59}$$

where the matrices $\underline{X}^{-1}, \underline{Y}$, and their product $\underline{XY}^{-1}$ can be precomputed. This means that to advance the induction equation at each time step requires only a simple matrix multiplication.

A.3.1 Inner core magnetic field

Since the equation which must be solved in the inner core is just the induction equation it can be time stepped in the same fashion as outlined above. In addition, the nonlinear term on the left hand side is simply

$$\pm im\Omega_i \sum_{l,n} \frac{n(n+1)}{r^2} h_{lmn} \widehat{T}_{l-1}(x_i) P_n^m(\cos\theta) \tag{A.60}$$

for the first curl of the induction equation in the inner core and

$$\pm im\Omega_i \sum_{l,n} \frac{n(n+1)}{r^2} g_{lmn} \widehat{T}_{l-1}(x_i) P_n^m(\cos\theta) \tag{A.61}$$

for the second, meaning that these forcing terms can be calculated by matrix multiplication without using a pseudo-spectral method. Note also that the nonlinear terms in the heat equation can also be calculated without using a pseudo-spectral method.

A.3.2 Adaptive time stepping

The time stepping method detailed above produces two solutions, the *predictor* and *corrector*. For a prescribed value of δt these are $O(\delta t)$ and $O(\delta t^2)$ accurate respectively. The adaptive time stepping method compares the results obtained in these two stages. If the relative difference in any spectral coefficient, ΔT, is greater than a desired tolerance, ΔT_{max}, then the prescribed value of δt is decreased by a factor 2, and the calculation at that time step is repeated for the new value of δt. This process continues either until the required tolerance level is obtained i.e. $\Delta T < \Delta T_{max}$ or the minimum time step value allowed is reached i.e. $\delta t \leq \delta t_{min}$. If $\delta t > \delta t_{min}$, and the tolerance is satisfied, then the calculation continues with δt as time step. The solutions are continually checked, and if $\Delta T < \Delta T_{max}/\omega$, where ω is a safety factor,

for nt consecutive time steps, then the value of δt is increased again. Each of the quantities $\Delta T_{max}, \delta t_{min}, \omega$ and nt are prescribed, along with the default value of the time step δt. This is a very efficient way of tracking solutions with complicated time behaviour. Rather than repeat a whole run at a uniform lower value of δt, the adaptive code will only employ a lower value of δt when required, with the default prescribed value used at other times.

A.4 Diagnostics

We are interested in obtaining the time dependence and morphology of $\mathbf{B}, \mathbf{U}$ and T for each given set of parameters. To enable us to establish when a given solution has settled, and how each quantity is varying in time, then the leading (i.e. $l = 1, n = 1$) spectral coefficients are written out after a given number of time steps. This coefficient should be representative of the full solution. By also making a note of the total number of time steps and multiplying by the time step δt, a plot of the particular coefficient(s) against time can be produced. Using the adaptive time stepping version of the code requires a different calculation method for the time. When each solution is written out, in this case the total time is written out with the other data, since the points in real time may now be unevenly spaced. By calculating and writing the magnetic and fluid energies of the solution at the same time as the spectral coefficients, an idea of the time dependence and magnitude of $\mathbf{B}$ and $\mathbf{U}$ can be obtained, which does not depend on looking at one particular coefficient. The magnetic and fluid energies are defined as follows

$$E_m = \frac{1}{2\mu_0} \int_{V1} \mathbf{B}^2 dV, \quad E_f = \frac{\rho}{2} \int_{V2} \mathbf{U}^2 dV \tag{A.62}$$

where $V1$ represents all space and $V2$ is the volume of the outer core. It is worth commenting on the choice of fluid energy, as opposed to the more normal kinetic energy. The kinetic energy of a system is the work done in bringing that system to rest. If no

129

inertia is acting in the system, then no work is required to bring a body to rest, and so the kinetic energy is 0. We can of course still form the integral, and it should still tell us something about the strength of the fluid flow, however we cannot strictly refer to it as the kinetic energy. The term fluid energy is used in Chapters 3 and 4, but since no such problem exists in a system with inertia, then in Chapter 5, we will talk about the kinetic energy. The integrals in θ and ϕ can be calculated analytically, by using the normalisation of the Legendre polynomials and evaluating the real part of the $e^{im\phi}$ term explicitly in terms of $\cos(m\phi)$ and $\sin(m\phi)$. This leaves a one-dimensional integral in r, which is performed using Gaussian quadrature with 64 nodes. All that remains is to calculate what form the functions of r will take. We will calculate the axisymmetric and non-axisymmetric energies separately, with the poloidal and toroidal parts of each also calculated separately. Additionally the equivalent integrals have to be evaluated for the magnetic field in the inner core, which has a different set of expansion functions.

As an example consider the non-axisymmetric velocity, $\mathbf{u}$, and its toroidal-poloidal decomposition (A.21). Then

$$\mathbf{u} \cdot \mathbf{u} = \tag{A.63}$$

$$\nabla \times (e\mathbf{1}_r) \cdot \nabla \times (e\mathbf{1}_r) + \tag{A.64}$$

$$2(\nabla \times (e\mathbf{1}_r) \cdot \nabla \times \nabla \times (f\mathbf{1}_r)) +$$

$$\nabla \times \nabla \times (f\mathbf{1}_r) \cdot \nabla \times \nabla \times (f\mathbf{1}_r)$$

By expanding these terms fully, the middle cross term will give 0 when integrated over θ due to the combinations of spherical harmonics which appear. The toroidal term can be dealt with by using the vector identity,

$$\nabla \cdot (\mathbf{D} \times \mathbf{E}) = \mathbf{E} \cdot (\nabla \times \mathbf{D}) - \mathbf{D} \cdot (\nabla \times \mathbf{E}) \tag{A.65}$$

twice, and substituting for the expansions to obtain,

$$\nabla \times (e\mathbf{1}_r) \cdot \nabla \times (e\mathbf{1}_r) = \nabla \cdot ((e\mathbf{1}_r) \times \nabla \times (e\mathbf{1}_r)) + e\mathbf{1}_r \cdot \nabla \times \nabla \times (e\mathbf{1}_r). \quad \text{(A.66)}$$

All of the terms which would not contribute to the volume integrals, with the given expansions, have been removed at this stage. A similar expression can be obtained for the poloidal term,

$$\nabla \times \nabla \times (f\mathbf{1}_r) \cdot \nabla \times \nabla \times (f\mathbf{1}_r) = \quad \text{(A.67)}$$

$$\nabla \cdot (\nabla \times (f\mathbf{1}_r) \times \nabla \times \nabla \times (f\mathbf{1}_r)) + f\mathbf{1}_r \cdot \nabla \times \nabla \times \nabla \times \nabla \times (f\mathbf{1}_r).$$

By suitable use of the divergence theorem, the non-axisymmetric part of E_f can be calculated using the following four integrals,

$$\int_{V2} e\mathbf{1}_r \cdot \nabla \times \nabla \times (e\mathbf{1}_r) \, dV, \quad \int_S e\mathbf{1}_r \times \nabla \times (e\mathbf{1}_r) \, dS \quad \text{(A.68)}$$

$$\int_{V2} f\mathbf{1}_r \cdot \nabla \times \nabla \times \nabla \times \nabla \times (f\mathbf{1}_r) \, dV, \quad \int_S \nabla \times (f\mathbf{1}_r) \times \nabla \times \nabla \times (f\mathbf{1}_r) \, dS \quad \text{(A.69)}$$

The corresponding integrals involving the scalars g and h will give the non-axisymmetric part of E_m. However within the code, we do not need to calculate all these integrals explicitly as the boundary conditions require that the surface integrals involving e, g and f do not contribute to the final value of the energy. The integrands can be calculated by constructing the real radial fields in a similar fashion to that used to calculate the nonlinear terms in the main equations, remembering of course that for the magnetic field, $V1$ includes the inner core. Since the axisymmetric quantities can be treated in exactly the same way, then ten integrals are required to evaluate E_m or E_f.

The morphology of the axisymmetric and non-axisymmetric quantities are plotted separately. For the axisymmetric quantities we plot the toroidal magnetic field contours, the poloidal magnetic field lines, the angular velocity contours, the meridional flow streamlines and the temperature contours. The poloidal field lines are obtained

by solving the relation

$$\frac{dr}{\overline{B}_r} = \frac{r\,d\theta}{\overline{B}_\theta} \tag{A.70}$$

which gives

$$Ar\sin\theta = constant, \tag{A.71}$$

and similarly for the meridional streamlines $\psi r \sin\theta$. For the non-axisymmetric quantities the real and imaginary parts of the r, θ and ϕ components of ($\mathbf{b}$ and $\mathbf{u}$) are plotted, giving the solution in two meridional slices $\pi/2$ radians apart. The axisymmetric and non-axisymmetric components of the flow are shown below, with the components of the magnetic field obtained in an analogous way.

$$\overline{U}_r = \frac{1}{r\sin\theta}\left(\frac{\partial}{\partial\theta}\sin\theta\psi\right) \tag{A.72}$$

$$\overline{U}_\theta = -\frac{1}{r}\frac{\partial}{\partial r}(r\psi) \tag{A.73}$$

$$\overline{U}_\phi = v \tag{A.74}$$

$$u_r = \frac{n(n+1)}{r^2}f_{nm}(r)P_n^m(\cos\theta)e^{im\phi} \tag{A.75}$$

$$u_\theta = \left(\frac{im}{r\sin\theta}e_{nm}(r)P_n^m(\cos\theta) + \frac{1}{r}f'_{nm}(r)\frac{d}{d\theta}P_n^m(\cos\theta)\right)e^{im\phi} \tag{A.76}$$

$$u_\phi = \left(\frac{im}{r\sin\theta}f'_{nm}(r)P_n^m(\cos\theta) - \frac{1}{r}e_{nm}(r)\frac{d}{d\theta}P_n^m(\cos\theta)\right)e^{im\phi} \tag{A.77}$$

where f'_{nm} is the radial derivative d/dr.

132

Appendix B

Model 2

B.1　Numerical method

In Model 2 the inertia of both the inner core and the outer core fluid is restored, requiring a different method of numerical solution for the momentum equation. When $Ro \neq 0$, the equation is predictive rather than diagnostic, and the momentum equation must be time stepped to obtain the flow. This leads to two options for the Coriolis force. It can be treated implicity as before, giving a method which is well suited to rapid rotation, or it can be treated as a nonlinear forcing term, which is less suited to dealing with rapid rotation. We have chosen to adopt the latter method for now. In addition the equation governing inner core rotation (2.18) must also be time stepped, since there is now an inertial torque to balance the magnetic and viscous torques on the inner core. The governing equations, as first given in Chapter 2, for Model 2 are as shown below:

$$Ro \left(\partial \mathbf{U}/\partial t + (\mathbf{U} \cdot \nabla)\mathbf{U} \right) + \mathbf{1}_z \times \mathbf{U} = \tag{B.1}$$

$$-\nabla P_R + E\nabla^2 \mathbf{U} + (\nabla \times \mathbf{B}) \times \mathbf{B} + qRaT\mathbf{r}.$$

$$\frac{\partial \mathbf{B}}{\partial t} = \nabla \times (\mathbf{U} \times \mathbf{B}) + \nabla^2 \mathbf{B} \tag{B.2}$$

$$\frac{\partial T}{\partial t} + \mathbf{U} \cdot \nabla T = q\nabla^2 T + \hat{\epsilon} \tag{B.3}$$

$$\nabla \cdot \mathbf{U} = \nabla \cdot \mathbf{B} = 0 \qquad (B.4)$$

with the magnetic field in the inner core having to satisfy the induction equation as described in Appendix A.

Since Model 2 has been derived from a fully $3D$ model, $\mathbf{B}, \mathbf{U}$ and T are not split into separate axisymmetric and non-axisymmetric components, with the axisymmetric quantities treated just like those for any other value of m. The magnetic field $\mathbf{B}$, and flow $\mathbf{U}$ are now decomposed into poloidal and toroidal vectors as shown below:

$$\mathbf{B} = \nabla \times (g\mathbf{1}_r) + \nabla \times \nabla \times (h\mathbf{1}_r) \qquad (B.5)$$

and

$$\mathbf{U} = \nabla \times (e\mathbf{1}_r) + \nabla \times \nabla \times (f\mathbf{1}_r) \qquad (B.6)$$

Each of the scalars, in addition to the temperature T are again expanded using Chebyshev polynomials and spherical harmonics. In the outer core we have

$$e(r,\theta,\phi) = \sum_{k=1}^{KU2}\sum_{l=1}^{LU} e_{kl0}\widehat{T}_{k-1}(x_o)P_l^0(\cos\theta) + \sum_{k=1}^{KU2}\sum_{l=m}^{LU} e_{klm}\widehat{T}_{k-1}(x_o)P_l^m(\cos\theta)e^{im\phi} \quad (B.7)$$

$$f(r,\theta,\phi) = \sum_{k=1}^{KU4}\sum_{l=1}^{LU} f_{kl0}\widehat{T}_{k-1}(x_o)P_l^0(\cos\theta) + \sum_{k=1}^{KU4}\sum_{l=m}^{LU} f_{klm}\widehat{T}_{k-1}(x_o)P_l^m(\cos\theta)e^{im\phi} \quad (B.8)$$

$$g(r,\theta,\phi) = \sum_{k=1}^{KB2}\sum_{l=1}^{LB} g_{kl0}\widehat{T}_{k-1}(x_o)P_l^0(\cos\theta) + \sum_{k=1}^{KB2}\sum_{l=m}^{LB} g_{klm}\widehat{T}_{k-1}(x_o)P_l^m(\cos\theta)e^{im\phi} \quad (B.9)$$

$$h(r,\theta,\phi) = \sum_{k=1}^{KB2}\sum_{l=1}^{LB} h_{kl0}\widehat{T}_{k-1}(x_o)P_l^0(\cos\theta) + \sum_{k=1}^{KB2}\sum_{l=m}^{LB} h_{klm}\widehat{T}_{k-1}(x_o)P_l^m(\cos\theta)e^{im\phi}$$
$$(B.10)$$

$$T(r,\theta,\phi) = \sum_{k=1}^{KT2}\sum_{l=1}^{LT} \Theta_{kl0}\widehat{T}_{k-1}(x_o)P_l^0(\cos\theta) + \sum_{k=1}^{KT2}\sum_{l=m}^{LT} \Theta_{klm}\widehat{T}_{k-1}(x_o)P_l^m(\cos\theta)e^{im\phi}$$
$$(B.11)$$

with x_o defined as before. There are several points which are worthy of comment. Firstly the truncations for each of the flow, magnetic field and temperature can be set to different values, and we take advantage of this for the calculations performed in Chapter 5. The radial truncation $K*2/4$, where $*$ represents B, U or T, allows for $K*$ Chebyshev polynomials which give the radial structure of the solution in the outer core, plus two/four extra coefficients which are used to satisfy the boundary conditions. We will return to the boundary conditions when the individual equations are discussed in more detail. The latitudinal truncation for the spherical harmonics is given by the integers denoted by $L*$. Note that there is now no symmetry constraint imposed for the spherical harmonic degrees l. For the scalars e, f, g and h, the more natural Legendre polynomials are now used, but the $l = m = 0$ mode has been excluded, since it will not contribute when substituted back into equations (B.5) and (B.6). However this mode is included for the scalar temperature T, where we have used Θ to denote the spectral coefficient. The expansions for the non-axisymmetric terms have been written in complex form purely for convenience of notation. Within the code these quantities are explicitly separated into coefficients of $\cos(m\phi)$ and $\sin(m\phi)$, and so at no stage is complex arithmetic employed. This has the effect of making the code longer, especially since the nonlinear interactions between different azimuthal modes are being calculated analytically, but also making it run faster. When the finitely conducting inner core is added to the code then g and h are expanded there as follows

$$
g(r, \theta, \phi) = \sum_{k=1}^{KBI1} \sum_{l=1}^{LB} gi_{kl0} \widehat{T}_{2k-1}(x_i) r^n P_l^0(\cos\theta) + \sum_{k=1}^{KBI1} \sum_{l=m}^{LB} gi_{klm} \widehat{T}_{2k-1}(x_i) r^n P_l^m(\cos\theta) e^{im\phi}
$$

(B.12)

$$
h(r, \theta, \phi) = \sum_{k=1}^{KBI1} \sum_{l=1}^{LB} hi_{kl0} \widehat{T}_{2k-1}(x_i) r^n P_l^0(\cos\theta) + \sum_{k=1}^{KBI1} \sum_{l=m}^{LB} hi_{klm} \widehat{T}_{2k-1}(x_i) r^n P_l^m(\cos\theta) e^{im\phi}
$$

(B.13)

where x_i is as defined before. Notice that the radial expansions are slightly different to those for Model 1. Let the radial function for gi be $\widehat{g}_{lm}(r)$. There are two conditions

that $\widehat{g}_{lm}(r)$ (or equivalently $\widehat{h}_{lm}(r)$) must satisfy. Close to the origin $\widehat{g}_{lm}(r)$ must tend to zero at least as quickly as r^2 for the even modes and r^3 for the odd modes. Additionally the following condition for the radial symmetry must be satisfied

$$\widehat{g}_{lm}(-r) = (-1)^{l+1}\widehat{g}_{lm}(r). \tag{B.14}$$

These conditions will be satisfied if $n = 1$ for odd l and $n = 2$ for even l in (B.12) and (B.13). The radial truncation in this case is $KBI = KB/2$, with one extra coefficient included to satisfy the matching condition at the ICB.

B.2 Momentum equation

As in Model 1 the viscous term is shifted to the left hand side, but the Coriolis force is in this case shifted to the right hand side and so is dealt with explicitly. This method places a lower limit on the values of Ro which can be prescribed. The notation in this section is given with a summation over m, simply for ease of presentation. Wherever summation over m is displayed or implied, the 'sum' should be thought of as $m = 0$ plus one other non-zero value of m. We again consider the r component of the first and second curls of the momentum equation, giving,

$$\sum_{m,l} \frac{l(l+1)}{r^2} \left[Ro\frac{\partial}{\partial t} - EL_l \right] e_{lm}(r)P_l^m(\cos\theta)e^{im\phi} = \mathbf{1}_r \cdot \nabla \times \mathbf{F}_m \tag{B.15}$$

$$-\sum_{m,l} \frac{l(l+1)}{r^2} \left[Ro\frac{\partial}{\partial t} - EL_l \right] L_l f_{lm}(r)P_l^m(\cos\theta)e^{im\phi} = \mathbf{1}_r \cdot \nabla \times \nabla \times \mathbf{F}_m \tag{B.16}$$

where the operator

$$L_l = \frac{\partial^2}{\partial r^2} - \frac{l(l+1)}{r^2}, \tag{B.17}$$

and

$$\mathbf{F}_m = -\mathbf{1}_z \times \mathbf{U} - Ro(\mathbf{U} \cdot \nabla)\mathbf{U} + (\nabla \times \mathbf{B}) \times \mathbf{B} + qRaT\mathbf{r}. \tag{B.18}$$

136

By noting that

$$(\mathbf{U} \cdot \nabla)\mathbf{U} = \nabla(|\mathbf{U}|^2/2) - \mathbf{U} \times (\nabla \times \mathbf{U}), \tag{B.19}$$

and that the $\nabla(|\mathbf{U}|^2/2)$ term will be eliminated by the curls anyway, then the forcing actually calculated is

$$\mathbf{F}_m = -\mathbf{1}_z \times \mathbf{U} - Ro(\nabla \times \mathbf{U}) \times \mathbf{U} + (\nabla \times \mathbf{B}) \times \mathbf{B} + qRaT\mathbf{r}. \tag{B.20}$$

The calculation of the terms in $\mathbf{F}_m$, the r components of their curls and the separation into spherical harmonic components is done using the pseudo-spectral method as discussed in Appendix A. By separating into different spherical harmonics, the equations (B.15) and (B.16) can be treated independently for each m and each l, as well as independently of each other, since the Coriolis force is now included in the forcing. Let us now consider time stepping the equation (B.15), where the notation

$$e_{lm}(r) = \sum_{k=1}^{KU2} e_{klm}\widehat{T}_{k-1}(x_o), \tag{B.21}$$

is again introduced for ease of presentation. The equation is enforced at KU collocation points, which are taken to be the zeros of $\widehat{T}_{KU}(x_o)$, and the two boundary conditions give the required $KU2$ conditions on the spectral coefficients e_{klm}. The collocation points are chosen so that resolution is automatically concentrated close to the boundaries. A second order Runge-Kutta method, which is modified to treat the diffusive terms implicitly, is used to advance the coefficients from one time step to the next. This is done in a two stage process which involves calculating the forcing terms twice. The numerical method has reduced the initial partial differential equation to a matrix equation, which uses the spectral coefficients at time step n to evaluate the spectral coefficients at time step $n + 1$. Implementing these algorithms gives

$$Ro\left(\frac{e_{klm}^{n+1} - e_{klm}^n}{\delta t}\right) - EL_l\left(\zeta e_{klm}^{n+1} + (1 - \zeta)e_{klm}^n\right), \tag{B.22}$$

137

for the left hand side of (B.15), with ζ usually taking the value 0.5 to weight the known and unknown coefficients equally. For the equation which arises for f, a different value has to be adopted if no-slip boundary conditions are to be used, because the algorithm is unstable even for very small time steps. Since treating the diffusive terms implicitly was designed to improve the stability of the scheme, then increasing the weight of the unknown coefficients may rectify the problem. It transpires that in this case adopting $\zeta = 0.6$ is sufficient to stabilise the procedure, but at the cost of degraded accuracy. With $\zeta = 0.5$ the procedure is $O(\delta t^2)$ accurate, but with any other value of ζ the procedure is only $O(\delta t)$ accurate with respect to the diffusive terms. However, even for this first order procedure a reasonable time step gives quite good accuracy, as can be seen from the free decay results. Additionally, since the diffusive (viscous) time scale is likely to be one of the longest time scales in the model, and δt must be shorter than the shortest time scale in the model, then the first order procedure will give very good accuracy.

The first stage of the calculation is the *predictor* stage, which evaluates the forcing terms at the collocation points using the spectral coefficients at time step n, with an initial estimate of the new coefficients $\tilde{e}_{klm}^{n+1}$ obtained by inverting the resultant matrix equation. These new coefficients are used in the *Corrector* stage to again evaluate the forcing terms, and obtain the final coefficients e_{klm}^{n+1}. This whole procedure can be very neatly summarised in two matrix equations, where the $\sim$ denotes the terms associated with the Predictor stage.

$$\underline{X}\tilde{e}^{n+1} = \underline{Y}e^n + \delta t\tilde{\mathbf{F}} \qquad (B.23)$$

$$\underline{X}e^{n+1} = \underline{Y}e^n + \frac{\delta t}{2}\left(\tilde{\mathbf{F}} + \mathbf{F}\right) \qquad (B.24)$$

138

where

$$\mathbf{e}^n = [e^n_{1,lm}, e^n_{2,lm}, \dots, e^n_{KU2,lm}]^T, \tag{B.25}$$

$$\mathbf{F} = [F_1, F_2, \dots, F_{KU}, 0, 0]^T \tag{B.26}$$

and each entry F_k represents $\mathbf{1}_r \cdot \nabla \times \mathbf{F}_m$ at collocation point k. The first KU rows of the matrices $\mathbf{X}$ and $\mathbf{Y}$ are given by the following relations

$$\mathbf{X}_{jk} = \frac{l(l+1)}{r_j^2} [Ro - 0.5\delta t EL_l] \widehat{T}_{k-1}(x)|_{x=x_j} \tag{B.27}$$

$$\mathbf{Y}_{jk} = \frac{l(l+1)}{r_j^2} [Ro + 0.5\delta t EL_l] \widehat{T}_{k-1}(x)|_{x=x_j}, \tag{B.28}$$

with the last two rows of $\underline{X}$ implementing the boundary conditions and the last two rows of $\underline{Y}$ being zero. As before all of these matrices can be precomputed allowing a very efficient time stepping procedure. Adopting the same procedure for the more complicated equation (B.16) gives a similar matrix system with in this case

$$\mathbf{X}_{jk} = -\frac{l(l+1)}{r_j^2} [Ro - 0.6\delta t EL_l] L_l \widehat{T}_{k-1}(x)|_{x=x_j} \tag{B.29}$$

$$\mathbf{Y}_{jk} = -\frac{l(l+1)}{r_j^2} [Ro + 0.4\delta t EL_l] L_l \widehat{T}_{k-1}(x)|_{x=x_j}, \tag{B.30}$$

and the last four rows of $\underline{X}$ implementing the boundary conditions and the last four rows of $\underline{Y}$ being zero. The boundary conditions are incorporated almost exactly as described in Appendix A, but the inhomogeneous boundary condition on $\mathbf{U}$ at the ICB now reduces to

$$e_{KU+1,10} = \Omega_i r_1^2. \tag{B.31}$$

As an added consequence the viscous torque on the ICB will only depend on $e_{10}(r)$.

B.3 Induction equation

By treating the induction equation in a similar manner to that described in Appendix A and substituting for (B.9) and (B.10) we obtain

$$\sum_{m,l} \frac{l(l+1)}{r^2} \left[\frac{\partial}{\partial t} - L_l \right] h_{lm}(r) P_l^m(\cos\theta) e^{im\phi} = \mathbf{1}_r \cdot \nabla \times (\mathbf{U} \times \mathbf{B}) \tag{B.32}$$

$$\sum_{m,l} \frac{l(l+1)}{r^2} \left[\frac{\partial}{\partial t} - L_l \right] g_{lm}(r) P_l^m(\cos\theta) e^{im\phi} = \mathbf{1}_r \cdot \nabla \times \nabla \times (\mathbf{U} \times \mathbf{B}). \tag{B.33}$$

It is immediately obvious that these equations have an identical format to (B.15), and so can be time stepped in exactly the same way. The nonlinear terms on the right hand side are again obtained using a pseudo-spectral method. We now turn to the boundary conditions, and begin by examining the case of electrically insulating boundary conditions at *both* the ICB and CMB. Matching to potential fields in the regions $r < r_1$ and $r > r_2$ then yields the boundary conditions

$$g_{lm}(r) = \left(\frac{d}{dr} - \frac{l+1}{r} \right) h_{lm}(r) = 0, \tag{B.34}$$

at $r = r_1$ and

$$g_{lm}(r) = \left(\frac{d}{dr} + \frac{l}{r} \right) h_{lm}(r) = 0, \tag{B.35}$$

at $r = r_2$. The actual entries in the appropriate rows of the $\underline{X}$ matrices will be slightly more complicated than for the flow, but nevertheless the boundary conditions can be implemented exactly as before. In fact because the boundary conditions do not involve m, the same $\underline{X}$ matrices can be precomputed and re-used for each value of m as well as at each time step.

As we have already stated, a finitely conducting inner core cannot be implemented simply by imposing a boundary condition at $r = r_1$, we must also solve for the magnetic field in the inner core. The equations which must be solved in the inner core are

$$\sum_{m,l} \frac{l(l+1)}{r^2} \left[\frac{\partial}{\partial t} - \Sigma^{-1} L_l \right] \widehat{h}_{lm}(r) P_l^m(\cos\theta) e^{im\phi} = \mathbf{1}_r \cdot \nabla \times (\mathbf{U} \times \mathbf{B}) \tag{B.36}$$

140

$$\sum_{m,l} \frac{l(l+1)}{r^2} \left[\frac{\partial}{\partial t} - \Sigma^{-1} L_l \right] \widehat{g}_{lm}(r) P_l^m(\cos\theta) e^{im\phi} = \mathbf{1}_r \cdot \nabla \times \nabla \times (\mathbf{U} \times \mathbf{B}), \qquad \text{(B.37)}$$

where Σ is the ratio of the inner core to outer core conductivity, and $\mathbf{U} = \Omega_i r \sin\theta \mathbf{1}_\phi$ is purely the solid body rotation of the inner core. The equations (B.36) and (B.37) are enforced at KBI collocation points, given by the zeros of $\widehat{T}_{2KBI+1}(x_i)$ on (0,1). This is slightly more difficult to implement, but since each l is dealt with separately then only a minor change is required to the precomputation of the $\underline{X}$ matrices. Rather than boundary conditions at $r = r_1$, we now impose the matching conditions

$$h_{lm}(r) = \widehat{h}_{lm}(r), \frac{d}{dr} h_{lm}(r) = \frac{d}{dr} \widehat{h}_{lm}(r) \qquad \text{(B.38)}$$

$$g_{lm}(r) = \widehat{g}_{lm}(r), \frac{d}{dr} g_{lm}(r) = \frac{d}{dr} \Sigma^{-1} \widehat{g}_{lm}(r), \qquad \text{(B.39)}$$

which are only valid for no-slip boundary conditions. These represent the continuity of the three components of the magnetic field, and the tangential components of the associated electric field. Once again the resultant $\underline{X}$ matrices do not depend on m and so can be reused as before. These $\underline{X}$ matrices have a structure which allows the simultaneous implementation of the equations in the outer and inner cores, the matching conditions and the boundary condition at the CMB (see Hollerbach 1999).

Additionally we have to time step the equation (2.18). Implementing a similar algorithm on this equation gives

$$\Omega_i^{n+1} = \Omega_i^n + (\Gamma_C^n + \tilde{\Gamma}_C^{n+1}) \qquad \text{(B.40)}$$

where $\Gamma_C = \Gamma/C$. It is this value of Ω_i which is input to the inhomogeneous boundary condition on $e_{10}(r)$.

B.4   Heat equation

By substituting (B.11) into the heat equation, we obtain

$$\sum_{m,l} \left[\frac{\partial}{\partial t} - q(L_l + \frac{2}{r} \frac{\partial}{\partial r}) \right] \Theta_{lm}(r) P_l^m(\cos\theta) e^{im\phi} = -\mathbf{U} \cdot \nabla T. \qquad \text{(B.41)}$$

141

This equation can be time stepped using a similar method to that used for the other scalar equations, with the boundary conditions

$$\Theta_{lm}(r) = 0, \tag{B.42}$$

at $r = r_1, r_2$ implemented in exactly the same way.

B.5   Testing of the code

B.5.1   The $2\frac{1}{2}D$ approximation

By employing this approach, the only major change to the code occurs in the calculation of the nonlinear terms, and so this has to be thoroughly tested. Even although only minor changes have to be made to the time stepping routines, these are still tested by obtaining the free decay rates for the equations involving each of the scalars e, f, g, h and Θ.

Analytic testing of the calculation of the nonlinear terms

Calculation of the nonlinear terms from each equation is a two stage process. First the real variables $\mathbf{B}, \mathbf{U}$ and T have to be calculated and combined in the appropriate way, and then the r component of the first and second curls is taken. This whole process is performed within one large subroutine in the code, with a single subroutine within this one to deal with the curls. The main difference lies in the calculation of the nonlinear terms which is done by the same pseudo-spectral method in r and θ, but the azimuthal interactions are calculated analytically. As an example of how this is done consider an interaction between the scalars e and f given in (B.7 and B.8), a similar interaction arises in the calculation of $(\nabla \times \mathbf{U}) \times \mathbf{U}$. The interaction produces four products; the two axisymmetric ($m = 0$) parts combine to produce an axisymmetric term, two non-axisymmetric terms are produced by the interaction of the non-axisymmetric ($e^{im\phi}$) part of e and the axisymmetric part of f and vice versa. There

142

is also the product of the two non-axisymmetric parts, which produces an axisymmetric term and a non-axisymmetric ($e^{i2m\phi}$) term. The former term is included along with the other axisymmetric product but the latter term is excluded, since only one azimuthal wavenumber m is included.

The ultimate test of course is to compare the output from the $2\frac{1}{2}D$ code with a suitably truncated $3D$ model, and this has been done and is discussed later in Section B.4.3. To test the analytic separation into azimuthal modes, requires that simple functions are prescribed for the scalars e, f, g, h and Θ. A symbolic computing package (Maple) is then used to calculate the required nonlinear forcing terms and the r component of their first and second curls. Both the prescribed analytic functions and the solution obtained must be converted to spectral coefficient expansions as this is what is input and output from the code. As an example let

$$e(r, \theta, \phi) = r \cos \theta = r P_1^0, \qquad (B.43)$$

then $e_{110} = 1, e_{210} = 1/2$ and $e_{klm} = 0$ for all other values of k, l and m. Examples were chosen with purely axisymmetric interactions, purely non-axisymmetric interactions and a mixture of the two. A total of seven analytic examples were tested, each of which produced exact agreement between the code and the output from Maple.

Testing removal of the azimuthal collocation points

One of the analytic examples was also used as input for the $2\frac{1}{2}D$ code and the $3D$ code to compare the output. The major difference between the two approaches is that the $2\frac{1}{2}D$ code calculates analytically to which azimuthal mode the nonlinear terms belong, whereas the $3D$ code uses a collocation method to construct the ϕ structure, and relies on a slow Fourier transform to separate out the different azimuthal modes. It is clearly important to test that this change has been made consistently. The solution will be

exactly dealiased if

$$2MN \geq max(3MU + 1, MU + 2MB + 1, MU + 2MT + 1) \qquad \text{(B.44)}$$

where MN represents the number of azimuthal collocation points, and MU, MB and MT give the azimuthal truncation for the flow, magnetic field and temperature. So for the case $MU = MB = MT = 2$, the number of collocation points, $MN \geq 4$. The calculation was repeated for $MN = 16, 8, 4$. It was found that even for $MN = 4$, the same solution was obtained using both the $2\frac{1}{2}D$ code and the $3D$ code. With agreement to at worst 9 or 10 decimal places, giving confidence that our $2\frac{1}{2}D$ approach has been correctly implemented.

B.5.2 Testing of the time stepping

This is done by obtaining the free decay rates for each of the five equations used to obtain the spectral coefficients. Implementation in the code requires that the forcing terms for each of the equations are 0. The free decay rates are independent of m, which means that an axisymmetric case can be chosen, with an arbitrary function of r chosen as initial conditions. A value of l is chosen, and the solution is time stepped until the decay rate has settled. Initial results are given with an insulating inner core.

The equations governing the scalars e, g and h can be solved analytically to obtain the free decay rates. Each of the equations (B.15, B.32 and B.33) takes the form

$$\frac{d\varphi}{dt} - L\varphi = 0, \qquad \text{(B.45)}$$

where $\varphi = \varphi(r, t)$ represents one of e, g, h and $L = L_l$. The solutions can be shown to be of the form,

$$\varphi(r, t) = e^{-\lambda^2 t}[Arj_l(\lambda r) + Bry_l(\lambda r)] \qquad \text{(B.46)}$$

where j_l and y_l are spherical Bessel functions of the first and second kind respectively (see Abramowitz and Stegun 1965), and A and B are arbitrary constants. The different boundary conditions determine the exact value for λ.

For (B.15) and (B.33) the boundary conditions are $e = g = 0$ at $r = r_1, r_2$, and so the decay rates, for a given l, can be obtained from the following relation,

$$j_l(\lambda/2)y_l(3\lambda/2) - j_l(3\lambda/2)y_l(\lambda/2) = 0 \qquad (B.47)$$

since $r_1 = 1/2$ and $r_2 = 3/2$. For (B.32), the boundary conditions are,

$$r = r_1 : \frac{dh}{dr} - \frac{(l+1)h}{r} = 0, \qquad r = r_2 : \frac{dh}{dr} + \frac{lh}{r} = 0 \qquad (B.48)$$

giving the more complicated relation,

$$[\lambda/2 j_l'(\lambda/2) - l j_l(\lambda/2)] \, [3\lambda/2 y_l'(3\lambda/2) + (l+1)y_l(3\lambda/2)] - \qquad (B.49)$$

$$[\lambda/2 y_l'(\lambda/2) - l y_l(\lambda/2)] \, [3\lambda/2 j_l'(3\lambda/2) + (l+1)j_l(3\lambda/2)] = 0$$

The equation (B.16) is much harder to solve analytically, in this case two 4×4 determinants have to be solved rather than just one 2×2 determinant. The analytic values for $l = 1 \ldots 4$ are taken from Hollerbach (1999).

The free decay rate can be calculated analytically for the heat equation by solving,

$$\frac{d\varphi}{dt} - L\varphi - \frac{2}{r}\frac{d\varphi}{dr} = 0 \qquad (B.50)$$

The solutions can be shown to be of the form,

$$\varphi(r, t) = e^{-\lambda^2 t}[A j_l(\lambda r) + B y_l(\lambda r)] \qquad (B.51)$$

where j_l and y_l are again spherical Bessel functions of the first and second kind respectively, and A and B are arbitrary constants. The boundary conditions are $\Theta = 0$ at $r = r_1, r_2$, giving rise to the same relation as (B.46), and so the same analytical values of λ are obtained as for e and g.

Table B.1: The analytically calculated free decay rates with an insulating inner core and no-slip boundary conditions.

	$l = 0$	$l = 1$	$l = 2$	$l = 3$	$l = 4$
e, g	–	12.07101109	16.33228462	22.41275078	30.04580136
f	–	37.6096886	36.5341303	38.3227479	43.3706793
h	–	4.44750953	9.00507099	14.77623480	21.70742406
Θ	9.869604401	12.07101109	16.33228462	22.41275078	30.04580136

By scaling the coefficients at a given time step by the value at the previous time step and writing out the values to a file, it is easy to see when the decay rate has settled to a steady value. By examining the final two values of the coefficients output by the code, and recording the ratio g_n/g_{n+1}, then the value of the decay rate can be calculated using the following relation

$$\lambda^2 = \log_e\left(\frac{g_n}{g_{n+1}}\right)/\delta t. \tag{B.52}$$

Although the specific coefficient g has been used here, the decay rates for the other coefficients are obtained in the same way. Table B.2 gives the values of λ^2 obtained with the code relative to the analytically derived values, obtained with $\delta t = 1 \times 10^{-4}$, for $l = 1$ and $l = 2$. The calculations are then obtained with a different weighting, apart from f which already has $\zeta = 0.6$. Notice that this very neatly confirms our belief that with $\zeta = 0.5$ the solution is $O(\delta t^2)$ accurate, but with any other value it is only $O(\delta t)$ accurate.

Table B.2: The relative free decay rates obtained with the code using an insulating inner core and no-slip boundary conditions.

	$l = 0$	$l = 1$	$l = 2$	$l = 1, \zeta = 0.6$	$l = 2, \zeta = 0.6$
e, g	–	1.000000121	1.000000222	0.999879237	0.999836845
f	–	0.9996251	0.9996359	0.9996251	0.9996359
h	–	1.000000016	1.000000068	0.999955345	0.99991049
Θ	0.999901162	1.000000121	1.000000222	0.999879237	0.999836845

When the finitely conducting inner core is introduced, then the boundary conditions governing g and h, and hence the observed free decay rates will change, and so the tests are repeated, with the results given in (B.5.4).

B.5.3 Comparison of $2\frac{1}{2}D$ and $3D$ codes

Once the above has been completed and satisfactorily tested, then the code can be used to try and obtain some results. We have already performed significant parameter surveys using Model 1, and so would want to use some of these results as initial conditions. Unfortunately different expansions are used in the two different numerical schemes, and so a method for transforming between the two sets of spectral coefficients is required. The starting point is a set of spectral coefficients as described in Appendix A, and the transformation involves a three stage process. In Model 1 dipolar symmetry is imposed, by only including certain degrees of spherical harmonics. Since Model 2 has no imposed symmetry, then the set of spectral coefficients must be modified to reflect this. In practice all that is required is to double the values of $N1$ and $N2$ making the coefficients associated with the harmonic degrees which were previously excluded identically zero. The main work is now over for the non-axisymmetric coefficients, since the expansions are identical in the outer core, and only slightly different in the inner core. Note that since we are still running with an insulating inner core, then the inner core coefficients are not required here. All that remains to be done is to convert the complex coefficients to real notation, remembering that the real part of the complex coefficient is associated with $\cos(m\phi)$, and the imaginary part is associated with $-\sin(m\phi)$. Unfortunately things are not so straightforward for the axisymmetric quantities, which are expanded in terms of different poloidal and toroidal scalars, and in terms of different spherical harmonics. This can be overcome by calculating the real axisymmetric magnetic field, flow and temperature at a set of collocation points. These real quantities can then be converted back into spectral coefficients appropriate for Model 2, by carrying out the inverse operations to those used for constructing the real quantities, ensuring that the truncation and collocation points used are identical. Exactly the same procedure, with the appropriate expansions, can also be used for the

147

inner core quantities. It is relatively simple to check that this method is correct by plotting the relevant quantities and comparing the morphology and magnitude.

Using a steady solution which was obtained at small χ as the initial condition, the new $2\frac{1}{2}D$ code was compared to the existing $3D$ code with insulating inner core. The parameters for the test run were $Ro = 10^{-4}, E = 10^{-3}, q = 10, Ra = 80, \chi = 0.05, m = 2$, and a comparison of the performance is given in Table B.3 below. Excellent agreement was found between the results, with the leading coefficients agreeing to at least 8 decimal places.

Table B.3: Comparison of the performance of the $2\frac{1}{2}D$ and $3D$ codes.

	$2\frac{1}{2}D$	$3D$
Run Time (Hours)	6.78	12.31
Time for 1 time scale	67.78	123.11
Storage (input) MB	4.80	6.00
Storage (output) MB	0.23	0.34
Processor time	94 %	99 %

B.5.4   The inclusion of a finitely conducting inner core

As we have already seen, the induction equation now has to be time stepped to obtain the magnetic field in the inner core, and the inner core will be free to rotate due to the strong magnetic torque on the ICB, requiring that we also time step equation (2.18) to obtain the inner core rotation rate. This means that we have to test, the routine set up to time step Ω_i, the routine which calculates the viscous and magnetic torques as given by (2.19), the routine to calculate the nonlinear forcing terms and the time stepping of the induction equation. The calculation of the torques and the nonlinear forcing terms can be easily tested by inputting simple analytic examples as used to test the $2\frac{1}{2}D$ approximation. To test the time stepping of the inner core rotation rate, we force the outer core fluid to undergo solid body rotation, setting $g = h = f = \Theta = 0$. With this prescription for e the viscous torque at the ICB will be identically zero and so the

148

inner core should maintain exactly the same solid body rotation. We obtained some free decay results for $l = 5$ and $\delta t = 1 \times 10^{-6}$ to test the time stepping of the induction equation. Again the values shown in Table B.4 are relative to the analytically obtained values, and the results give exact agreement with the results presented in Hollerbach (1999).

Table B.4: The relative free decay rates obtained with the code using a finitely conducting inner core and no-slip boundary conditions.

KB	$g, \Sigma = 0.1$	$h, \Sigma = 0.1$	$g, \Sigma = 10$	$h, \Sigma = 10$
8	1.0000001	1.0000016	–	–
10	–	–	1.0005254	1.0002015
12	1.0000000	1.0000000	–	–
14	1.0000000	1.0000000	0.9999995	1.0000014
16	1.0000000	1.0000000	–	–

B.6 Diagnostics

In terms of the plotting of solutions the diagnostics which we use are similar to those used for Model 1. The magnetic and kinetic energies are calculated in the code by a similar method, although clearly the same routines can now be used for the axisymmetric and non-axisymmetric energy. As another test of both the implementation of the these routines in the code, and our transformation method, we calculate the various energy terms with the original coefficients in Model 1, and compare with the same energy terms obtained by substituting the transformed coefficients into Model 2. The values obtained show good agreement giving added confidence in the transformation method, and providing a valid test of the implementation of the routines to calculate the energy terms.

It is somewhat simpler in this case to calculate some of the forces in the momentum equation, to give some idea of the leading order balance in the equations. The Lorentz force, the Coriolis force and the buoyancy force are already calculated by the code,

but we would also like to calculate the viscous and inertial forces. Using the vector identity,

$$\nabla \times (\nabla \times \mathbf{U}) = \nabla(\nabla \cdot \mathbf{U}) - \nabla^2 \mathbf{U}, \tag{B.53}$$

we can calculate $\nabla \times (\nabla \times \mathbf{U})$ instead of $\nabla^2 \mathbf{U}$ for the viscous force, since $\nabla \cdot \mathbf{U} = 0$. This involves a much shorter calculation than is required for $\nabla^2 \mathbf{U}$, and in any case we have already calculated the components of this vector, when setting up the energy routines. The velocity $\mathbf{U}$ is also calculated during the normal calculation of the code. By obtaining the value of $\mathbf{U}$ at consecutive time steps, then the inertial term $\partial \mathbf{U}/\partial t$ can be approximated by

$$\frac{\partial \mathbf{U}}{\partial t} = \frac{\mathbf{U}^{n+1} - \mathbf{U}^n}{\delta t} \tag{B.54}$$

where δt is the value of the time step. Our method is then as follows, we take the solution, in terms of the spectral coefficients, and calculate the r, θ and ϕ components of each of the given forces at two points, one inside the tangent cylinder and one outside the tangent cylinder, for an arbitrary value of ϕ. The point inside the tangent cylinder has spherical coordinates $r \approx 1$, remembering that $r_o = 3/2$, and $\theta \approx \pi/10$, while the point outside the tangent cylinder also has $r \approx 1$ and $\theta \approx \pi/5$. To remain inside the tangent cylinder at this radius requires $\theta \lesssim \pi/6$. This calculation is repeated for the solution at the very next time step, allowing the calculation of $\partial \mathbf{U}/\partial t$. Once the components of these forces have been obtained, the corresponding torques about the z-axis can be calculated. In particular we are interested in obtaining the z-component of the axisymmetric torques, which have the form,

$$F_\phi \, r \sin \theta, \tag{B.55}$$

where F_ϕ represents the azimuthal component of the given axisymmetric force. Since the axisymmetric pressure gradient ($\partial P/\partial \phi = 0$), which we do not calculate anyway,

and the buoyancy, do not have a ϕ-component, then the full balance in the axisymmetric momentum equation can now be examined. Note that the $(\mathbf{U} \cdot \nabla)\mathbf{U}$ part of the axisymmetric inertial term can now be obtained by evaluating $(\nabla \times \mathbf{U}) \times \mathbf{U}$, which is also calculated in the routine operation of the main code, since the $\nabla(\mathbf{U}^2/2)$ term does not contribute to the ϕ-component of the axisymmetric force.

Appendix C

Derivation of T_0 and β

Let us return to the dimensional heat equation (2.3) and consider the unperturbed state for which $\mathbf{U} = 0$ and $T = T_0$, then the equation becomes

$$\kappa \nabla^2 T_0 = -\epsilon \tag{C.1}$$

We now make the suppositions that the volumetric heat source ($\epsilon = $ const.) and that T_0 depends only on r, so that

$$T_0 = -\frac{\epsilon r^2}{6\kappa} - \frac{A}{r} + B \tag{C.2}$$

If we were working in a full sphere then A would automatically take the value 0 to maintain a finite T as $r \to 0$. However we are concerned only with T in the outer core. The temperature remains fixed at both the inner and outer boundaries and so B is an arbitrary constant chosen to give specific values of the temperature at the inner and outer boundaries. Throughout this study we shall assume, without loss of generality, that $B = 0$. By setting $A = 0$, the heating must arise totally from internal sources, whereas by setting $\epsilon = 0$ we assume that the heating is due solely to differential heating at the boundaries. Our implementation requires that we do not choose specific values of A and ϵ, but instead specify the non-dimensional unperturbed temperature profile T_0, appropriate for either of the above cases.

C.1 Internal heating

With $A = 0$ then (C.2) becomes

$$T_0 = -\frac{\epsilon r^2}{6\kappa} \qquad (C.3)$$

It seems sensible to non-dimensionalise the temperature using this unperturbed temperature profile. The temperature scale $\theta = \beta L$, where $\beta = \Delta T_0/L$, the difference in temperature across the shell, scaled by the gap width. In what follows a subscript $*$ represents a non-dimensional quantity, r_1 is the non-dimensional inner core radius, r_2 is the non-dimensional outer core radius, T_1 is the non-dimensional temperature at the ICB and T_2 is the non-dimensional temperature at the CMB. Under the non-dimensionalisation (C.3) becomes

$$\theta T_{0*} = -\frac{\epsilon L^2}{6\kappa} r_*^2 \qquad (C.4)$$

so,

$$T_{0*} = -\frac{\epsilon L^2}{6\kappa\theta} r_*^2 = -\frac{\epsilon L}{6\kappa\beta} r_*^2 \qquad (C.5)$$

For a sensible non-dimensionalisation we want $T_1 - T_2 = 1$, therefore

$$T_1 - T_2 = -\frac{\epsilon L}{6\kappa\beta} \left(r_1^2 - r_2^2 \right) = 1 \qquad (C.6)$$

Since $(r_1 - r_2) = -1$, then

$$\beta = \frac{\epsilon L}{6\kappa} \left(r_1 + r_2 \right) \qquad (C.7)$$

meaning that

$$T_{0*} = -\frac{1}{(r_1 + r_2)} r_*^2 \qquad (C.8)$$

C.2 Differential heating

If we assume instead that $\epsilon = 0$ then (C.2) becomes

$$T_0 = -\frac{A}{r} \tag{C.9}$$

We again use the temperature scale $\theta = \beta L$. Under the non-dimensionalisation (C.9) becomes

$$\theta T_{0*} = -\frac{A}{L}\frac{1}{r_*} \tag{C.10}$$

so,

$$T_{0*} = -\frac{A}{L\theta}\frac{1}{r_*} = -\frac{A}{\beta L^2}\frac{1}{r_*} \tag{C.11}$$

Again assuming $T_1 - T_2 = 1$, we obtain

$$T_1 - T_2 = -\frac{A}{\beta L^2}\left(\frac{1}{r_1} - \frac{1}{r_2}\right) = 1 \tag{C.12}$$

Since $(r_2 - r_1) = 1$, then

$$\beta = -\frac{A}{L^2 r_1 r_2} \tag{C.13}$$

meaning that

$$T_{0*} = (r_1 r_2)\frac{1}{r_*} \tag{C.14}$$

C.3 Intermediate heating sources

The above discussion covers the case of two different heating sources, each with different properties. It may also be desirable to have a heating source with input from both separate sources. To implement this we start from the non-dimensional unperturbed temperature distribution, introducing a parameter γ, which controls the ratio of heat

from different sources and must reflect the relative sizes of ϵ and A. This gives the following relation for T_{0*},

$$T_{0*} = \gamma \left(-\frac{1}{(r_1 + r_2)} r_*^2 \right) + (1 - \gamma) \left((r_1 r_2) \frac{1}{r_*} \right) \tag{C.15}$$

where $\gamma \in [0, 1]$, with $\gamma = 0$ corresponding to total differential heating and $\gamma = 1$ to total internal heating. For the expression given in (C.15) to be valid, then the following three conditions must hold

$$T_1 - T_2 = 1, \qquad \beta = \Delta T_0 / L, \qquad \theta = \beta L. \tag{C.16}$$

It can easily be shown that these three conditions are satisfied and that

$$\beta = \frac{\epsilon L}{6\kappa} (r_1 + r_2) - \frac{A}{L^2 r_1 r_2}, \tag{C.17}$$

where the following relation holds between ϵ and A,

$$\frac{\epsilon}{6\kappa A} = -\frac{\gamma}{1 - \gamma} \frac{1}{r_1 r_2 (r_1 + r_2)} \tag{C.18}$$

155